Optical Force on Atoms with Periodic Adiabatic Rapid Passage Sequences

A Dissertation Presented

by

Xiyue Miao

to

The Graduate School in Partial Fulfillment of the Requirements for the

Degree of

Doctor of Philosophy

in

Physics

Stony Brook University

August 2006

Stony Brook University

The Graduate School

Xiyue Miao

We, the dissertation committee for the above candidate for the Doctor of Philosophy degree, hereby recommend acceptance of this dissertation.

Distinguished Teaching Professor Harold J. Metcalf
Dissertation Director
Department of Physics and Astronomy

Professor Gene Sprouse
Chairman of Defense
Department of Physics and Astronomy

Professor Philip B. Allen
Department of Physics and Astronomy

Professor Charles Fortmann
Department of Applied Mathematics and Statistics

This dissertation is accepted by the Graduate School.

Graduate School

Abstract of the Dissertation

Optical Force on Atoms with Periodic Adiabatic Rapid Passage Sequences

by

Xiyue Miao

Doctor of Philosophy

in

Physics

Stony Brook University

2006

Adiabatic Rapid Passage (ARP) is a long-existing method to invert the population of a two-level nuclear spin system. Its extension to the optical domain necessitates a frequency chirped light pulse to interact with a two-level atom through dipole interaction. In this dissertation ARP processes for various pulse schemes and pulse parameters have been studied theoretically and experimentally. The non-adiabatic transition probability of ARP was quantified to characterize the efficiency of ARP for population transfer. Unanticipated regularities were found in the pulse parameter space. ARP sequences in periodic phase coherent counter-propagating light pulses can be used to produce large optical forces on atoms. The magnitude of the force is proportional to the

pulse repetition rate. So the force can be much larger than the usual radiative force if the pulse repetition rate is much higher than the spontaneous emission rate. The behavior of the atoms in such periodic ARP fields without spontaneous emission is well described by a periodic Hamiltonian. By investigating the evolution of the Bloch vector on the Bloch sphere, we related the average optical force on atoms to the non-adiabatic transition probability of a single pulse. Syncopation time has to be introduced in the pulsing scheme to produce a directional force in the presence of spontaneous emission. Experimentally, we observed the force on He* atoms by the deflection of the atomic beam with periodic chirped pulses from counter-propagating pulse trains. The chirped pulse train was realized by synchronized phase and amplitude modulation of the light from a cw diode laser. The Fourier spectrum of the modulated light was monitored to guarantee the quality of the chirped pulses. The measured ARP forces are about half of the theoretical predictions. Not only have we shown that such forces are huge and robust, but we have also been able to map the forces in the two dimensional pulse parameter space. The force distribution agrees qualitatively with the theoretical prediction.

To my parents, to Tianshi and Vivian

Table of Contents

List of Figures

List of Tables

Acknowledgements

At the point of nearly finishing this PhD work, I really have more appreciation of the hard work it demands. Without the help and support from so many people, I can not image how I can make through it by now.

First, I would like to express my profound gratitude to my advisor, Dr. Harold J. Metcalf, for his constant advice, support and guidance towards my Ph. D. thesis. I sincerely appreciate him for suggesting this exciting thesis topic. His scientific vigor and dedication makes him a great mentor. His great personality also makes him a good friend. Not only has he taught me about atomic physics, but also he has led me the way to do scientific research and to be a professional researcher. He is my advisor and a lifetime role model for me.

Next, I would like to acknowledge my husband, Dr. Tianshi Lu, who is also our collaborator in the theoretical work of this dissertation. Thank him for having done some beautiful theoretic analysis and numerical modelling for us. I have very much enjoyed the enlightening discussion with him throughout our collaboration, which has certainly enhanced my understanding of the physical picture. Furthermore, I am deeply indebted to him for his strong support in my life. I also would also like to acknowledge Dr. Tom Bergeman for his

careful review and thoughtful advice on our theoretical work. Dr. Bergeman has partially provided financial support to this work. I appreciate that deeply.

Team work is what makes things fun and fast. I really appreciate Esther Wertz and Dr. Martin Cohen, who joined me in the experiment during the past year. They are the ones who helped me to set the experiment up. I can not remember how many times Esther has done the fiber coupling for the experiment. I also thank her for helping me with the machine shop work. Marty was very helpful in the experiment, especially during the troubleshooting process. Benefitted from his broad knowledge and experience, we could really move things forward. I would also extend my thanks to Tak Chu Li and Htay Min Hlaing for helping me in taking data for the experiment. In addition, I would like to thank Hal, Marty and Esther for spending lots of time on correcting my thesis.

Friendship is what makes life full of sunshine. I am grateful to all the friends who have helped me and cheered me up when I was in the blues. Among whom, I especially thank Dr. Matthew Cashen. He is the most warmhearted person I have met in graduate school and he helped me to learn the rope in the lab. I truly thank Dr. Seung Hyun Lee for his help during the experiment. I thank Andy Vernaleken for his friendliness. Dr. Lee and Andy encouraged me a lot when I was in times of frustration. I thank Dr. Benjamin Dietzek, Dr. Olexiy Boyko, Matt Eardley for all the fun time we had together. It has also been a great pleasure getting to know, working with and learning from all the other past and current members of the group, Oleg Kritsun, Matt Partlow, Joerg Bochmann, Mattias Biedmann, Claire Shean, Jason Reeves and Michael

Keller. My experience with each one of them definitely broadened my horizon and enriched my life.

I would also like to express my gratitude to the staff in the physics Department for their support. Thank Peter Davis for supplying liquid nitrogen and helping us with the vacuum system. Many thanks to Chuck Pancake and Eugene Shafto for their help on electronics. Thank Walter Schmeling, Mark Jablonski and others in the machine shop. Thank Bob Segnini for doing a great job in maintaining the physics building. Thank Sal Natale for delivering all the packages for me. Thank Linda Dixon, Pat peliker, Diane Siegel, Mario Hofer, Elaine Larsen for their warm assistance all the time. I am especially thankful to Pam Burris, Sara Lutterbie for their enormous help in dealing with the bureaucracy to get me a position after graduation.

Finally, I owe my parents innumerable thanks. Throughout my academic career, the constant support of my parents has always motivated me to strive forward. The unconditional love of my parents has never been affected by the physical distance between us. I could have never have been able to accomplish this work without their encouragement and support and I could never repay them for what they did for me in my life. All I want to say is, I love you mum and dad. Last but not least, I want to thank my daughter Vivian for cheering me up from the exhaustion after days of hard work. My dissertation is dedicated to my parents and my family.

Chapter 1

Introduction

The field of laser cooling and trapping of neutral atoms, first proposed in middle 1970's [1, 2, 3], has progressed greatly the past 30 years. Laser cooling and trapping is of interest not only in fundamental research, but also for its practical applications [4]. It enables the study of the coherent and collective properties of atomic deBroglie waves, and research in optical lattices, Bose-Einstein condenstes and cold Fermions. Its applications include atomic clocks, atomic lithography, atomic lasers and quantum computing. Underlying the processes of laser cooling and trapping is the directional transfer of momentum from light fields to atoms. In this chapter I will present a brief introduction to laser cooling and trapping. Comprehensive reviews of these topics can be found in many places in the literature [4, 5, 6].

1.1 Two-level Atoms

The view of two-level atoms moving in a monochromatic laser field provides the fundamental picture of laser cooling and trapping of neutral atoms.

The evolution of the wave function of the atom in the monochromatic light field is governed by the time-dependent Schrödinger equation,

$$i\hbar\frac{\partial\psi}{\partial t} = H\psi. \tag{1.1}$$

In reality no atom is a two-level atom, but we can ignore the other atomic levels when the monochromatic field strongly couples only two of the internal electronic states of the atom. Typically these are the ground state and a low lying excited state, which can be labelled $|g\rangle$ and $|e\rangle$ respectively. The energy separation of the two states is $\hbar\omega_a$, where ω_a is the atomic resonance frequency. The monochromatic laser frequency is ω_l and the detuning of the laser frequency is defined as $\delta \equiv \omega_l - \omega_a$. The energy level diagram of such a two-level atom is shown in Figure 1.1.

1.1.1 Dressed Atom Picture

The monochromatic field can not only induce transitions between the two levels, but also shift the energy levels through the AC Stark effect. Due to the strong coupling of the two-level atom and the light field, one should consider the problem in the combined system of the atom and the laser field, where the total Hamiltonian of the system $H = H_{atom}+H_{rad}+H_{int}$ has three components. H_{atom} is the unperturbed atomic Hamiltonian, H_{rad} is the field Hamiltonian, and $H_{int} = -\vec{d}\cdot\vec{E}$ is the atomic dipole interaction with $\vec{d}$ being the atomic dipole moment and $\vec{E}$ being the electric field. For a monochromatic travelling wave light field, $\vec{E} = E_0\hat{\varepsilon}\cos(kz - \omega_l t)$ where $\hat{\varepsilon}$ denotes the polarization of

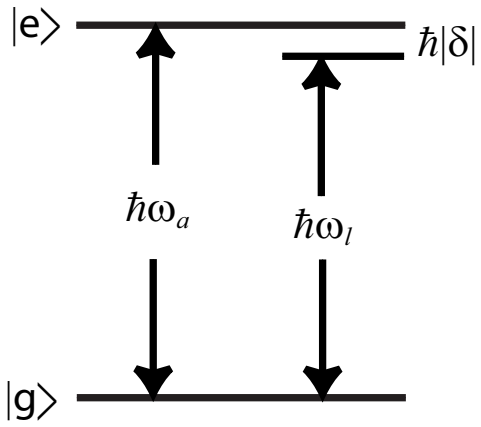

Figure 1.1: Energy levels of the two-level atom subject to a monochromatic laser field. The ground $|g\rangle$ and excited $|e\rangle$ states are separated by $\hbar\omega_a$. The photon energy of laser light is $\hbar\omega_l$. The light frequency of the laser field can be detuned from the resonance by $\delta \equiv \omega_\ell - \omega_a$.

the light field. The energy levels of the two-level atom consist of $|g\rangle$ and $|e\rangle$ called the bare atomic states. The field has an infinite number of energy levels given by $E_n = (n + \frac{1}{2})\hbar\omega_l$. Neglecting the dipole interaction term, the energy levels of the combined system $|g, n\rangle$ and $|e, n\rangle$ form an infinite set of two-dimensional manifold spaced by a photon energy $\hbar\omega_l$, where each manifold consists of $|g, n+1\rangle$ and $|e, n\rangle$ with separation $\hbar\delta$ in between. The dipole interaction couples each pair within a manifold and pushes them apart. Since we only care about the atomic evolution, the field energy can be discarded, and a semiclassical description confined to the two dimensional Hilbert basis is adequate.

Assume the atom is localized, *i.e.* $\lambda_{dB} < \lambda$ where λ_{dB} represents the de Broglie wave wavelength of the atom and λ is the light wavelength. The

coupling term can be written as $H_{eg}^{int} = -\hbar\Omega\cos(kz - \omega_l t)$, where Ω is the Rabi frequency that characterizes the on-resonance, electric dipole interaction between the light field and atom and is defined by $\Omega \equiv \frac{E_0}{\hbar}\langle g|\vec{d}\cdot\hat{\varepsilon}|e\rangle$ By transforming to a frame rotating with ω_l and neglecting the counter-rotating component [7], the Hamiltonian of the system can be simplified as shown below:

$$H = \frac{\hbar}{2}\begin{pmatrix} \delta & \Omega \\ \Omega & -\delta \end{pmatrix}. \tag{1.2}$$

Note that the ground and excited states in the rotating frame differ from the bare atomic ground and excited states in the laboratory frame by an opposite time dependent phase factor $e^{\pm i\omega_l t/2}$, *i.e.* a rotating frame transformation. We will still refer then as $|g\rangle$ and $|e\rangle$ for convenience. If the transition between $|g\rangle$ and $|e\rangle$ involves circularly polarized light as in the case of our experiment, no rotating wave approximation is needed and the Hamiltonian in dressedH is thus exact [7].

The eigenstates of this Hamiltonian in the basis of $|g\rangle$ and $|e\rangle$ in the rotating frame are given by

$$\begin{aligned} \psi_+ &= (|g\rangle\ |e\rangle)\begin{pmatrix} \cos(\theta/2) \\ \sin(\theta/2) \end{pmatrix} \\ \psi_- &= (|g\rangle\ |e\rangle)\begin{pmatrix} -\sin(\theta/2) \\ \cos(\theta/2) \end{pmatrix}, \end{aligned} \tag{1.3}$$

where θ is the mixing angle, $\tan\theta = \Omega/\delta$. The corresponding eigenenergies are

$$E_{\pm} = \pm\hbar\Omega'/2 \tag{1.4}$$

with $\Omega' = \sqrt{\delta^2 + \Omega^2}$ called the generalized Rabi frequency. These eigenstates are the so-called dressed atom states [8]. $|g\rangle$ and $|e\rangle$ here correspond to the dressed atom states in the diabatic limit, *e.g.* $\Omega \longrightarrow 0$. The basis spanned by $|g\rangle$ and $|e\rangle$ is thus called the diabatic basis. When the light field has non-vanishing intensity, the dressed atom eigenenergies are shifted from the energies of the diabatic states, and these shifts are called the light shifts. The light shifts in a standing wave can be considered as spatially varying periodic potentials which can be used to trap atoms.

1.1.2 Bloch Sphere

A three dimensional projection of the two dimensional Schrödinger equation in the rotating frame gives a very instructive view of the atomic response to laser fields [7, 9]. The state of the two-level atom can be represented by a vector $\vec{R}$ whose three components are defined below:

$$\begin{aligned} r_1 &= c_g c_e^* + c_g^* c_e \\ r_2 &= i(c_g c_e^* - c_g^* c_e) \\ r_3 &= |c_e|^2 - |c_g|^2, \end{aligned} \tag{1.5}$$

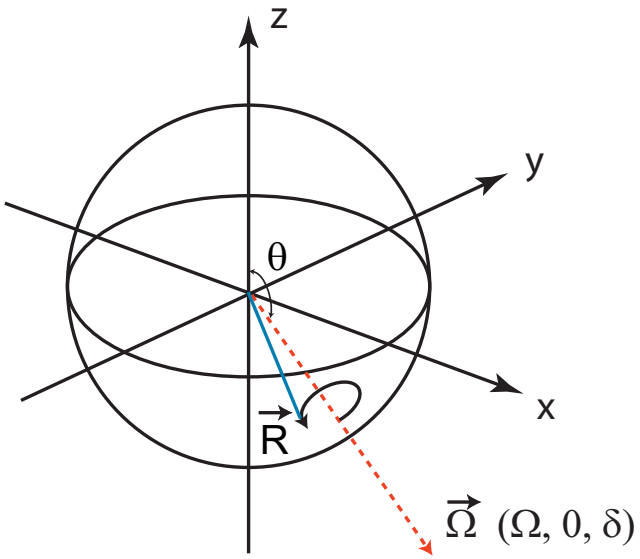

Figure 1.2: The precession of the Bloch vector around the torque vector on the Bloch sphere. The solid line represents the Bloch vector $\vec{R}$ and the dashed line represents the torque vector $\vec{\Omega}$.

where c_g, c_e are the coefficients of the ground state and excited state components of the atomic wave function in the rotating frame, *i.e.* $\psi = c_e|e\rangle + c_g|g\rangle$. $\vec{R}$ is called the Bloch vector. It can be shown that $|\vec{R}| = |c_e|^2 + |c_g|^2 = 1$. The Bloch vector is thus confined on the surface of a unit sphere, namely the Bloch sphere, by conservation of the atomic probability. The south pole of the Bloch sphere corresponds to the ground state of the atom, the north pole corresponds to the excited state and other points on the sphere represent various superposition states. From the Schrödinger equation, the equation of motion of the Bloch vector can be derived as:

$$\frac{\mathrm{d}\vec{R}}{\mathrm{d}t} = \vec{\Omega} \times \vec{R}, \tag{1.6}$$

where $\vec{\Omega} = (\Re(\Omega), \Im(\Omega), \delta)$ is called the torque vector and it is determined by the Rabi frequency and the detuning of the applied laser field. In general Ω is complex. However, a frame transformation can be introduced to make Ω real so that $\vec{\Omega} = (\Omega, 0, \delta)$. The Bloch vector precesses around the torque vector on the unit sphere like a pseudospin as shown in Figure 1.2. The Bloch sphere view provides a versatile tool for the analysis of quantum logic and entanglement.

1.2 Radiative Force

The radiation pressure, or the radiative force is the simplest force on a two-level atom interacting with a monochromatic laser field. When a two-level atom is illuminated by a monochromatic laser field whose frequency is tuned

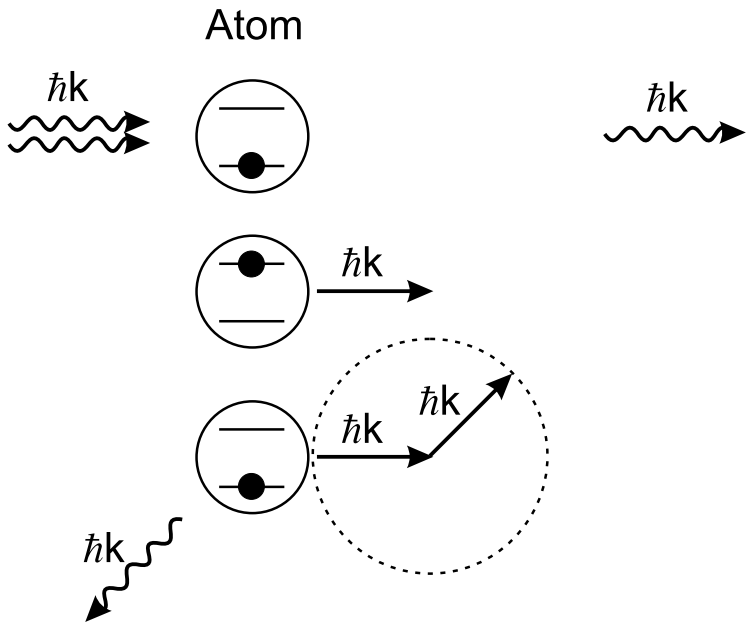

Figure 1.3: The cycle that produces the radiative force. The absorption of the incident photon in the laser field excites the two-level atom and also transfers momentum $\hbar\vec{k}$ to the atom. The atom can decay by spontaneous emission, where the associated momentum transfer is spatially symmetric and therefore averages away after many cycles. So a net momentum transfer in the laser propagation direction is delivered to the atom.

near atomic resonance, it will be excited by absorption of a photon, which is accompanied by a momentum transfer of $\hbar\vec{k}$, where $\vec{k}$ is the wavevector of the laser field with $|\vec{k}| = k = \frac{\omega_l}{c}$. The momentum transfer via absorption of laser photons is always along the direction of the laser beam propagation. Now, if the atom decays back to the ground state via spontaneous emission, the emitted photon will carry away momentum of $\hbar\vec{k}$. However, the spontaneous emission is in a random direction, the momentum loss via spontaneous emissions is spatially symmetric and averages to zero over many cycles. Therefore, stimulated absorption followed by spontaneous emission will, on average, result in a pushing of the atoms in the direction of the laser beam propagation. In other words, the atoms will experience a pressure in the laser field, which is called the radiation pressure. The process can be visualized in Figure 1.3. Notice that a weak field is assumed here, so that spontaneous emission is predominant over stimulated emission. The net force on the atom is proportional to the rate of this process, *i.e.* the scattering rate γ_p,

$$\vec{F}_{rad} = \hbar\vec{k}\gamma_p. \tag{1.7}$$

For an atom at rest, γ_p is given below:

$$\gamma_p = \frac{s\gamma/2}{1 + s + (2(\delta))/\gamma)^2}. \tag{1.8}$$

Here s is the on-resonance saturation parameter, which is the ratio of the intensity of the laser field to the saturation intensity,

$$s \equiv 2\frac{|\Omega|^2}{\gamma^2} = \frac{I}{I_{sat}} \tag{1.9}$$

with $I_{sat} \equiv \frac{\pi hc}{3\lambda^3\tau}$, τ is the lifetime of the two-level atom and $\gamma \equiv \frac{1}{\tau}$ is the spontaneous emission rate of the two-level atom. The radiation force saturates at $\frac{\hbar k\gamma}{2}$ since a two-level atom driven by the on-resonance light field can stay at most half of the time in the excited state and thus can decay by spontaneous emission, this is also manifested in Eq. (1.8), when $\delta = 0$ and $s \gg 1$

1.3 Doppler Cooling

For an atom with velocity $\vec{v}$ in the laboratory frame, the Doppler shift, the frequency shift of the light field seen by the moving atom is $\omega_D = -\vec{k} \cdot \vec{v}$. An effective detuning $\delta_{eff} = \delta + \omega_D$ should be substituted in Eq. (1.8). Therefore the radiative force on the moving atom is given by:

$$F_{rad} = \hbar k \frac{s\gamma/2}{1 + s + (2(\delta - \vec{k} \cdot \vec{v})/\gamma)^2.} \tag{1.10}$$

The force on a atom ensemble has a Voigt profile peaked at $\delta_{eff} = 0$ [10]. For on-resonance light, the force is centered for zero-velocity atoms. For an off-resonance light, the force center is shifted to the group of atoms moving with velocity $\vec{v} = \delta\vec{k}/k^2$.

The radiative force is used in the Zeeman slowing of atomic beams, in

which a red detuned laser beam is directed oppositely to an atomic beam. However, the Doppler effect limits the velocity range of the atoms with which the laser is in resonance. To keep the light field always in resonance with the atoms along their path, a spatially varying magnetic field is applied along the beam path, which shifts the energy levels of the atoms to compensate for the changing Doppler shift while the atoms are slowed down [11].

The velocity dependence of the radiative force can also be used to cool the atoms in a standing wave configuration. Consider a standing wave of a red detuned ($\delta < 0$) laser field. Due to the Doppler shift, the radiative push by the right moving laser beam has its peak shifted to the atoms moving to the left, while the radiative push by the left moving laser beam has its peak shifted to the atoms moving to the right. In the low intensity limit, the forces from the two counter-propagating beams can simply be added together. The explicit expression of the force is [4]

$$\begin{aligned} \vec{F} &= \hbar\vec{k}\frac{\gamma s/2}{1+s+(2(\delta-\vec{k}\cdot\vec{v}))/\gamma)^2} - \hbar\vec{k}\frac{\gamma s/2}{1+s+(2(\delta+\vec{k}\cdot\vec{v}))/\gamma)^2} \\ &\approx \frac{8\hbar\vec{k}\delta s\vec{v}\cdot\vec{k}}{\gamma(1+s+(2\delta/\gamma)^2)^2} \\ &\equiv -\beta\frac{\vec{k}(\vec{k}\cdot\vec{v})}{k^2} \end{aligned} \tag{1.11}$$

The approximation is taken in the limit of small velocities ($kv < \gamma, \delta$), so that terms of order $(kv/\gamma)^4$ and higher can be neglected. It is clear that the force is a damping (cooling) force only if $\delta < 0$, since a positive β results. The force was given the name optical molasses due to its viscous nature, and the cooling

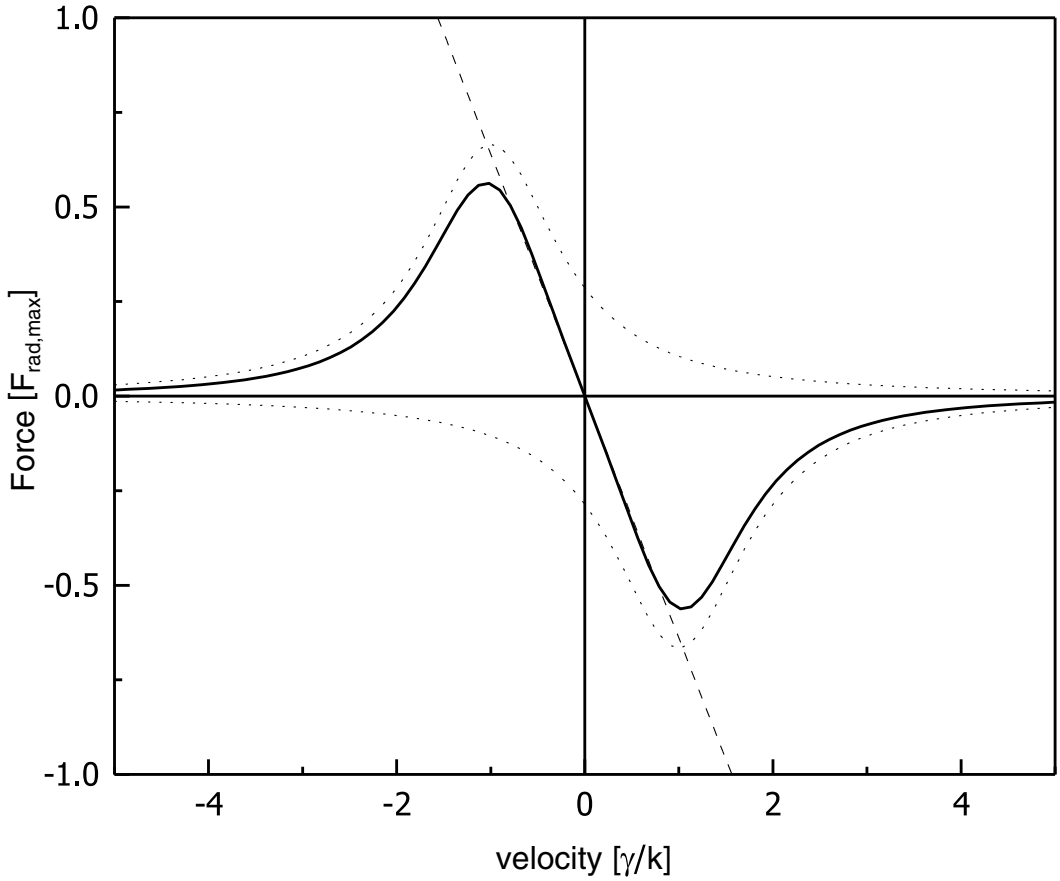

Figure 1.4: Optical molasses with $s = 2$ and $\delta = -\gamma$. The two dotted lines show the force due to each individual beam, and the solid line is the combined force. The linear dashed line has slope $-\beta$.

scheme is called Doppler cooling. The velocity capture range of the force is $v_c = \frac{\gamma}{k}$, which corresponds to a Doppler shift pushing the atom out of its natural absorption linewidth. The force with $s = 2$ and $\delta = -\gamma$ is illustrated in Figure 1.4.

Although the mean final velocity of the Doppler cooling is zero, it has a nonzero temperature limit due to a competitive heating process resulting from the discrete momentum transfer steps. The randomness in the spontaneous emissions produces a momentum fluctuation with step size $\hbar k$ and step frequency $2\gamma_p$ (2 because of two beams) about the mean momentum, . The resulting coefficient for momentum diffusion is $D_0 = 2\gamma_p(\hbar k)^2$. The steady state temperature is given by Brownian motion theory as $k_B T = D_0/\beta$. The minimum reachable temperature via Doppler cooling, *i.e.* the Doppler temperature, is then $T_D = \hbar\gamma/2k_B$. For the typical atoms used in laser cooling experiments, namely the alkalis and metastable noble gases, these temperatures range from hundreds of μK to tens of μK.

1.4 Sisyphus Cooling

Experimental observation of temperatures below the Doppler limit in sodium atoms in 1988 came as a big surprise [12]. The simplified two-level atom picture was found inapplicable in this case. New theories with the multiplicity of the atomic sublevels incorporated were soon developed [13, 14] and had great success in clarifying the puzzle.

The optical pumping among the multiple levels in spatially varying light shift potentials provides the mechanism to cool the atom below the Doppler

temperature. Since the kinetic energies of the atoms are transferred to the potential energy in climbing the light field potential and then radiated away via spontaneous emissions in optical pumping; the whole process can thus be repeated over and over. The new cooling mechanism was named Sisyphus cooling due to the similarity of the atomic behavior to that of King Sisyphus in Greek mythology. It actually categorizes a class of cooling schemes which include polarization gradient cooling [14], magnetic induced laser cooling [15], high intensity blue molasses cooling [16] etc. Sisyphus cooling in general has a much larger damping coefficient than that of Doppler cooling, while the diffusion coefficient is about the same. Therefore, it has a lower temperature limit. However, its velocity capture range is usually smaller.

The extension of the two-level atom in a monochromatic field to the multilevel picture provides an unexpected richness to the atomic motion in optical fields and leads to a broad subbranch in laser cooling. An excellent review article of this subject can be found in [17]. More details are also given in [4] and the references therein.

1.5 Dipole Force

The dipole force plays an important role in the Sisyphus cooling schemes described in Section 1.4. The dipole force can be derived from the spatial light shift gradient of the standing wave light field made up by two counter-propagating monochromatic light beams. The origin of the force is the coherent momentum exchange between the atom and the light fields by absorption of a photon from one light beam followed by stimulated emission of a pho-

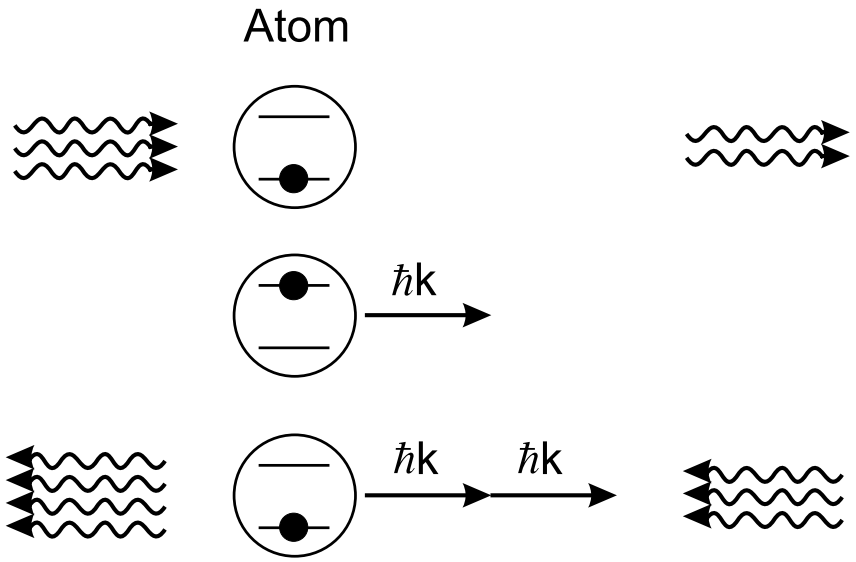

Figure 1.5: The cycle that produces the dipole force. The atom is subject to a standing wave light field made up by two counter-propagating monochromatic light beams. A stimulated absorption of a photon from one light beam followed by a stimulated emission of a photon from another beam transfers a net $2\hbar k$ momentum to the atom at each cycle.

ton to the opposite laser beam, with a net $2\hbar k$ momentum transfer resulting from each cycle. The process is illustrated in Figure 1.5. Since the stimulated emission and absorption rate can increase with the light field intensity with no limit, the force is thus not limited by the spontaneous emission rate. However, this process can take place in both directions due to the symmetry of the light field. The dipole force is not only conservative but also vanishes when averaged over a wavelength. This force can be used to trap atoms but not cool or slow atoms. In the standing wave configuration, the symmetry needs to be broken down to define a preferred direction for momentum transfer.

In the well-studied case of high intensity blue molasses, such symmetry breaking is introduced by spontaneous emission. The spontaneous emission rate is spatially dependent since the exited state components in the dressed atom eigenstates are changing spatially with the light field intensity. This spatial dependent spontaneous emission rate not only results in a directional force but also provides the irreversibility that gives rise to a velocity-dependent force [4]. The force can thus be used for cooling the atoms.

The cooling forces used in polarization gradient cooling and magnetic induced laser cooling are similar, except that more that one of the sublevels are involved. The symmetry breaking is optical pumping between different light shifted potentials induced by the polarization gradient or the magnetic field. The optical pumping is in turn enabled by spontaneous emission [17].

Some rectified dipole force schemes had been proposed to make better use of the dipole force for manipulating atoms [18, 19]. Here the interaction of two-level atoms with more non-monochromatic light fields are involved. For

example, by using a second, far detuned standing wave to provide a modulation of the atomic transition frequency on the wavelength scale, the dipole force produced by the near resonant standing wave light field is then rectified to have a nonzero spatial average. The rectified dipole force has been investigated by several groups [20, 21, 22]. The resulting force has a magnitude several times bigger than that of the radiative force. However, this dipole force rectification mechanism has very stringent frequency requirements to produce the effective atomic transition frequency modification and thus can only tolerate small Doppler shifts. Therefore the velocity range of the force is very limited. Note that this rectified force is still conservative as a result of the absence of spatial dependent spontaneous emission and is not suitable for cooling.

1.6 Bichromatic Force

The bichromatic force can be considered as a special case of the rectified dipole force. However, the description given in the previous section of the rectified dipole force does not apply due to the very large detunings and intensities of the two light frequencies. The bichromatic light field has two frequency components with equal intensities oppositely detuned from the atomic resonance by $\pm\delta(\delta > 0)$. Each component plays an equally important role in the production of the force. The bichromatic force has a magnitude and a velocity capture range both scaling with δ. This makes it very efficient in slowing and cooling of atoms. The force has been demonstrate in Na [19], Cs [23], Rb [24, 25], and He [26, 27, 28]. Two models used to give a physical interpretation to the bichromatic force are discussed below.

1.6.1 π-pulse model

The most intuitive description of the bichromatic force is given in a π-pulse model [29, 21, 23]. The model starts by beating the two frequency components of the light field together. The electric field can be written as:

$$\begin{aligned} E &= E_0 \cos[(k+\Delta k)z - (\omega_a + \delta)t] + E_0 \cos[(k-\Delta k)z - (\omega_a - \delta)t] \\ &= 2E_0 \cos(\delta t - \Delta k z)\cos(kz - \omega_a t) \end{aligned} \tag{1.12}$$

where $k = \omega_a/c = 2\pi/\lambda$, and $\Delta k = \delta/c$. The resulting field is an amplitude modulated travelling wave with carrier frequency at ω_a and the modulation frequency δ. Each beat envelope can be seen by the atom as a pulse. Using a π-pulse condition [7] in the Bloch sphere picture, if the time integral of the Rabi frequency of the on-resonance pulse is π, an atom starting in the ground state rotates along the meridian (perpendicular to the on-resonance torque vector) on the Bloch sphere by π radians and ends up in the excited state. An atomic population inversion is thus induced and we say a photon of energy $\hbar\omega_a$ is absorbed and a momentum kick of $\hbar k$ is associated with the absorption. The π-pulse condition for each bichromatic beat envelope is:

$$\int_{-\pi/2\delta}^{\pi/2\delta} 2\Omega_0 \cos(\delta t) dt = \pi \tag{1.13}$$

which demands $\Omega_0 = \frac{\pi}{4}\delta$, where $\Omega_0 = dE_0$ is the amplitude of the Rabi frequency of each frequency component. With this condition satisfied, the bichromatic beat signal becomes a series of π-pulses . A retro-reflection of the

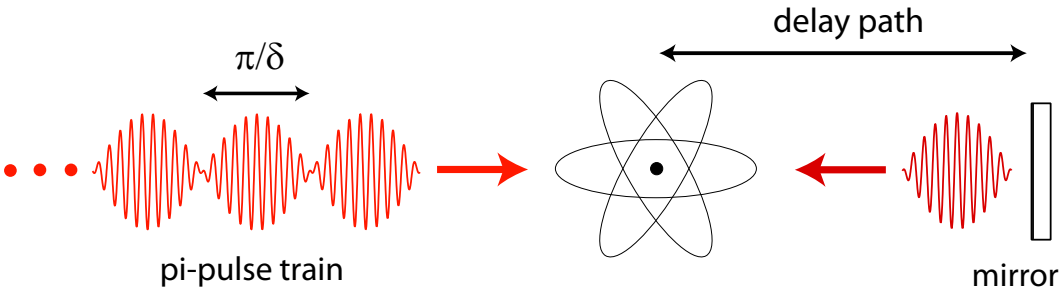

Figure 1.6: Coherent momentum transfer using bichromatic pulse trains. The position of the mirror serves to set a delay time between the arrival of the two counter-propagating pulse trains.

beat pulses creates a counter-propagating π-pulse train. The bichromatic force comes from the coherent control of momentum exchange between the atoms and π-pulse trains.

As in the dipole force, the bichromatic force comes from absorption followed by stimulated emission of the light field. In figure 1.6, if the atom is excited by the π-pulse from the left and deexcited by the π-pulse from the right, a total momentum $2\hbar k$ to the right is transferred to the atom. Without spontaneous emission, the repetition rate of the process is δ/π, the force is $F = \frac{\Delta p}{\Delta t} = \frac{2\hbar k}{\pi/\delta} = \frac{2\hbar k\delta}{\pi}$, so it can be much larger than the radiative force $\hbar k\gamma/2$ if $\delta \gg \gamma$.

When spontaneous emission occurs, the atom is returned to the ground state so that absorption rather than stimulated emission occurs with the next π-pulse, and thus the direction of the force is switched. When the field is symmetric, the process can happen in either direction, there is no preferred direction of the momentum transfer. A directional momentum transfer can be

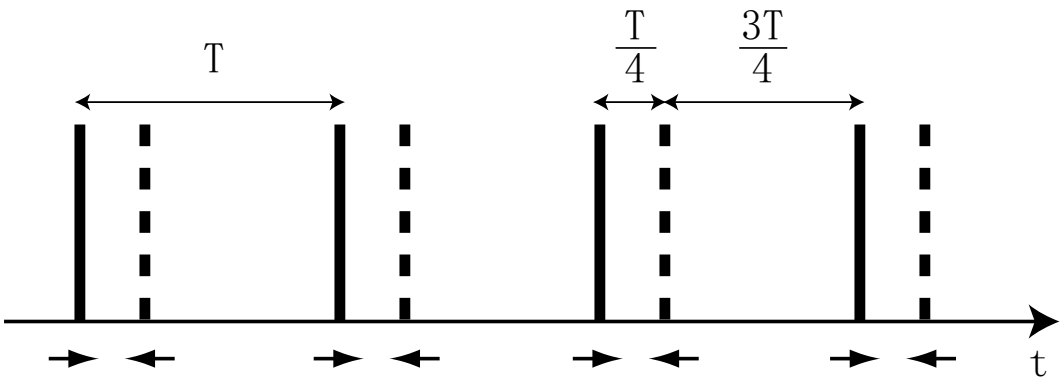

Figure 1.7: The timing of Bichromatic π-pulses via the delay path to produce a unidirectional force. The centers of the right propagating π-pulses are marked with solid lines and the centers of the left propagating π-pulses are marked with the dashed lines. The pulse from right and left are paired with separation $\frac{T}{4}$ within each pair and separation of $\frac{3T}{4}$ between neighboring pairs. The direction of the force comes from the longer time for spontaneous emission to occur and prepare the atom in the ground state before the arrival of the pulse pairs.

created via spontaneous emission in an asymmetric field. We can choose an uneven arrival time spacing among pulses in the two directions by choosing the time delay in Figure 1.6 to be $\frac{T}{4}$, where $T = \pi/\delta$ is the pulse period. Now each π-pulse from the left and from the right are paired with a $\frac{T}{4}$ time spacing within a pair and $\frac{3T}{4}$ between neighboring pairs. The probability of spontaneous emission occurring in the time interval between the pulse pairs is $\frac{3}{4}$ and the probability of it occurring within the pulse pairs is $\frac{1}{4}$. The atom is more likely to be prepared in the ground state by spontaneous emission before the arrival of a pulse pair and a unidirectional force is then produced. The $\frac{T}{4}$ delay time corresponds to a $\phi = \pi/2$ phase delay of the retroreflected beat pulses.

The magnitude of the force can be calculated as below:

$$F_B = (\frac{3}{4} - \frac{1}{4}) \cdot 2\hbar k \cdot \frac{\delta}{\pi} = \frac{\hbar k \delta}{\pi} \tag{1.14}$$

The force can be arbitrarily large by increasing δ. Note that, in the above picture, if the delay time is chosen to be $\frac{3T}{4}$ the direction of the force reverses.

Though the simple π-pulse model provides insight into the bichromatic force which leads to a good estimation of the magnitude of the force, the temporal overlap between pulses is left out. The velocity dependence of the force is also excluded in the picture. A more careful analysis in a doubly-dressed atom picture (DDA) presents a better model of the bichromatic force [30, 31, 32] and will be discussed next.

1.7 Doubly Dressed Atom Picture

In the DDA picture, the atom is dressed simultaneously by the blue-detuned standing wave light field ($\omega_a + \delta$) and the red-detuned one ($\omega_a - \delta$). The total electric field is written by grouping the counter-propagating light components with the same frequency together.

$$E = 2E_0 \cos(kz + \chi/2) \cos[(\omega_a + \delta)t] + 2E_0 \cos(kz - \chi/2) \cos[(\omega_a - \delta)t] \tag{1.15}$$

where the two standing waves are spatially out of phase by $\chi = 2\Delta kz = 2\delta z/c$.

As in the dressed atom picture for two-level atom at rest in a monochromatic field, the DDA approach starts with enumerating the diabatic states

which are the product states of the bare atom and the light field. These states can be label as $|g, b, r\rangle$ and $|e, b, r\rangle$, where $|g\rangle$ and $|e\rangle$ are the ground and excited states of the atom, b represents the quantum number in the blue-detuned light field, and r represents the quantum number in the red-detuned light field. Each pair of diabatic states in the (singly) dressed atom picture are now extended to an infinite set of states equally spaced by $\hbar\delta$.

The Hamiltonian of the atom-photon system can be written in a set of the diabatic eigenstates bases as an infinite tridiagonal matrix [30, 32]. The truncated 7×7 Hamiltonian matrix over $\hbar$ is listed below:

$$\begin{bmatrix} 3\delta & \Omega_2 & 0 & 0 & 0 & 0 & 0 \\ \Omega_2 & 2\delta & \Omega_1 & 0 & 0 & 0 & 0 \\ 0 & \Omega_1 & \delta & \Omega_2 & 0 & 0 & 0 \\ 0 & 0 & \Omega_2 & 0 & \Omega_1 & 0 & 0 \\ 0 & 0 & 0 & \Omega_1 & -\delta & \Omega_2 & 0 \\ 0 & 0 & 0 & 0 & \Omega_2 & -2\delta & \Omega_1 \\ 0 & 0 & 0 & 0 & 0 & \Omega_1 & -3\delta \end{bmatrix} \tag{1.16}$$

where the off diagonal elements are the spatially dependent Rabi frequency of the standing wave of each frequency component divided by 2.

$$\Omega_{1,2} = \Omega_0 \cos(kz \pm \chi/2) \tag{1.17}$$

The doubly dressed Hamiltonian in the diabatic basis is derived by a Floquet approach in [32]. The approximate value for the position dependent eigenener-

gies of the DDA eigenstates are calculated by diagonalizing the above Hamiltonian. The approximated dressed state energy levels for $\delta = 10\gamma$ and $\chi = \pi/4$ calculated with a 11×11 Hamiltonian are plotted in Figure 1.8.

At the nodes of one of the standing waves the Rabi frequency of the frequency component is vanishing, *e.g.* $\Omega_2 = 0$, the matrix Hamiltonian (Eq. (1.16)) becomes a series of 2×2 matrices which can be solved analytically. The uncoupled states can then cross at some critical value of Ω_1, the Rabi frequency of the second standing wave. Such crossing makes the climbing on the Landau-Zener ladder possible for the atoms and thus produces the large bichromatic force. The level crossing conditionss are given in [32] as

$$\begin{aligned} \Omega_0 \cos(cos(kz - \chi/2) &= 0 \\ \Omega_0 \cos(cos(kz + \chi/2) &= \delta\sqrt{n^2 - \frac{1}{2}} \quad (n = 1, 2, ...). \end{aligned} \tag{1.18}$$

The dependence of χ versus Ω_0 can be obtained by solving Eq. (1.18). For the case of $\chi = \pi/4$, Eq. (1.13) demands $\Omega_0 = \sqrt{\frac{3}{2}}\delta$. This corresponds to $\phi = \pi/2$ in the π-pulse model. However, the π-pulse condition requires $\Omega_0 = \frac{\pi}{4}\delta$. The optimal force condition obtained from Eq. (1.18) agrees well with the force calculated by numerically solving the optical Bloch equation, Eq. (1.6) with spontaneous emission included, and then applying the Ehrenfest theorem [30].

The force magnitude can be derived by the slope of the DDA eigenenergy levels in the crossing condition. Spontaneous emission is included by weighting the excited state component in the DDA eigenstates. The same result as the π-pulse model is achieved which agrees with both the experiment and the

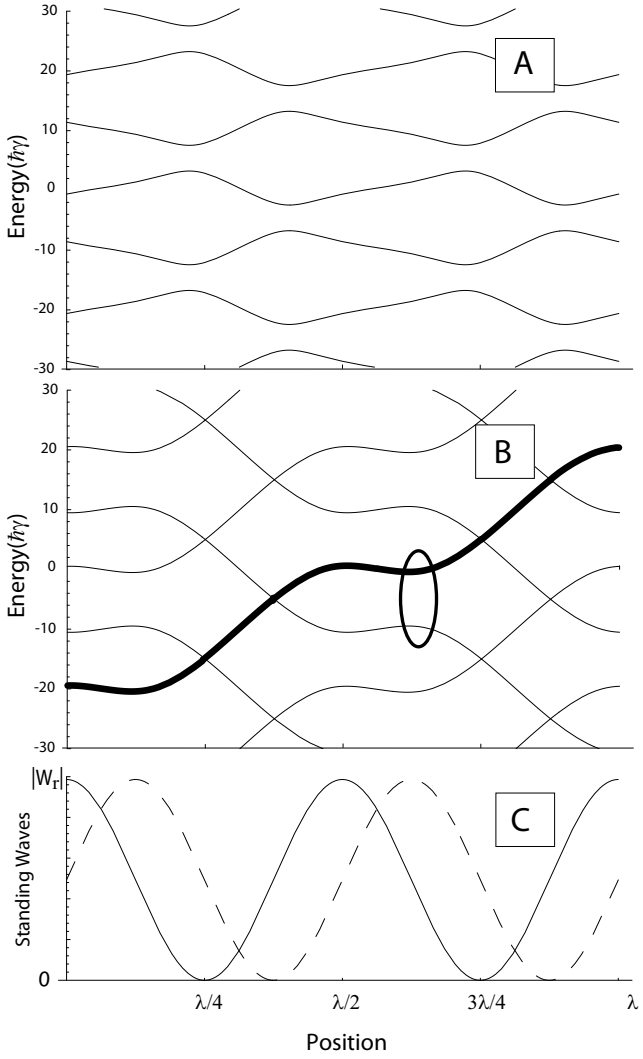

Figure 1.8: Spatial dependence of the approximate dressed state energy levels for $\delta = 10\gamma$ and $\chi = \pi/4$.In part (A) $\Omega_0/\delta = \pi/4$, the π-pulse condition. In part (B), $\Omega_0/\delta = \sqrt{6}/2$. In part (C) the standing wave intensities are plotted. Note that the levels are equally spaced where the intensities of the two standing waves are equal. The energy level crossing occurs at the node of one standing wave when the Rabi frequency of the other standing wave satisfies certain conditions. In this case it is $\Omega_0/\delta = \sqrt{6}/2$. The heavy line in (B) showing a possible path of an atom moving diabatically through the real crossings which give rise to the large bichromatic force.

optical Bloch equation calculation. The velocity capture range of the force stems from the requirement of adiabatic following of the DDA eigenstates at the avoided crossings as marked by the ellipse in Figure 1.8B. A velocity range of $\pm\delta/4k$ is obtained in [32] from this point of view. However, this is only half of that given by the numerical force calculation. The difference is believed to arise from the fact that the Floquet Hamiltonian approach does not include the Doppler shift of the optical frequencies due to atomic motion. A second Floquet approach, in a reference frame moving at velocity $v_{ref} = \delta/2k$, is in development by the authors of [32] and is expected to complete the picture.

Chapter 2

Theory of Adiabatic Rapid Passage

As suggested by the title of this dissertation, the focus of this work is the study of the optical force on two-level atoms associated with periodic adiabatic rapid passage (ARP) sequences. ARP is a long-studied method of inverting the population of a two-level system that is well known since the early days of magnetic resonance [33]. In the optical regime, ARP requires a light pulse whose frequency is swept through the resonance of the two level system [34, 35]. Its exploitation for producing large optical forces requires repeated sweeps with oppositely directed light beams that coherently exchange momentum between the beams, imparting the difference $2\hbar k$ to the atoms in each cycle [36]. When the repetition rate of these cycles is $1/T \gg \gamma$ the ARP force is $F_{ARP} = 2\hbar k/T$ which can be much large than the radiative force, $F_{rad} = \hbar k\gamma/2$ [37].

2.1 Adiabatic Rapid Passage

An ARP process of a two-level atom can be induced by a chirped pulse. The carrier frequency of the light field is chirped as the amplitude is pulsed.

The ARP process can be envisioned in a dressed-atom view of the energies of the two-level system [38, 37]. In the concomitant rotating frame [7] of the light field, *i.e.* the adiabatic frame - the frame spanned by instantaneous dressed atom states (see Section 1.1.1), the Hamiltonian of the system can be written as:

$$H(t) = \frac{\hbar}{2} \begin{pmatrix} \delta(t) & \Omega(t) \\ \Omega(t) & -\delta(t) \end{pmatrix}, \tag{2.1}$$

where $\delta(t)$ is the instantaneous detuning of the light frequency, and $\Omega(t)$ is the instantaneous Rabi frequency as defined in Chapter 1. The eigenenergies of the coupled levels are given by Eq. (1.4) as $E(t)_{\pm} = \pm(\hbar/2)\sqrt{\delta(t)^2 + \Omega(t)^2}$.

An important aspect of the dressed atom picture for the present concern is the energy ordering of the eigenstates. In the low-intensity domain (characterized by $\Omega < \delta$) the upper eigenstate approaches the ground state $|g\rangle$ in the diabatic frame and the lower one approaches the excited state $|e\rangle$ in the diabatic frame for the case of $\delta > 0$ but the reverse is true for $\delta < 0$. A plot of the energy of the dressed atom eigenstates is shown in Fig. 2.1 showing these limits near the $\Omega = 0$ plane, and also that these ground and excited states $|g\rangle$ and $|e\rangle$ are otherwise mixed on two eigenenergy sheets away from the low intensity limit (see Ref. [38]).

The process of adiabatic rapid passage (ARP) in this view involves a synchronized sweep of both the amplitude and frequency of the light so that the dressed atom eigenstate of the system follows a trajectory similar to that of the heavy line in Figure 2.1 (δ_0 is the amplitude of the frequency sweep). The trajectory on the lower energy sheet is not shown but behaves similarly.

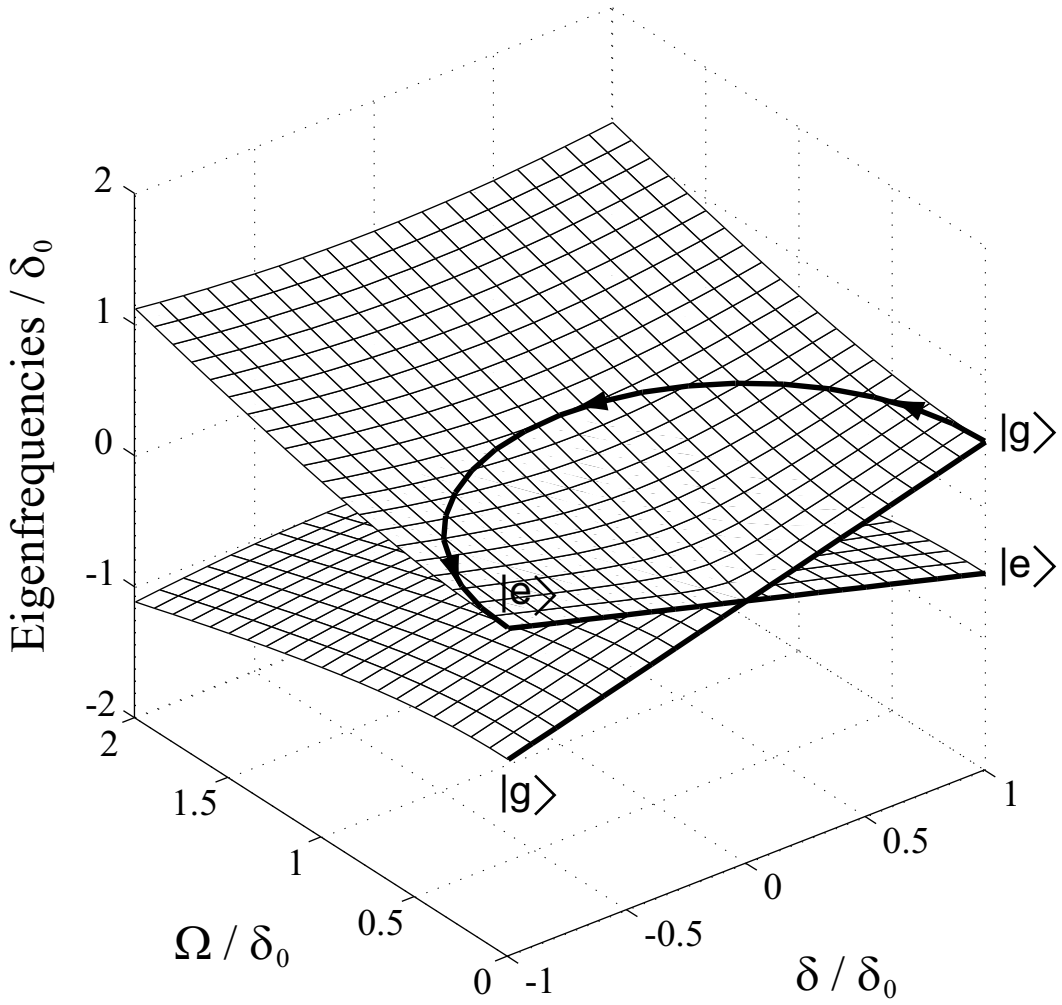

Figure 2.1: Energy of the dressed states comprise two separated sheets except at the conical intersection at the origin. The upper (lower) state is ground at $\Omega = 0$ for $\delta > 0$ ($\delta < 0$). The indicated path is a possible trajectory for ARP.

As long as the sweep is slow enough, the state of the two-level system follows one of the dressed atom eigenstates adiabatically, and the population will be inverted. For optical transitions there is always decay out of $|e\rangle$ by spontaneous emission at a rate γ, and the "R" in ARP requires that the sweep rate ω_m satisfies $\omega_m \gg \gamma$.

An alternative view is the rotation of the Bloch vector on the Bloch sphere under the influence of the modulated light field. The vertical axis (z) of the sphere is the population difference term and the horizontal axes are related to the relative phase of the atomic superposition [7]. The equation of motion for the Bloch vector, which is given in Eq. (1.6), is repeated here,

$$\frac{\mathrm{d}\vec{R}}{\mathrm{d}t} = \vec{\Omega}(t) \times \vec{R}, \tag{2.2}$$

where $\vec{\Omega}(t)$ is the "torque" vector having components $[\Omega(t), 0, \delta(t)]$. Eq. (2.2) is called the Bloch equation.

The process of adiabatic rapid passage (ARP) in this view involves a synchronized sweep of both the amplitude and frequency of the light so that the torque vector sweeps across the Bloch sphere along a meridian from one pole to the other. If the initial state lies in an eigenstate, $\vec{R}$ will start from a pole and precess around the torque vector to the other pole as illustrated in Figure 2.2(a). As long as the sweep is slow enough, the Bloch vector is always close to the torque vector, and the population will be inverted at the end. Figure 2.2(b) shows the trace of the Bloch vector in the adiabatic frame, in which the projection of the torque vector on the Bloch sphere is fixed at the

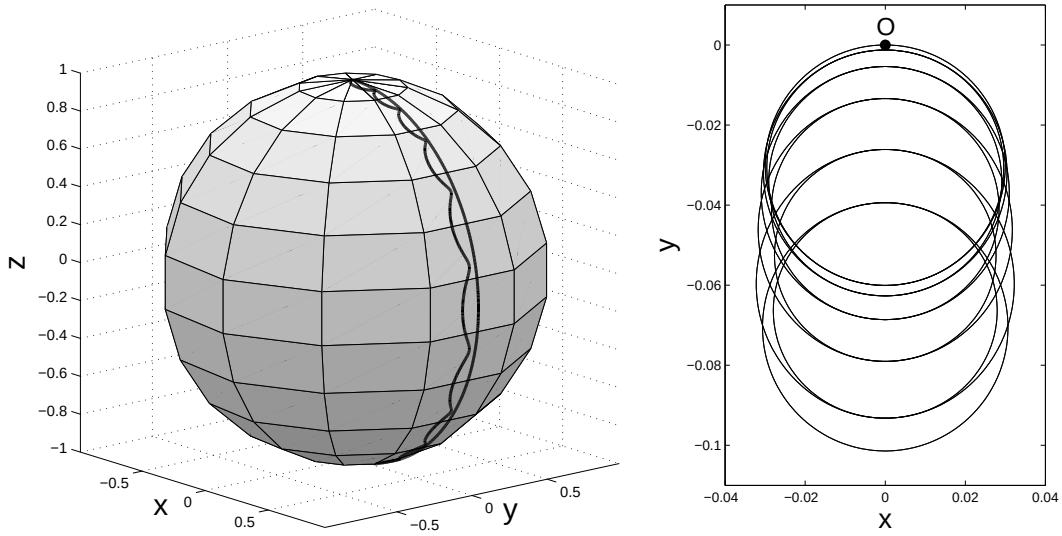

(a) Bloch sphere

(b) Adiabatic Frame

Figure 2.2: Adiabatic following of the Bloch vector along the torque vector of a modulated light field. In (a), the wavy curve connecting two poles is a typical trace of the Bloch vector on the Bloch sphere. The meridian close to it is the trace of the torque vector across the Bloch sphere . The light field is a cosinusoidally-chirped sinusoidal pulse with parameters $(\delta_0/\omega_m, \Omega_0/\omega_m) = (25.0, 18.724)$. In (b), the relative position of the Bloch vector and the torque vector is shown more clearly in the adiabatic frame. Notice that the scale of the plot is very small, so the deviation of the Bloch vector from the torque vector is actually small all the time, *i.e.* the adiabatic following.

origin, *e.g.* point O. The adiabatic frame itself rotates together with the torque vector (the precise definition of the adiabatic frame will be given in Section A.1). For adiabatic following, the deviation of the Bloch vector from point O is always small. Figure 2.1 is shown for a cosinusoidally-chirped sinusoidal pulse with parameters $(\delta_0/\omega_m, \Omega_0/\omega_m) = (25.0, 18.724)$. (The meaning of this expression will be clarified in Section 2.2.) The Bloch vector starting from and ending at the same point O over the duration of the pulse indicates a complete inversion.

The quantitative description of "slow enough" is the following:

$$|\vec{\Omega}(t)| \gg \frac{\mathrm{d}\theta}{\mathrm{d}t}. \tag{2.3}$$

where $\theta(t) = \arctan(\delta(t)/\Omega(t))$ is called the mixing angle. In terms of the Bloch sphere picture, $\theta(t)$ is the angle between the torque vector $\vec{\Omega}$ and the vector pointing to the north pole. Eq. (2.3) indicates that the angular frequency of the Bloch vector is much larger that the angular frequency of the torque vector at any time, so that the Bloch vector follows adiabatically.

If the sweep is not slow enough, the Bloch vector does not follow the torque vector adiabatically, and there is a small fraction of the population not inverted at the end of each sweep. Or in the dressed atom picture, there is some probability of the unwanted transition for the atomic population going to the "wrong" energy sheet at the end of each sweep. This transition is called the non-adiabatic transition. The probability for the non-adiabatic transition (P_{nad}) must be kept small for high efficiency of momentum transfer

via adiabatic rapid passage. In the next section we are going to study P_{nad} in detail.

2.2 Probability for Nonadiabatic Transition

In order to design sweep schemes with very small nonadiabatic transition probability P_{nad}, we need to study P_{nad} for various schemes and parameters. The ARP problem is in general a level crossing problem. The infinite time level crossing problem has been extensively studied [39, 40, 41]. However, to apply multiple repetitive ARP sweeps for optical force production, the pulse length must be finite and the nonadiabatic transition probability then has different properties.

Finite time sweeps make the numerical calculation of P_{nad} practical. Our first step was numerical integration of Eq. (2.2) for various finite time chirped pulses. For example, for a cosinusoidally-chirped sinusoidal pulse, the time-dependence of the intensity and frequency is described by

$$\begin{aligned} \Omega(t) &= \Omega_0 \cos \omega_m t \\ \delta(t) &= \delta_0 \sin \omega_m t, \end{aligned} \tag{2.4}$$

where $t \in [-\frac{T}{2},\ \frac{T}{2}]$, $\omega_m = \pi/T$. The special case of $\Omega_0 = \delta_0$ is analytically solvable and has been studied in some detail [42]. The consequence of this special case is that $|\vec{\Omega}|$ is constant so that $\vec{\Omega}$ satisfies

$$\frac{d\vec{\Omega}}{dt} = \vec{\omega}_m \times \vec{\Omega} \tag{2.5}$$

where $\vec{\omega}_m$ is an artificial constant vector. The nonadiabatic transition probability for this special case was found to be:

$$P_{nad} = \frac{x^2}{1+x^2} \sin^2 \frac{\pi}{2} \sqrt{\frac{1+x^2}{x^2}} \tag{2.6}$$

where the non-dimensional parameter $x = \omega_m/\Omega_0$. This analytic expression provides a series of values of $|\vec{A}|/|\Omega_0|$ where the probability of such non-adiabatic transitions is vanishingly small [42].

For the general case of $\Omega_0 \neq \delta_0$, the analytical solution is not available. However, numerical calculations are not restricted to the case of Eq. (2.5). Assuming the atom starts at the ground state, i.e., the initial Bloch vector $\vec{R}$ is at the South pole. We integrate for a single sweep (half cycle of Eq. (2.4)) and calculate the excited state component of the population. Ideally, $\vec{R}$ ends near the North pole and the population is nearly inverted, and $\hbar k$ is absorbed from the light field. The remaining ground state population at the end of the sweep, ρ_{gg}, gives the non-adiabatic transition rate of the process. In terms of the parameter r_3 in Eq. (1.5),

$$P_{nad} = \rho_{gg} = (1 - r_3)/2. \tag{2.7}$$

In Figure 2.3 we plot ρ_{gg} for various values of δ_0 and Ω_0, both in units of ω_m. For the case of $|\vec{\Omega}|$ constant (Eq. (2.5)), we reproduce the results of Ref. [42]. It corresponds to the diagonal of Figure 2.3 and the semi-circular paths in Figure 2.1. Other points on Figure 2.3 correspond to various elliptical trajectories [38]. The numerical calculation can be widely used for other finite

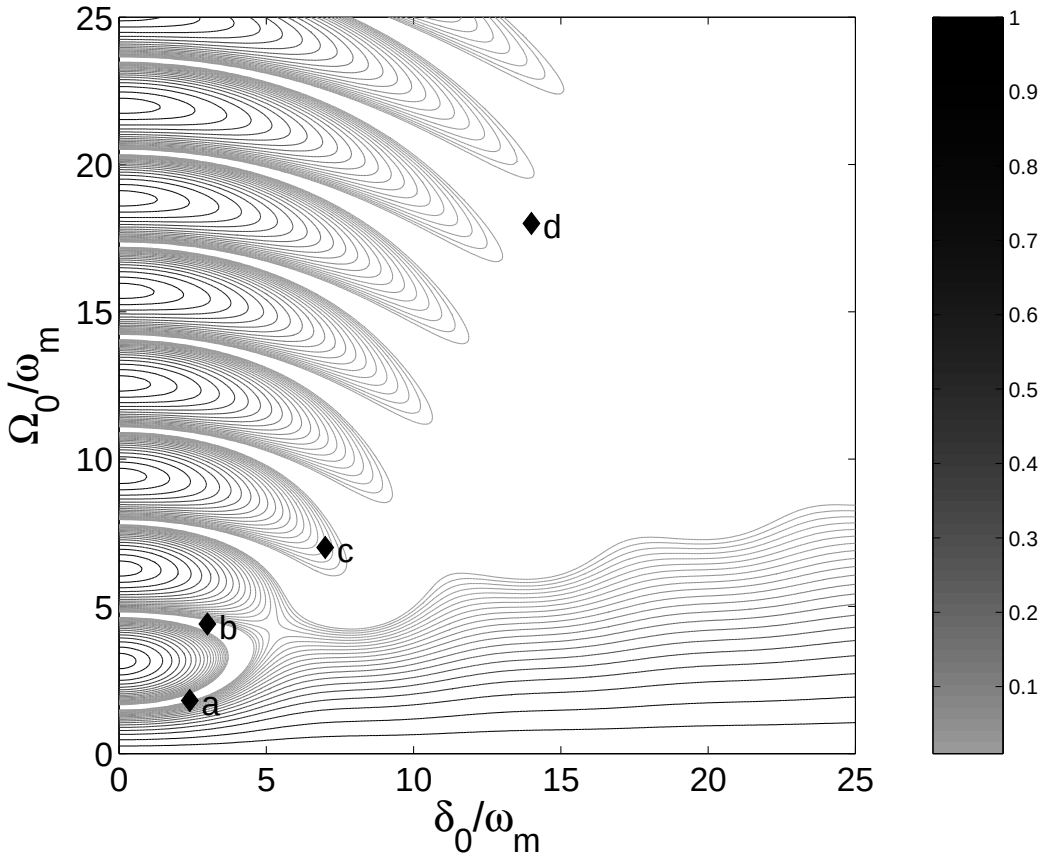

Figure 2.3: A contour plot of the numerical values of ρ_{gg} vs. δ_0 and Ω_0 after one sweep. The diagonal of this plot reproduces the results of Ref. [42], but our coordinate is the reciprocal of their "rapidity" parameter. The large open areas toward the upper right represent regions where $\rho_{gg} < .01$ so the probability of non-adiabatic transitions is negligibly small. Each contour line is a step of 0.01 so the point (c) is at $\rho_{gg} = 0.02$. Interest lies in those special areas that are close to the origin where ρ_{gg} is still tiny. The pathway along the vertical axis, $\delta_0 = 0$, that is punctuated by narrow white regions represents pulses of area $n\pi$ that also produce inversion ($n =$ odd integer). The indicated points represent $(\delta_0/\omega_m, \Omega_0/\omega_m)$ = (a) - (2.4, 1.8), (b) - (3, 4.4), (c) - (7, 7), and (d) - (14, 18) and will be referred to later.

time chirped pulses than the case given above.

To increase our understanding of the problem, further efforts were expended to find some analytical solution. This work has been done in collaboration with Dr. Tianshi Lu from the Computational Science Center, Brookhaven National Laboratory. Multiple unitary transformations have been applied to the two-level system driven by the finite time ARP pulses [43, 44]. A formal solution of the problem has been derived in the so-called rotating adiabatic frame and an approximate formula has been obtained for the nonadiabatic transition probability with generic symmetric finite time pulses. The results calculated with the approximate formula have been compared to numerical or analytical results for various pulses. We also discuss the similarity and difference between our finite-time ARP processes with two widely used infinite time level-crossing models - the Landau-Zener model [45, 46] and the Demkov-Kunike model [47, 48]. The asymptotic forms of the transition probability have been derived for the Landau-Zener regime, the "π-pulse" regime and adiabatic limit regime. The details of this work can be found in the Appendix A.

2.3 Periodic Adiabatic Rapid Passage

Large optical forces can be enabled by the multiple ARP sweeps with counter-propagating beams of high repetition rate. The force come from the coherent momentum exchange from atoms and the two light fields. In this section, we are going to discuss the behavior of the two-level system under periodic ARP pulses. This part of this work was published in [37].

The evolution of the Bloch vector $\vec{R}$ under an ARP pulse is determined

by equation (2.2). Ideally, an ARP pulse, *e.g.* a sinusoidal pulse described by $\Omega(t) = \Omega_0 \sin \omega_m t$, $\delta(t) = \delta_0 \cos \omega_m t$ for $t = 0 \rightarrow \pi/\omega_m$, nearly inverts the atomic population, and thus the Bloch vector $\vec{R}$ starting from the south pole ends near the north pole. Note that it is the same as described in Eq. (2.4) except a time shift. Here $t = 0$ is assigned to the start of the first sweep. Now we consider a second sinusoidal pulse, which is described by the second half cycle of the above formula for $t = \pi/\omega_m \rightarrow 2\pi/\omega_m$. Then $\vec{R}$ will be returned back to near the south pole. Note that $\vec{R}$ lying near the south pole after two sweeps doesn't guarantee the population inversion after one sweep, although the converse is true.

A strong force requires not only the population inversion but also that the two pulses have different $\vec{k}$-vectors. However, the evolution of $\vec{R}$ on the Bloch sphere does not depend on the propagating direction of the pulse. Thus two such sweeps of the laser parameters form a complete cycle which governs the evolution of the Bloch vector $\vec{R}$ from $t = 0$ to $T = 2\pi/\omega_m$. We consider a cycle as an operator that transforms $\vec{R}$ according to

$$\vec{R}(T) = U(T)\vec{R}(0) \tag{2.8}$$

where $U(T)$ is determined by the whole history of $\vec{\Omega}$ from $t = 0$ to T. We choose to view $U(T)$ as a rotation of the sphere instead. In fact, not only $U(T)$ but also $U(t)$ for arbitrary t is a rotation, and $\vec{R}$ remains on the surface of the Bloch sphere [37]. This view allows us to treat all cycles equally as multiple cycles are concerned since the rotation of the sphere doesn't depend

on $\vec{R}$. Although $U(t)$ may turn the sphere in a very complicated way, as illustrated in Figure 2.4, we are presently concerned only with the result at the end of each cycle and so consider only $\vec{R}(nT)$ where n is an integer.

In [37], we assume $\vec{R}(0) = (0, 0, -1)$. The first cycle transforms it to $\vec{R}(T) = U(T)\vec{R}(0)$, displaced from the South pole. Since $U(T)$ is a rotation, two angles θ_a (the polar angle) and ϕ_a (the azimuthal angle) are required to specify the rotation axis in the spherical coordinates, and a third angle α is required to specify the rotation itself. All these three angles are determined by the details of the laser parameter sweep $\vec{\Omega}(t)$, t from 0 to T. They are conceptually easy but not as easy to calculate. What's important is that the axis and rotation angle are the same for every repeated cycle. So the set of n points marking the values of $\vec{R}(nT)$ on the Bloch sphere lie on a circle that passes through the South pole for our chosen initial condition. The center of this circle of points $\vec{R}(nT)$ lies on the axis of rotation $(\theta_a,\ \phi_a)$. The circular locus of values of $\vec{R}(nT)$ has points separated by αr_0, where r_0 is the radius of the circle. If α is a rational multiple of 2π, the points cyclically overlap, and if not, they form a discontinuous circle. For the case where the parameters of the laser pulses are nearly ideal so that all $\vec{R}(nT)$'s are near the south pole, the radius of this circle $r_0 \ll 1$ since $|\vec{R}| = 1$. Thus it's most easily visualized when viewing the Bloch sphere from below, along its polar axis. Figure 2.5 shows a plot of our numerical results for a few particular cases. However, be cautious that $\vec{R}(T)$ being close to the south pole, *e.g.* αr_0 is small, does *not* necessarily mean $r_0 \ll 1$. In fact, the circle formed by $\vec{R}(nT)$'s can be as large as a meridian circle even when $\vec{R}(T)$ is very close to the south pole. The

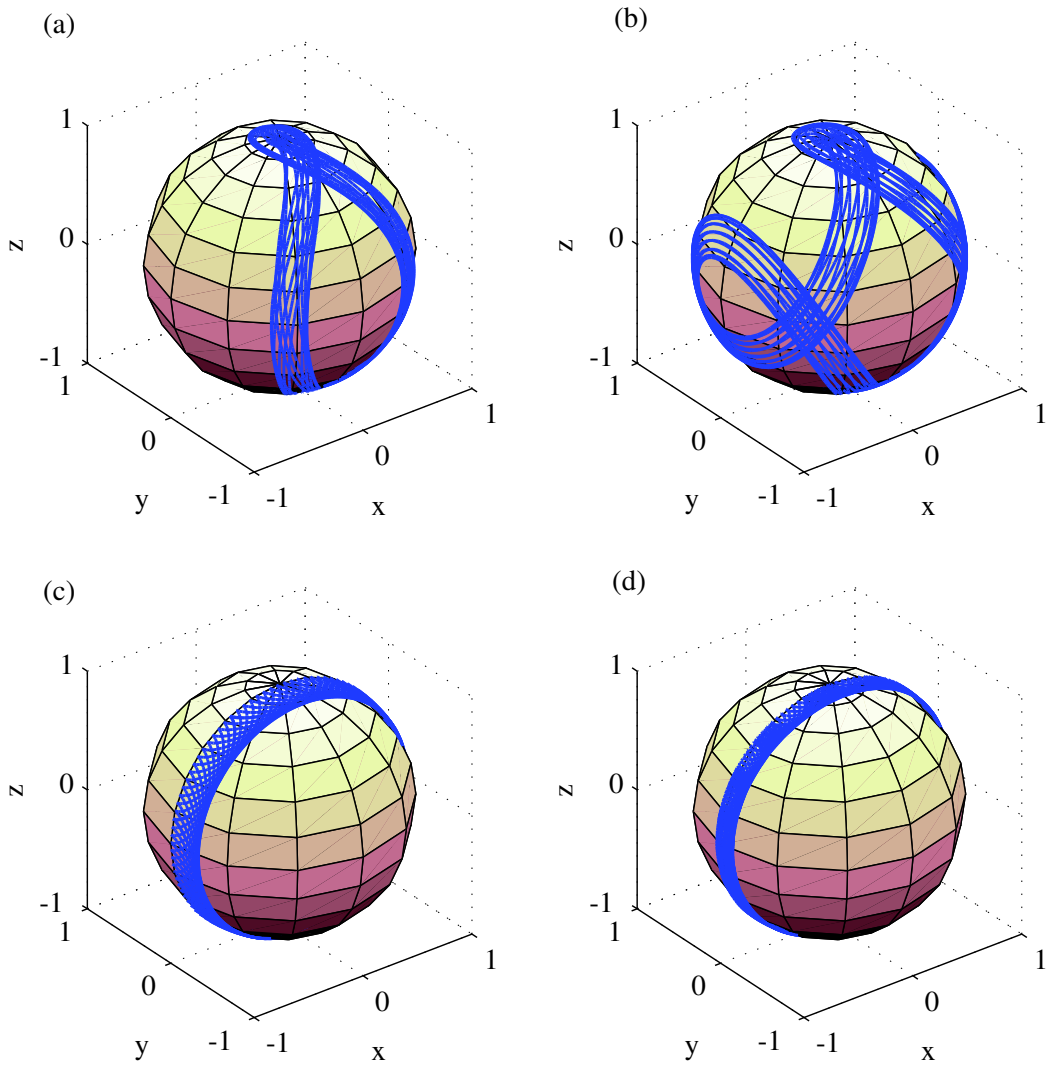

Figure 2.4: A set of trajectories of $\vec{R}$ on the Bloch sphere using the same laser parameters as in Figure 2.3 and Figure 2.5. The trajectories are confined to bands whose nearly constant width is essentially the same as the diameter of the circles of Figure 2.5.

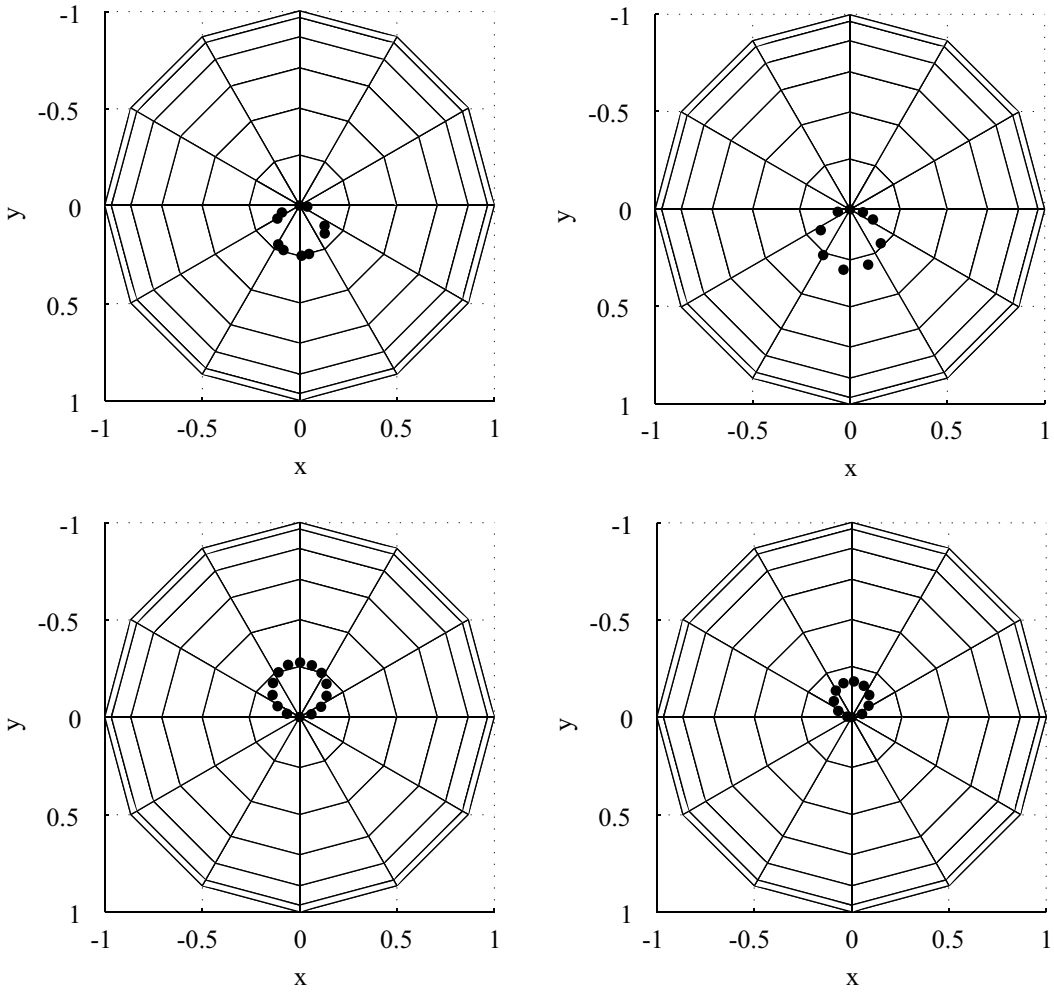

Figure 2.5: Plots showing calculated values of $\vec{R}(nT)$ on the Bloch sphere as viewed from the South pole. Each set of points lies on a circle whose radius and center depend on the sweep parameters. These parameters are the same as those for parts (a) through (d) of Figure 2.3. The points appear to be not evenly spaced (e.g., part (a)) because the rotation angle is large and more than one full rotation is shown.

quantitative analysis of r_0 will appear in Section 2.4.

In general the rotation $U(T)$ can be written as $U = e^{i\alpha \hat{J}\cdot\hat{u}/\hbar}$ where $\hat{u}$ is a unit vector along the rotation axis determined by θ_a and ϕ_a, and $\hat{J}$ is the spin-1 vector operator. The Floquet theorem can be applied here because of the periodicity of the linear equations being considered. There exist solutions that only change by a phase factor after each period T, which are the so called Floquet states. Floquet states on the Bloch sphere are located along the rotation axis. For these states, $U(nT)$ can be written as a phase factor $\langle U(T)\rangle^n$. This is mathematically analogous to the Bloch theorem.

As shown in Fig. 2.5, at the end of every cycle (pair of pulses), $\vec{R}$ is found somewhere on a circle. Since the trajectory $\vec{R}(t)$ of all the $\vec{R}(nT)$'s during the pulse can also be represented by the rotation of the Bloch sphere, that circle is preserved throughout the cycle. It is worth pointing out that all the $\vec{R}((n+\frac{1}{2})T)$ are lying on a circle passing through the north pole. The paths swept out by the tip of all the Bloch vectors are thus confined within a band swept by the circle on the Bloch sphere. A few such trajectories are plotted in Fig. 2.4.

2.4 Force from Periodic ARP Sequences

With some insight into the evolution of Bloch vector under periodic ARP pulses, we can now explore quantitatively the force associated with periodic ARP pulses. The force on the atom by the light field can be calculated using

the Ehrenfest theorem [49],

$$\vec{F} =< -\nabla H >= \frac{\hbar}{2}(r_1 \nabla\Omega_1 + r_2 \nabla\Omega_2),$$

where Ω_i represent the ith components of the torque vector $\vec{\Omega}$ in the Bloch equation Eq. (2.2), and r_i are the ith components of the Bloch vector $\vec{R}$. For one dimensional counterpropagating light fields of wave number k, as in our experiment, the force on an atom is

$$F = \frac{\hbar k}{2}((\vec{\Omega}_+ - \vec{\Omega}_-) \times \vec{R})_3, \tag{2.9}$$

where $\vec{\Omega}_+$ and $\vec{\Omega}_-$ are the torque vectors of the right and left propagating light respectively. When the counterpropagating light fields coexist at the same time, inter-beam multi-photon process can take place. The force on the atoms is then a complicated function of the overlapping light fields. On the other hand, if the two fields don't overlap in time, $\vec{\Omega}$ is either $\vec{\Omega}_+$ or $\vec{\Omega}_-$ at a given time. By using Eq. (2.2), the force calculation can be simplified as following,

$$F = \pm\frac{\hbar k}{2}(\vec{\Omega}_\pm \times \vec{R})_3 = \pm\frac{\hbar k}{2}\dot{r_3}.$$

The average force of a unidirectional light pulse is

$$\bar{F} = \pm\frac{\hbar k}{T_p}\frac{\triangle r_3}{2}. \tag{2.10}$$

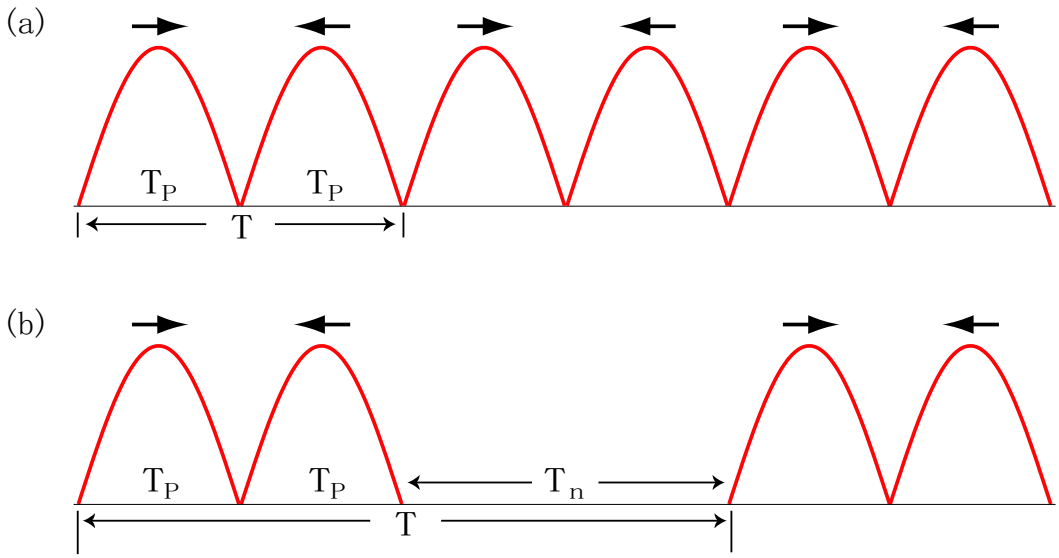

Figure 2.6: Schematics of alternating-directional chirped pulse trains. (a) Continuous chirped pulse pairs from counterpropagating light beams. Spontaneous emission is neglected here. (b) Chirped pulse pairs with half-period syncopation time to accommodate spontaneous emission. The directional force originates from the unsymmetric timing of the counterpropagating pulses.

If the atom is in the ground state initially, from Eq. (2.7), the average force of the pulse is

$$\bar{F} = \pm\frac{\hbar k}{T_p}(1 - P_{nad}), \tag{2.11}$$

where P_{nad} is the nonadiabatic transition probability of the pulse. In particular, $\bar{F} = \pm\hbar k/T_p$ if $P_{nad} = 0$, which represents the transfer of the entire momentum of a photon to the atom. For an atom starting from the excited state, the force by stimulated emission has the opposite sign to Eq. (2.11) .

Consider an atom in the periodic light field consisting of alternating-directional chirped pulses as shown in Figure 2.6(a). The counter-propagating pulses don't overlap in time. Suppose the atom is initially in the ground state.

If P_{nad} is zero for each pulse, then in each period the atom is lifted to the excited state by the first pulse and then brought back to the ground state by the second one, during which momentum of $2\hbar\vec{k}$ is imparted to the atom. Therefore the average force on an atom is $2\hbar k/T$ ($T = 2T_p$) for ideal ARP pulse train.

If $P_{nad} \neq 0$, the force is less than $2\hbar k/T$, and the reduction depends not only on P_{nad} but also on the relative phase of the counterpropagating light pulses. From the Hamiltonian of the atom,

$$H_0(t,x) = \frac{\hbar}{2}\begin{pmatrix} 0 & \Omega_\pm e^{i(\pm kx-\phi_\pm)} \\ \Omega_\pm^* e^{-i(\pm kx-\phi_\pm)} & 0 \end{pmatrix}, \tag{2.12}$$

where $\Omega_\pm$ and $\phi_\pm$ are the instantaneous Rabi frequency and initial phase of the right/left propagating pulses, and kx is the spatial phase variation with x being the position of the atom. We see that the relative phase of the counterpropagating pulses, $2kx$, varies by 4π in a wavelength of the light (1.083 μm in our experiment). The optical force observed in experiments is the average over all atoms in the atomic beam. For an atomic beam much wider than the wavelength of the light, *e.g.* the $\sim$ 0.3 mm wide helium beam in our experiment, the average can be taken over the atom position in a wavelength, or equivalently, over all possible relative phases between the counterpropagating pulses. Although the force is a complicated function of P_{nad} and the relative phase, it is shown in Appendix B that under the assumption of symmetric

pulses, the average force is

$$\overline{F} = \frac{2\hbar k}{T}(1 - \sqrt{P_{nad}}). \tag{2.13}$$

Eq. (2.13) is the average force on an atom at rest. For an atom moving at velocity v, the pulses seen by the atom are Doppler shifted by $\pm kv$. In general the Doppler-shifted fields are no longer periodic, except when kv is an integral multiple of $\omega_m = 2\pi/T$. For such kv's, $kvT = 2n\pi$ so the phases are shifted by $\pm 2n\pi$ after each period, equivalent to no shift. In Appendix B it is shown that under assumption of symmetric pulses, Eq. (2.13) still holds for $kv = n\omega_m$, but that P_{nad} is for the Doppler-shifted pulse.

2.5 Effect of Spontaneous Emission

All the theories discussed so far neglected spontaneous emission. The Optical Bloch Equation (OBE) including the contribution from spontaneous emission [49] is

$$\dot{\vec{R}} = \vec{\Omega} \times \vec{R} - \gamma \begin{pmatrix} \frac{1}{2}r_1 \\ \frac{1}{2}r_2 \\ r_3 + 1 \end{pmatrix}, \tag{2.14}$$

where γ is the spontaneous emission rate, and r_i is ith component of the Bloch vector.

The force on atoms can be calculated numerically by solving the OBE (2.14) and then applying Eq. (2.9). The kz-dependence of the light field should also be averaged out for the force calculation. A Fortran code originally

provided by the authors of [30] was modified for the ARP force calculation. Alternatively, based on the periodicity of the light fields, the OBE can be rewritten as a set of linear algebraic equations by expanding $\vec{R}$ and $\vec{\Omega}$ as truncated Fourier series [32]. The force can therefore be calculated by solving these equations. For adiabatic *rapid* passages, we can include the effect of spontaneous emission in a simple form, and calculate the force based on the results in Section 2.4.

First of all, the scheme shown in Figure 2.6(a) must be adjusted to accommodate spontaneous emission. Syncopation time between cycles can be introduced to produce a directional force, as sketched in Figure 2.6(b). The consequence is the same as we did in the bichromatic force by asymmetric timing of the counterpropagating π-pulses (see Section 1.6.1 and Figure 1.7). The optimal syncopation time is $T_n = 2T_p$, so that the pulsing period $T = T_n + 2T_p$ is twice the phase modulation period $2T_p$. In other words, the phase modulation frequency $\omega_{pm} = \omega_m$, the amplitude modulation frequency $\omega_{am} = \omega_m/2$, and the frequency corresponding to their common period is $\omega_c = \omega_m/2$. We used optimal syncopation time in all the experiments and numerical calculations of optical forces.

For $\omega_m \gg \gamma$ as in adiabatic rapid passages, the force with spontaneous emission is

$$F_{sp} = \kappa \bar{F}. \tag{2.15}$$

$\bar{F}$ is the average force without spontaneous emission as calculated in Section 2.4. The same argument as in Section 1.6.1 gives the reduction factor $\kappa \approx 1/2$. More careful calculation indicates that κ is a more complicated function of

P_{nad}. Generally speaking, κ is slightly larger than 0.5 for small P_{nad} and less than 0.5 for large P_{nad}. From Eq. (2.13) the actual force on atoms is

$$F_{sp} = \kappa \frac{2\hbar k}{T}(1 - \sqrt{P_{nad}}). \tag{2.16}$$

Be aware that the period T in Eq. (2.16) is $4T_p$, rather than $2T_p$ for the ideal scheme in Figure 2.6(a).

For sinusoidal light pulses sweeping at $\omega_m = 100\gamma$, the optical forces on atoms at rest are calculated and plotted in Figure 2.7. Figure 2.7(a) is from Eq. (2.16) with $\kappa = 0.6$; Figure 2.7(b) is from the numerical integration of Eq. (2.14) and the average of the force Eq. (2.9) over time. They agree qualitatively. The reason for $\kappa > 0.5$ for small P_{nad} is that for an atom in the ground state at the beginning of the second pulse in a pair, the subsequent ARP process is more susceptible to spontaneous emission as the atom is in the excited state during the syncopation time.

Detailed comparison with the numerical integration of the OBE (2.14) revealed that Eq. (2.16) is only qualitatively correct for moving atoms. The actual force is smaller than the prediction of Eq. (2.16) when P_{nad} is large. The reason is that for a larger P_{nad}, an atom initially in the ground state is more likely to be in the excited state during the syncopation time and thus more susceptible to the spontaneous emission.

Nevertheless, Eq. (2.16) can be used to estimate the velocity capture range of the optical force. With $P_{nad} = 0$ for rest atoms, the velocity capture range can be estimated as the velocity which shifts $P_{nad} = \frac{1}{4}$, so that the force

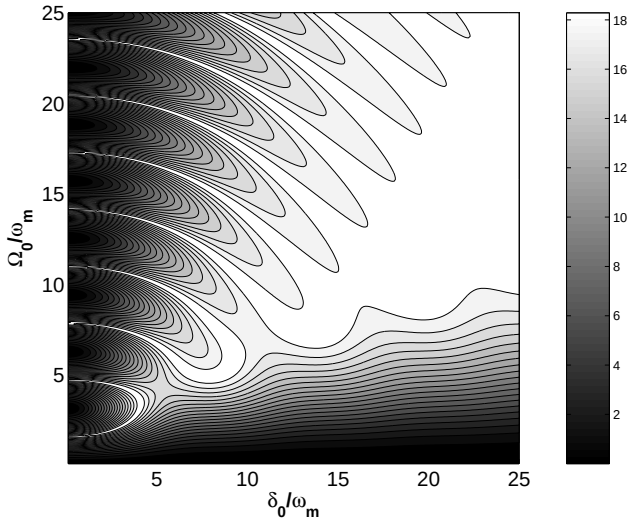

(a) Force Estimation by P_{nad}

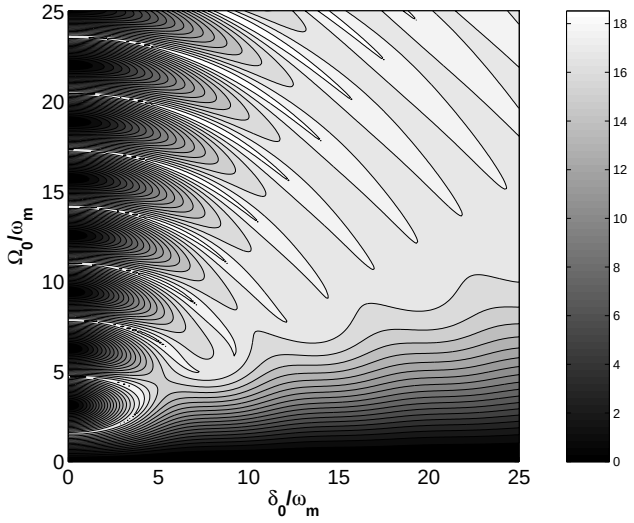

(b) Force from Numerical Integration of OBE

Figure 2.7: Force on rest atoms by sinusoidal light pulses. Spontaneous emission is included. $\omega_m = 100\gamma$. (a) is obtained from Eq. (2.16) with $\kappa = 0.6$. (b) is from the solution to Eq. (2.14). The force is plotted in unit of F_{rad}.

drops to half of the maximum value. In ARP, $\Omega' = \sqrt{\Omega^2 + \delta^2} \gg \omega_m$. For moving atoms, the Doppler shifted torque vectors still have $\Omega' \gg \omega_m$ so long as $\delta_0 - kv \gg \omega_m$. Therefore the velocity capture range for ARP is roughly δ_0/k, much larger than γ/k for radiative force. This is confirmed below by the numerical integration of the OBE (2.14). For other types of pulses, we can estimate the capture range via the approximate formulas for P_{nad} in Section A.1. For example, the velocity capture range of π-pulses is about ω_m/k, which is narrower than that for ARP. The derivation is omitted.

Comparison of optical force for various schemes

Next we compare the force and its velocity capture range for various force schemes with the same period. All calculations were done by the Fortran code that numerically integrates the OBE [30]. The force profile for π-pulse, ARP, and bichromatic schemes are plotted in Figure 2.8. The common sweeping frequency $\omega_m = 100\gamma$. The sinusoidal π-pulse beams have Rabi-frequency $\Omega_0 = (\pi/2) \times \omega_m$. The parameters of the sinusoidal ARP pulses locate at the right end of the first loop in Figure A.4(c), namely, $\delta_0 = 4.1 \times \omega_m$ and $\Omega_0 = 3.39 \times \omega_m$. The syncopation time included for both π-pulse and ARP schemes is illustrated in Figure 2.6(b) so that the $T = 4T_p = 4\pi/\omega_m$. The bichromatic laser beams have detuning $\pm\omega_m/2$ and optimal Rabi-frequency $\Omega = \sqrt{6}\omega_m/2$ (amplitude of beat wave) for $\pi/4$ phase delay. The period of the field is also $T = 2\pi/(\omega_m/2) = 4\pi/\omega_m$. For atoms at rest, the force of π-pulse and ARP sequences are about half of the force of bichromatic beams. However, the velocity capture range of π-pulse sequence is about double of

that for bichromatic beams, and the capture range of ARP sequence is even wider. The width of the velocity capture range agrees with the estimation by Eq. (2.16), namely, the capture range of π-pulse $\sim \omega_m$, while that of ARP pulses $\sim \delta_0$. The wide capture range of ARP pulses enables large deflection of the atomic beam.

The following example shows that the actual force profiles in our experiments are not symmetric with respect to the velocity. The left and right propagating pulses in the calculations so far have opposite frequency sweeping (type (a) or (b) in Figure B.2) so that the frequency sweeping is continuous between pulses, except for Figure 2.7(b) where actual pulse trains was used. In our experiments, actual counterpropagating pulses have the same frequency sweeping (type (c) and (d) in Figure B.2), since the light in one direction is obtained by retroreflection of the light in the opposite direction. The force profile for pulse trains of type (a) and (b) are the same except for several dopplerons. But the profile for (c) and (d) types are noticeably different, as plotted in Figure 2.9 for ARP pulse trains that have the same parameters as the ARP pulses in Figure 2.8. Apparently, (c)-type pulse pairs, in which each pulse is chirped from below resonance to above resonance, might be more favorable for the deflection experiment as the force is larger in the direction of the acceleration, so that the atom can attain a higher deflection velocity. An explanation is that the positive moving atoms spend less time in the excited state for a (c)-type pulse train due to the Doppler shift, so that the influence of spontaneous emission is weaker; while the reverse is true for a (d)-type pulse train.

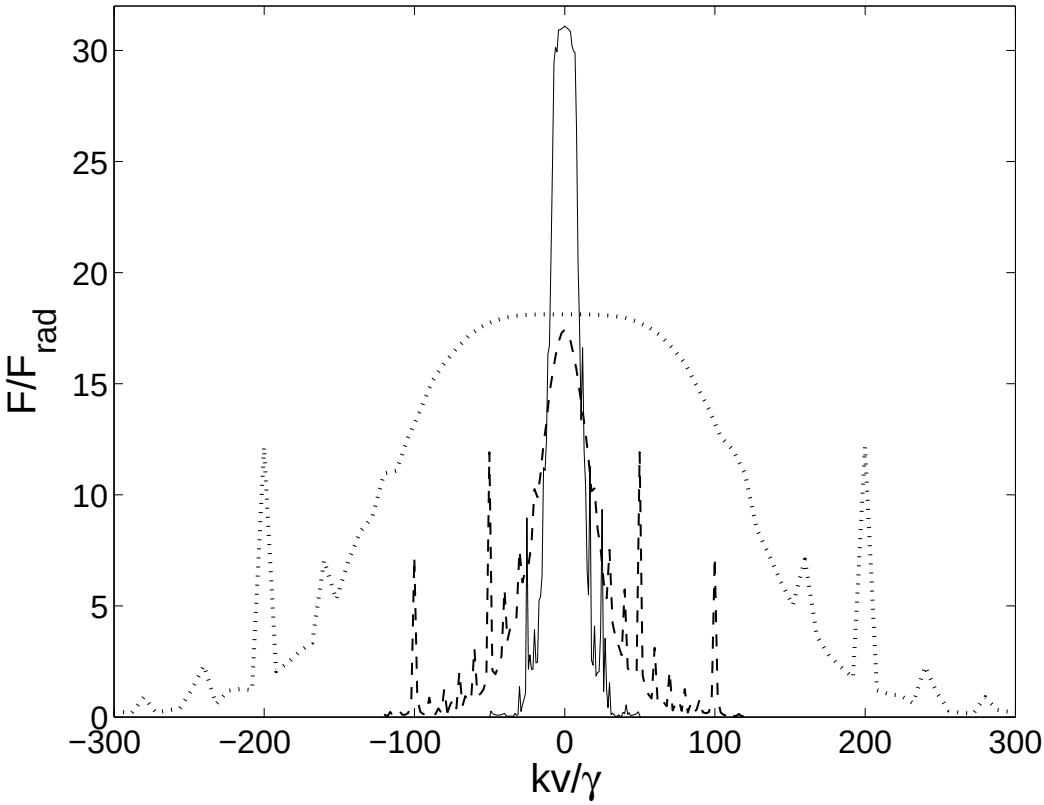

Figure 2.8: Comparison of velocities dependence for various force schemes. Dashed curve: sinusoidal π-pulse beams with $\Omega_0 = 157\gamma$; dotted curve: sinusoidal ARP pulses with $\delta_0 = 410\gamma$ and $\Omega_0 = 339\gamma$. Chirping frequency $\omega_m = 100\gamma$. Syncopation time $T_n = 2T_p$ has been introduced in both schemes to produce the directional force so that $T = 4T_p = 4\pi/\omega_m$. Solid curve: bichromatic laser beams of $\pi/4$ phase delay with detuning $\pm\omega_m/2$ and $\Omega = 122\gamma$ for two frequencies.

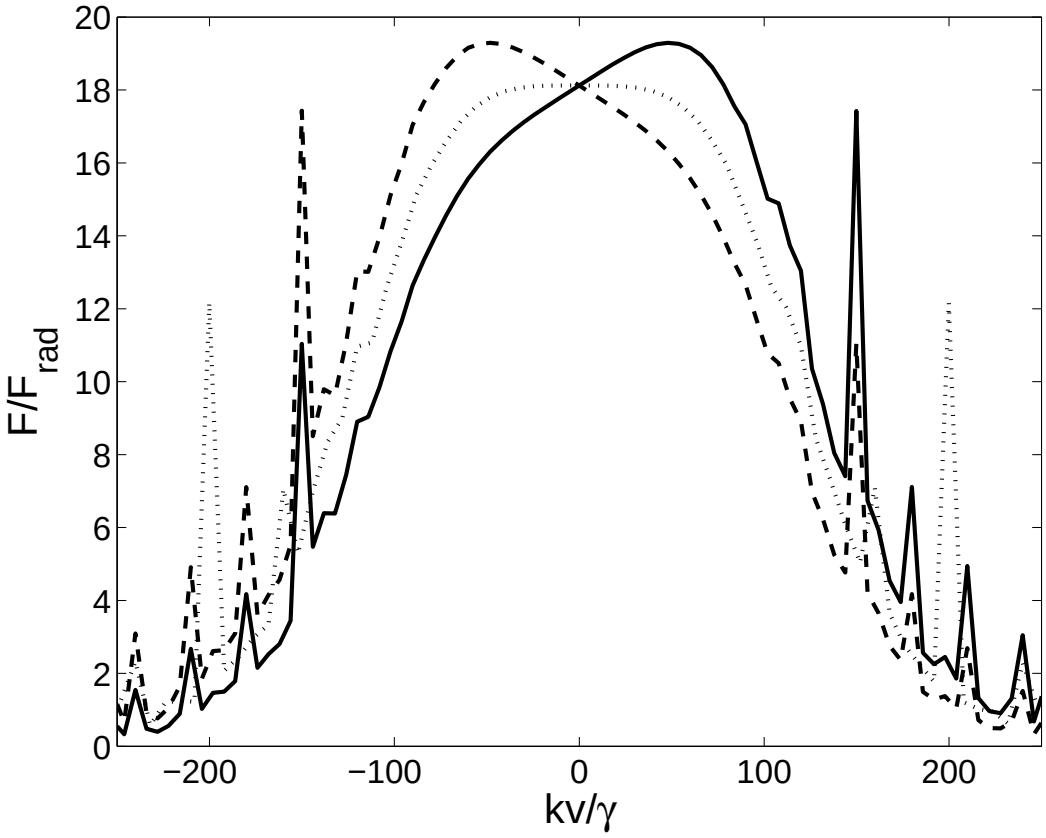

Figure 2.9: velocity dependence of the of sinusoidal pulse sequences with different chirping directions. $\omega_m = 100\gamma$, $\delta_0 = 410\gamma$, $\Omega_0 = 339\gamma$. Solid curve: pulse trains of type (c) in Figure B.2; dashed curve: pulse trains of type (d) in Figure B.2; dotted curve: pulse trains of type (a) and (b) in Figure B.2.

Chapter 3

Metastable Helium Apparatus

The "two-level atoms" used in this experiment are He atoms in their 2^3S_1 to 2^3P_2 transition. The effective "ground state" 2^3S_1 is actually the Metastable state of ^{4}He atoms. The reason it can serve as an effective "ground state" is that the 2^3S_1 state of He has a very long lifetime ($\sim$8000 s), much longer than the experiment time scale (a few μs), due to the prohibition of the electric dipole transition to the ground state. ^{4}He has no nuclear spin. The ground state is 1^1S_0, which has total electronic spin 0, while the metastable state 2^3S_1 has total electronic spin 1. The electric dipole transition selection rules $\Delta S = 0,\ \Delta L = \pm 1$ are not satisfied for the transition from 2^3S_1 to 1^1S_0, which makes the 2^3S_1 state nearly isolated from the ground state. It is thus the metastable state and called He*. A energy level diagram of He with the relevant energy levels is shown in Figure 3.1. The lifetime of the excited state 2^3P_2 is 98 ns. The transition wavelength from 2^3S_1 to 2^3P_2 is 1083.33 nm. The characteristic data of this atomic transition is listed in table 3.1. The production and detection of the He* is the subject of this chapter.

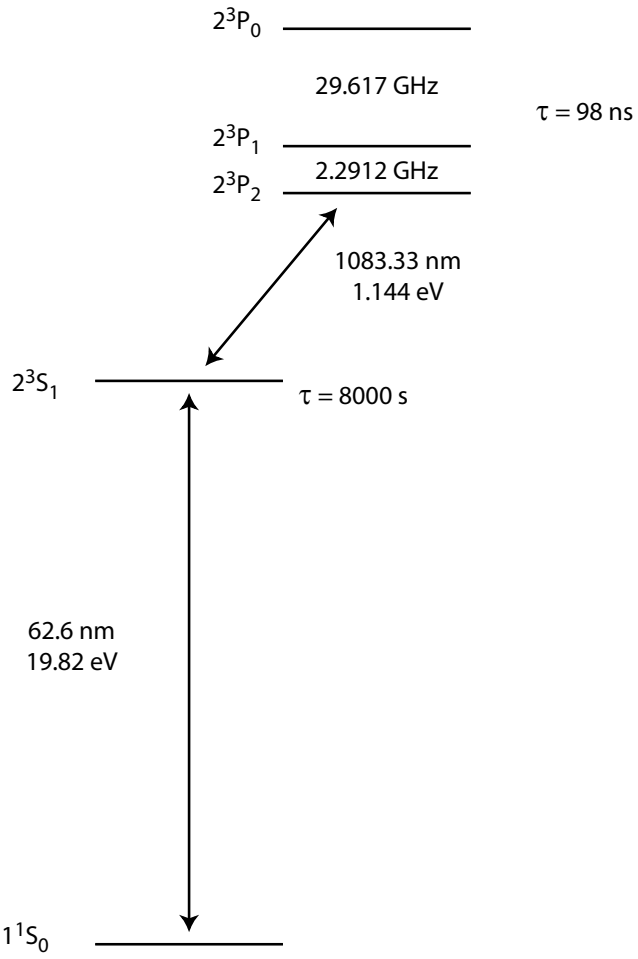

Figure 3.1: Energy level diagram for He and the transitions of interest. The 2^3S_1 state is called the metastable state because of its 8000 s life time. The metastable state is an effectively "ground state" on the timescale of our experiments. (Note that the levels are not drawn to scale.)

Quantity (unit)	λ (nm)	$\hbar\omega_a$ (eV)	τ (ns)	$\gamma/2\pi$ (MHz)	I_{sat} (mW/cm^2)	$\omega_r/2\pi$ (kHz)	v_r (cm/s)
	1083.33	1.144	98.04	1.62	0.17	42.46	9.2

Table 3.1: Characteristic values for the $2^3S_1 - 2^3P_2$ Helium transition used in the experiment, taken from [4].

3.1 Metastable Helium Source

As shown in Figure 3.1. The long-lived He* state is 19.82 eV above the ground state. This makes it a powerful tool to do neutral atom lithography [50, 51]. The He* source that is currently in use in the lab was originally built at Utrecht University in the Netherlands. It was assembled and tested at Stony Brook by Matthew Cashen and Michiel van Rijnbach in late 1998, and has been in good working condition since the spring of 1999[52, 53]. The source has mainly been used to study the polychromatic force on atoms.

The source is based on the "reverse flow" design of Kawanaka et. al. [54]. Modification has been made by the group at Utrecht [55, 56] to produce cooler He* beams. He atoms are excited to the metastable state by a DC glow discharge. The interior of the source has a long metal rod with a 1 mm diameter tungsten needle attached to the end. The rod is lying along the axis of 1 cm diameter pyrex glass tube. The needle tip is pointed to the tapered end of the glass tube. The outside is a stainless steel coaxial jacket which can be filled with liquid nitrogen (LN_2). The glass tube fits snugly in the LN_2 cooled jacket through a teflon spacer. The diagram of the source is shown in 3.2. He gas flows into the vacuum chamber through the gap between the glass tube and the LN_2 filled jacket, and is thus cooled before going into the tapered end of the glass tube. Most of the atoms are pumped out through the inside of the glass tube by a mechanical pump. The spacer that keeps the needle centered in the glass tube has several channels cut into it to allow appropriate gas flow. At the front end of the LN_2 filled jacket is a grounded aluminum plate with a 0.5 mm aperture, which is called the nozzle plate and

serves as an anode for the discharge source. The distance between needle and the anode can be adjusted by a motion feedthrough connected to the end of the needle rod. The remaining gas flow sustains a glow discharge between the tungsten needle and the nozzle plate as a negative high voltage (1 to 3 kV) is applied to the needle. The discharge produces He* via electron impact and/or ion-electron recombination. However, most of He* produced inside the dense plasma is almost immediately quenched by collisions. Only the atoms produced outside the plasma, in the dilute afterglow of the discharge directly behind and past the nozzle plate, can survive and fly to the interaction region [57, 54]. Therefore, the anticipated He* production rate is low ($\approx 10^{-5} - 10^{-4}$) [4]. The discharge source also produces other short-lived excited states, *e.g.* 2^1P_1, which decay quickly to the ground state and emit 20eV UV light which carries energy similar to that of the He*. Other than these components, the source beam is made up of electrons, ions, visible light and mainly ground state He atoms. Also shown in figure 3.2, directly following the nozzle plate is a second plate with a 0.5 mm aperture, called the skimmer. The skimmer plate serves a dual purpose. First, it geometrically defines the He* beam. Second, it allows for differential pumping between the source chamber (the region in front of the skimmer) and the He* beam chamber (the region behind the skimmer).

The reliable production of a discharge and subsequent metastable beam is contingent upon many conditions, which include the shape and the cleanliness of the glass tube, the sharpness of the tungsten needle and the quality of the anode surface. A problem with any of them can cause the discharge source to

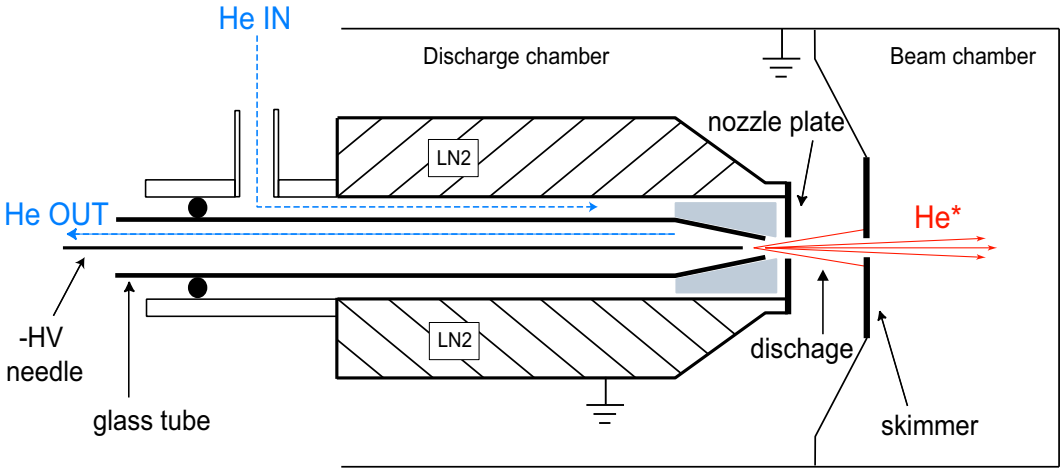

Figure 3.2: Cross sectional schematic of the DC discharge source for metastable helium. Ceramic spacer on the tungsten needle is not shown.

fail. Trial and error were needed to get them right initially [52].

The pressure in the discharge region and voltage on the discharge needle are also very important parameters. The discharge begins to run stably for discharge currents above 2 mA. It could be run up to 12 mA or higher with higher pressure or higher voltage. However, an increasing current results in a "hotter" discharge, and thus a faster He* beam. We typically chose 6 mA as a trade-off between metastable production and beam velocity. The pressure in discharge region can not be measured accurately, but it relies on the pressure of gas entering the source and the speed at which it is pumped out. The inlet pressure can be adjusted with a fine needle valve, and was measured by a Granville-Phillips Convectron Gauge placed in the helium gas inlet. The gauge was read by a Terranova Model 926 Scientific Gauge Controller. Such devices are typically calibrated for nitrogen (air) so a conversion chart for

other gases had to be acquired from Duniway Stockroom, the manufacturer of the controller. The inlet He pressures read from the chart are typically 5 to 10 Torr. Another Granville-Phillips Convectron Gauge at the outlet indicates a pressure of 1.2 Torr. Running at lower pressures results in higher metastable production rate, but also causes the discharge to become unstable. After finding the optimal operation condition, the source can operate reliably for long periods of time without significant change in the properties of the He* beams. However, the sharpening of the needle and cleaning of the parts may need be redone every two years. The source output flux is $\approx 10^{14}$ He* atoms/s·sr [52, 53]. During this experiment, the typical discharge voltage is 2500 V and the discharge current is 6 mA. Proper production of metastable atoms can be assured by monitoring the current and by viewing the color, intensity, and shape of the discharge glow.

The characterization of the He* beam after the skimmer plate was done by Matt Cashen [52]. The longitudinal velocity of the beam was characterized by a time of flight (TOF) measurement. A mechanical chopper was used in the TOF measurement to pulse the beam. The signal intensity versus the arrival time (different for atoms moving with different velocities) was detected by an amplified Multichannel plate (MCP) downstream. This method allows the separating the atomic signal from the UV signal, which provides a zero point for time. TOF measurements for this source were carried out for a wide variety of operating parameters by Matt Cashen. The results were shown to be highly repeatable. The longitudinal velocity distribution of the He* beam for 6 mA discharge current is shown in Figure 3.3, where the He* atom velocity

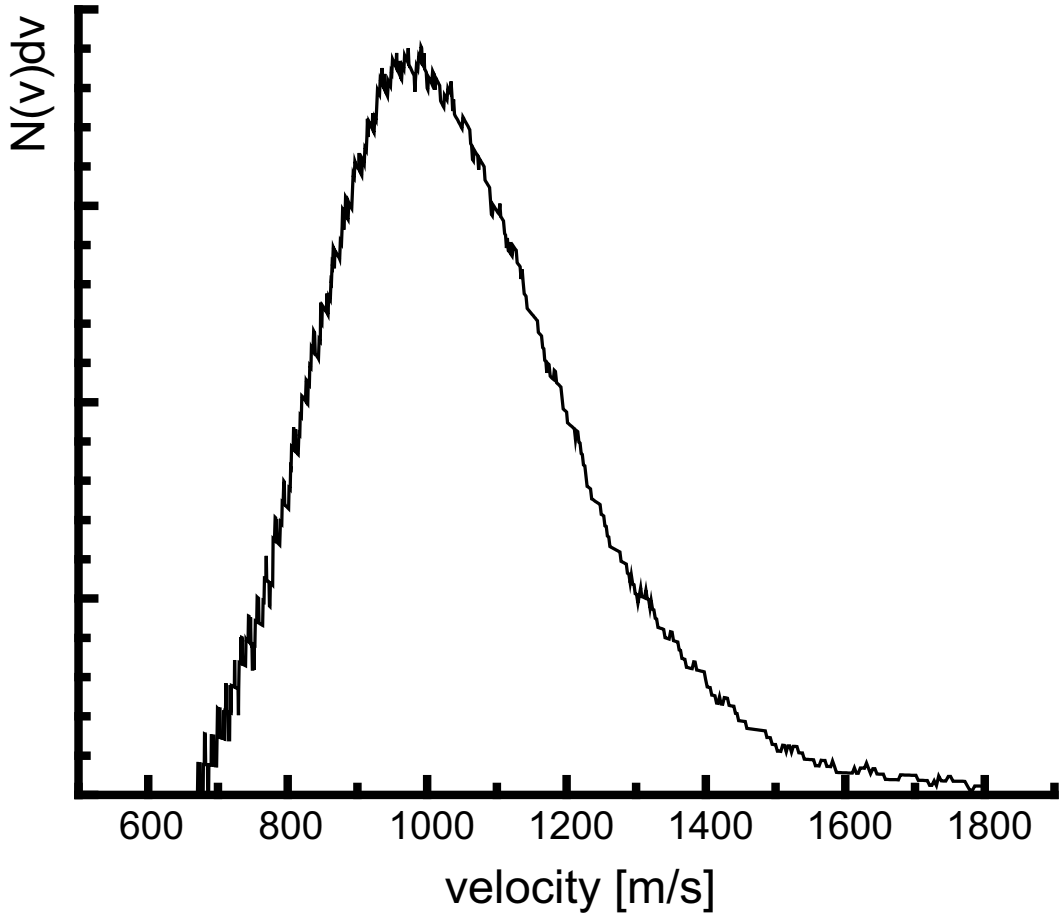

Figure 3.3: Metastable atom longitudinal velocity distribution with a discharge current of 6 mA [52].

is peaked at $\approx$ 1000 m/s with a FWHM of $\approx$ 400 m/s.

3.2 Metastable Helium Beamline

The current Metastable Helium beamline was modified from the one for doing bichromatic collimation experiment [28]. The design of the current system is optimized for doing neutral atom lithography [58]. The bichromatic force collimated He* beam is used for this purpose. The whole beamline can be divided into four sections, the source chamber, the interaction chamber, the detection chamber and the lithography chamber. These sections are named as per the lithography experiment. The last three all together are called the beam chamber. The main beamline is made from 4" diameter stainless steel tubes. All connections are copper sealed Conflat flanges, which support ultra-high vacuum. The total length of the beamline is about 1.2 m. The side view of the vacuum system is shown in Figure 3.4.

The source chamber and the beam chamber are each pumped by a Pfeiffer model TPH 330 turbomolecular pump, which is backed by a mechanical pump. Separated by the skimmer plate with a 0.5mm aperture, the source chamber and He* beam chamber are maintained at different pressure while the discharge source is running. The pressure between the nozzle plate and the skimmer plate is $\approx$ 10^{-4} Torr, while behind the skimmer the pressure remains at a few $\times 10^{-6}$ Torr. The pressures are measured by two Kurt J. Lesker model G100F ion gauges. Low pressure is needed in the He* beam chamber to reduce collisions between the metastable beam atoms and background gas in order to minimize collision induced decay of the He* atoms (Penning ionization [59]).

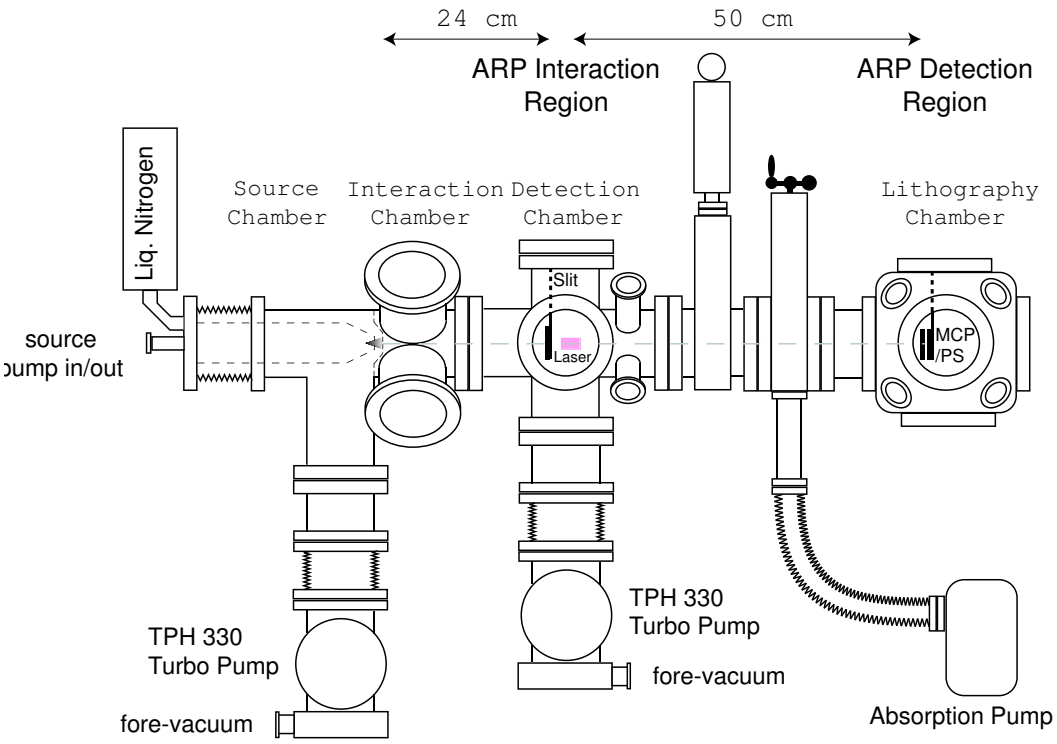

Figure 3.4: Diagram of the vacuum system viewed from the side. The turbo pumps are attached to the system through vibration isolators. All seals are conflat except those connecting the gas flow and the vibration isolators. The name of the chamber are as per the lithography experiment. The interaction region and the detection region for ARP experiment and the relevant distances are indicated above the vacuum system.

The distance between the nozzle plate and skimmer, as well as their mutual alignment, can be adjusted via a bellows which connects the source to the source chamber. The typical separation of the two apertures are about 0.5 to 1 cm.

The interaction chamber is a six-way-across directly welded onto the Tee of the source chamber so that the source and skimmer protruded into an area

with considerable optical access. Both the Tee and the six-way-across are of 4" outer diameter. The source chamber turbomolecular pump was connected to the downward facing port of the Tee. The source was mounted through one arm of the tee. The other arm of the Tee and one arm of the 6-way cross had to be cut to have them welded together. A wall was placed in between the two sections with a section cut from a conical reducer welded for mounting the skimmer plate. The conical section and skimmer protruded 1 cm into the region directly under the viewports of the 6-way cross. The other two axes of the 6-way cross were at 45° to the horizontal plane. Flanged glass viewports were mounted on the four ports for the optical access of the bichromatic laser beam. This allows the bichromatic collimation beam to be applied very close to the skimmer plate and thus enables efficient collimation of the atomic beam before it expands too far. The glass windows have 4" diameter and are anti-reflected coated for 1083 nm and 389 nm. On top of the vacuum chamber, up against the 6-way cross on the source side, a tube with a small window was welded in place to allow viewing the afterglow of the discharge between the nozzle and skimmer.

The next section is another six-way-across used as the detection chamber for bichromatic collimation [53]. Its arms are rotated 45° relative to the interaction chamber so that the other two axes of the 6-way cross were at the horizontal and the vertical plane. A Multichannel Plate/Phospher Screen (MCP/PS) detector assembly was mounted on the top port with a linear motion feedthrough for the detection of the collimated beam. The bottom port was connected to the beam chamber turbomolecular pump. Each side port

also has a flanged glass viewport for optical access. These viewports are anti-reflected coated for 1083 nm light. An additional four ports (1 1/2" tube OD), each of these mounted at 45°, was used to mount Stainless Steel detectors (SSD), ion gauge etc. The SSD was used to do two dimensional scans of the collimated He* beam.

Following the detection chamber, is a Thermionics VLS-600/N shutter and then a Thermionics PFG-TLG-4000H/R gate valve. A Kimball physics $4\frac{1}{2}$" Multi-CF spherical cube (MCF450-SC60008-A) is attached at the end of the He* beamline. This section was designed for doing atomic lithography. The shutter and the gate valve are used to close the vacuum system in loading a sample. A roughing line was connected from the bottom of the gate valve to an absorption pump. This allowed the pumping down of the lithography chamber before opening the gate valve. A back SSD and a sample holder were fitted in the lithography chamber. Since this is not going to be used for the ARP experiment, a detailed description will not be presented here.

The bichromatic collimation experiment was working well for atomic lithography. However, the collimation itself is a bit tricky and tedious and can be very time consuming. One motivation to study the force related to ARP sequences is to make use of it for He* beam collimation. The force is believed to be more robust than the bichromatic force. Of course the physics of ARP force is very intriguing itself. To fit the ARP experiment in the current beamline without interfering with the lithography experiment was a real challenge. The final idea is to hang a 0.3 mm vertical slit (mounted on a 1.4" × 1.4" plate) onto the MCP/PS detector in the detection chamber. A 4" push-pull lin-

ear motion feedthrough (Huntington L-2121-4) was purchased to have enough motion range to move the MCP/PS/Slit assemble out of the way for doing lithography. By bringing the motion feedthrough down, the MCP/PS detector can be used to monitor the bichromatic collimation. In doing the ARP experiment, the linear motion feedthrough was set to position the slit in front of the He* beam for better geometrically defining the atomic beam. The distance between the skimmer plate and the slit is 24 cm. The interaction region for the ARP experiment is about 1 cm behind the slit. The big 4" windows in the horizontal axis of the detection chamber give optical access for the ARP beam. The detection of the ARP force is done by inserting another MCP/PS detector assembly through the flange of the $4\frac{1}{2}$" spherical cube with a 2" linear motion feedthrough (Huntington L-2211-2). The MCP/PC detector is 50 cm downstream of the interaction region of the ARP beam. It can be move in and out of the way of the He* beam by using the motion feedthrough.

3.3 Multichannel Plate and Phosphor Screen Detector

As described in Section 3.1, the helium atom in the metastable state carries ∼20 eV internal energy. This internal energy can be released when the He* atom experiences a collision, such as striking a metallic surface, where the ejection of an electron results. This can be used for the detection of the He* beams. In our experiment, to measure the transverse deflection of He* beams, a MCP/PS detector was used to map the distribution of the He* 50 cm behind the interaction region. The MCP/PC detector is a very useful way to analyze the atomic beam since it can produce a real-time, cross sectional

imaging of an atomic distribution.

The MCP is a thin disc of lead glass comprising of many channels oriented parallel to one another and perpendicular to the surface of the disc. These channels have $\sim$10 μm diameter and form a hexagonal lattice with lattice spacings of 12 μm. When a He* atom strikes on the surface of a channel, an electron is produced. A negative bias voltage across the two surface of the MCP accelerates the electron into the channel, causing a cascade of secondary electrons. This results in electron multiplication. The MCPs we used in the lab were purchased from BURLE (part #'s 30286). The active area of the MCP has a 25 mm diameter. The multiplication factor is up to $\approx 10^3$ for -1000 V bias voltage. We typically use the MCP at -500 to -800V.

A phosphor screen was placed directly behind the MCP (see Figure 3.5). The phosphor screen substrate is a 1.5 inch diameter glass plate. A thin layer of gold coating was first evaporated on the glass for conductivity. A layer of P20 phosphor particles was then deposited on top of the gold coating. The phosphor layer has a diameter of 1.25 inches. A positive high voltage (typically +1000 to +2000 V) applied on the gold layer accelerate electrons from the MCP to the phosphor screen. Electrons impacting cause the phosphor to fluoresce with visible light. The brightness on a given spot depends on the electron density, and thus on the number of He* atoms hitting the MCP at that spot. The phosphor screens we used were manufactured by James van House in Vancouver, WA.

The phosphor screen image was viewed from a side window of the lithography chamber by a CCD camera. A 35 mm $\times$ 50 mm front surface mir-

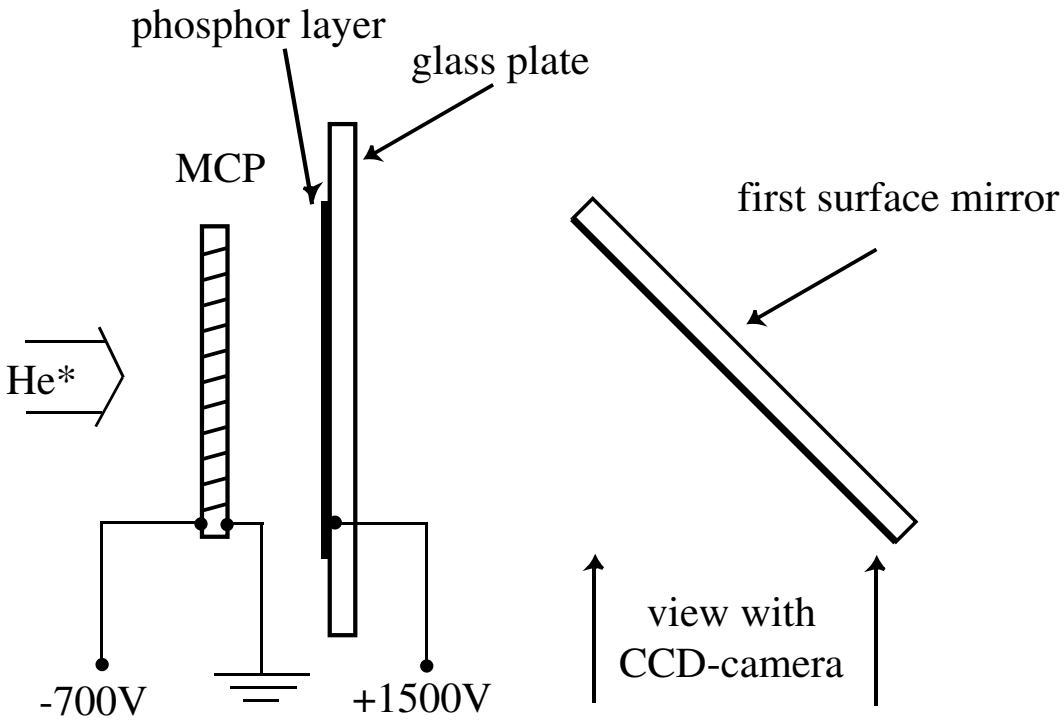

Figure 3.5: Schematic of the MCP/PS detector system for He* beam detection. The 45° mounted mirror was used to reflect the image through the side window of the vacuum chamber. Viewing of the image with a CCD camera is then possible without interference with atomic lithography at the end of the beam.

ror mounted at 45° to the MCP/PS detector was used to view the image through the side window. The mirror was glued on a piece of sheet metal and then mounted together with the MCP/PS detector with Kimball Physics standard eV parts. The whole assembly was then mounted on a linear motion feedthrough which fit through the top flange of the spherical cube. This allows the detector to move out of the way for atomic lithography. A TV tuner card (AVerMedia TV98) was used to grab and save the camera images onto a computer as bitmap files. The greyscale pixel value across the image is directly correlated to the brightness across the phosphor screen. Images analysis is primarily done with ImageJ, a public domain Java application developed at the National Institutes of Health, and Matlab.

Although it is very useful for real time observation of the atomic beam deflection, the MCP/phosphor screen has some severe limitations. A calibration of the correlation between atom flux and image pixel value is missing. Not only is the electron ejection efficiency of a He* atom from the surface of the MCP not exactly known, but also the sensitivity of the combination of MCP and phosphor screen to atomic flux is highly non-linear and non-uniform. The non-uniformities are mainly due to the aging of the phosphor screen under high flux impact. This makes quantitative measurement with the MCP/PS detector very difficult.

Chapter 4

ARP Light Production

The production of the ARP pulse sequence is the key of this experiment. In this chapter I will describe the optical system. The 1083 nm light originated from a Spectra Diode Labs diode laser. The chirped pulses needed for the ARP processes were generated by successively modulating the frequency and amplitude of the light with two $LiNbO_3$-based integrated-optic modulators. A fast InGaAs photo detector was used for the pulse profile measurement and two Fabry-Perot interferometers were built for the spectrum analysis. The high optical power required for the experiment was gained through two commercial Ytterbium-doped fiber optical amplifiers. Finally the optics that transport the light beam to interaction region are described.

4.1 The Diode Laser

The diode laser used for our experiment was a Spectra Diode Labs SDL-6702-H1 DBR laser, where DBR stands for Distributed Bragg Reflector. High performance, low cost, tunable diode lasers have gained wide popularity in

atomic and molecular physics experiments since their development. DBR lasers have a Bragg grating fabricated into the active region of the laser diodes. The grating serves as an internal wavelength selective element of the laser and also improves the frequency tunability and the long-term frequency stability. The availability of DBR laser sources at 1.08 μm have facilitated experiments involving He* since 1994 [60]. We have two SDL-6702-H1 laser systems in our lab. Their frequency control and stabilization were investigated by C. Avila [61] and they were put to use by M. Cashen [52] in polychromatic force experiments. One laser is used for bichromatic collimation of the He* beam for the lithography experiment and the other one is used in the ARP experiment described in this thesis. This product was discontinued by Spectra Diode Labs a few years ago but fortunately, replacements recently became available from Sacher Lasertechnik.

The SDL-6702-H1 laser comes in a standard 8-pin TO-3 window package with a thermistor and a thermoelectric cooler (TEC) included. Two commercial laser diode controllers were used for laser operation - a Newport model 325 temperature controller for temperature stabilization and a Newport 505 current controller for injection current supply. The current can be modulated up to 500 kHz by applying a low-level signal to the controller. This is very useful for laser frequency locking.

4.1.1 The Mechanism of Laser Frequency Tuning

Laser frequency control and stabilization is a very demanding task for experiments in atomic and molecular physics. The frequency of a diode laser

is tunable via adjusting its temperature and injection current, and via optical feedback [62]. Temperature tuning provides the coarse control and current tuning provides the fine control. Finer control and frequency narrowing can be achieved via optical feed back.

The frequency tuning coefficients of the DBR laser via temperature and injection current was previously measured to be -22 GHz/°C and -300 MHz/mA [61]. For our experiment, the thermistor was set at 9.73 KΩ, corresponding to a temperature slightly lower than the room temperature (∼25 °C). The injection current was set at 150 mA. The operating points were chosen to put the laser frequency reliably on the He* atomic transition at $\lambda = 1083$ nm with a moderate power output level (∼25 mW). An "extended cavity" (EC) scheme is used for our laser system as the controlled optical feedback [63]. As shown in Figure 4.1, the EC is formed between the back Bragg reflector of the DBR diode and an external high reflectivity mirror (> 99% reflectivity) in an angled configuration. A 30/70 beam splitter was used to complete the EC and also served as the output coupler. A piezo electric transducer (PZT) driven by a home-built, high voltage controller is attached to the external mirror for adjusting the EC length and thus ramping the laser frequency.

In order to insulate the EC laser from environmental disturbances such as mechanical vibrations, air flows and temperature drifts, the laser and EC components were rigidly mounted on a solid 305 mm × 710 mm × 76mm slab of aluminum. Then the entire assembly was put into a box made from 51 mm thick Owens-Corning polystyrene foam. These precautions help to stabilize the laser frequency to the order of a few MHz.

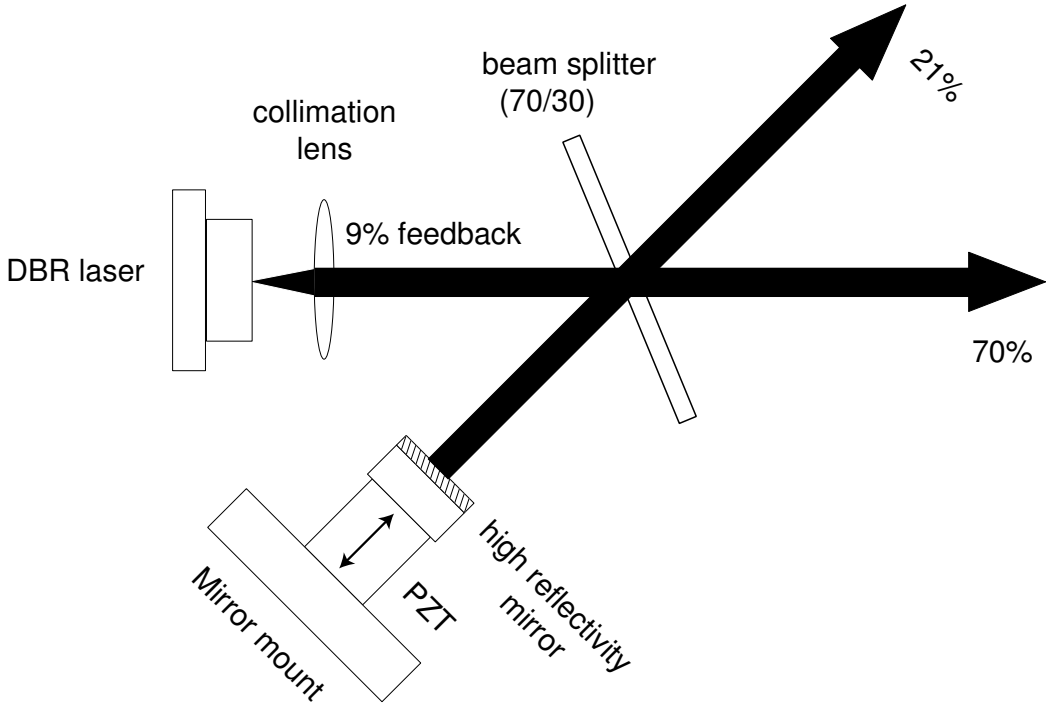

Figure 4.1: The configuration of the extended cavity of the diode laser system. The laser light is collimated and then sent to a 70/30 beamsplitter. The 30% reflected light from the beamsplitter is retroreflected by a high reflectivity mirror ($> 99\%$) to provide 9% optical feedback to the laser. The mirror is mounted on a PZT on a kinematic mirror mount so that the external cavity length is tunable by voltage applied on the PZT. The 70% transmitted light by the beamsplitter is used for the experiment, and the 21% leakage beam is used for saturated absorption spectroscopy.

Aside from providing fine tuning to the laser frequency, the EC configuration also helps to narrow the linewidth of the laser [62, 63]. The linewidth reduction by EC feedback of our DBR laser was measured to be 125 kHz by beating the laser with a second DBR laser (in the same EC configuration). The observed linewidth is 20 times smaller than the 3 MHz free running laser linewidth and also smaller by an order of magnitude than the natural linewidth (1.6 MHz) of the He* transition used in the experiments ($2^3S_1 \rightarrow 2^3P_2$) [52]

4.1.2 Laser Frequency Locking

To further reduce frequency fluctuations and long term drift, a Doppler-free Saturated Absorption Spectroscopy (SAS) signal was used to lock the laser frequency to the desired atomic transition [64]. The leakage beam (21%) light from the EC was used for this purpose while the main beam (70%) was directed to the experiment. In Figure 4.2, the area to the right the dashed line shows schematically how the SAS signal was derived.

The light incident on a thick un-coated glass plate is reflected ($\sim 4\%$) from each surface of the plate, producing two weak parallel beams, termed "probe" and "reference". The two beams pass through a He discharge cell and a 50/50 beamsplitter onto two photodiodes. The absorption signal is then detected as the light frequency is swept across the resonance. The strong transmitted beam, called the "pump", is reflected from the 50/50 beamsplitter to counter-propagate against the probe through the cell. The absorption signal of the reference beam is the usual Doppler broadened peak. However, the probe absorption peak is diminished at resonance since the strong pump beam (with

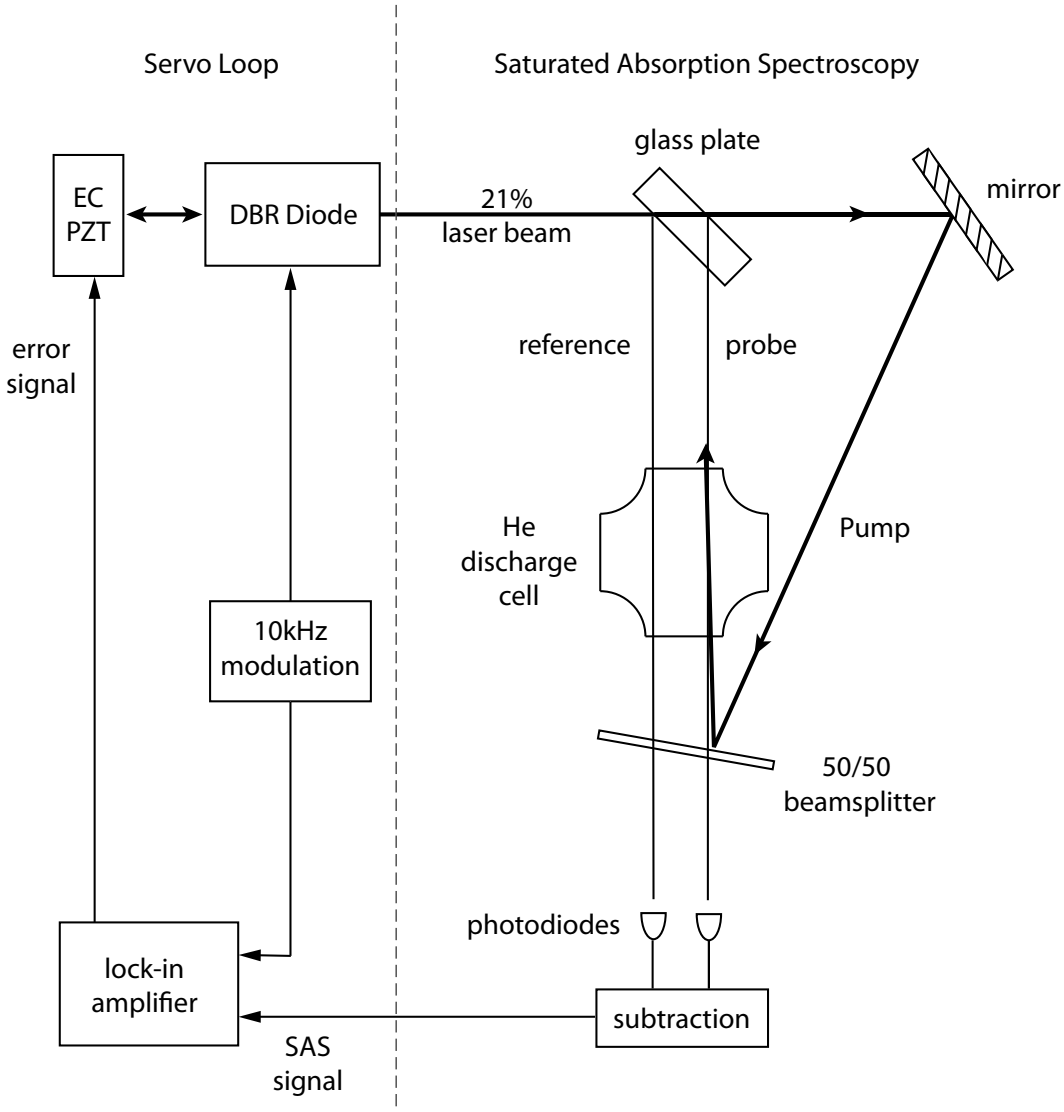

Figure 4.2: The frequency is locked to the $2^3S_1 \rightarrow 2^3P_2$ transition of He* by Saturated Absorption Spectroscopy. The right side of the dashed line shows how the SAS signal is derived from the 21% leakage beam of the laser. The left side shows how the SAS signal is used to produce electronic feedback for laser frequency stabilization.

opposite Doppler detunings) interacts with atoms of the same velocity group and saturates the transition. The resulting signal is the Doppler-free Lamb dip. The subtraction of the absorption signal of the probe from that of the reference will single out the Doppler-free absorption signal for laser frequency locking.

In order to lock the laser, the SAS signal is sent to a lock-in amplifier (Princeton Advanced Research model 126) that generates an error signal to feed back to the laser. A 10 kHz sinusoidal signal produced by an internal oscillator of the lock-in amplifier is applied to the modulation input of laser current controller and also used as a reference signal for the lock-in itself. The modulated SAS signal is mixed with the reference signal in the lock-in amplifier resulting in a derivative of the SAS peak which serves as the error signal. Finally when the PZT scanning is turned off and the laser frequency is set at the resonance peak, the error signal is fed back to the EC PZT to compensate for any drift away from resonance. A schematic of this servo loop is shown in Figure 4.2.

4.2 Electro-optic Modulators

Two $LiNbO_3$-based integrated-optic modulators are used in our experiment. These modulators make use of the linear electro-optic effect in a $LiNbO_3$ crystal which creates a change in the indices of refraction of the crystal proportional to the magnitude of an external applied field [65]. Both modulators

are made by Photline Technologies[1]. The NIR-MPX-LN03 is used for phase modulation and the NIR-MX-LN03 for amplitude modulation. The series of NIR-LN $LiNbO_3$ modulators are designed for near infrared wavelength.

The electro-optic effect in a crystal can be fully described by a third-rank tensor [66]. However, if the electric field is applied on one of the principle axes of the crystal, and the polarization axis of the light is properly chosen according to the crystal symmetry, the complexity can be greatly reduced. $LiNbO_3$ is an anisotropic, uniaxial crystal with good optical and electrical properties. To take advantage of its strongest electro-optic coefficient (r_{33} in the Z direction), the applied electric field as well as the polarization of the light should be aligned with the Z axis. Light travelling perpendicular to the electric field experiences an optical path length change due to the change of the index of refraction that is proportional to the applied electric field and thus accumulates an additional phase shift along its path.

Since the electro-optic coefficients are in general very small ($r_{33} = 32$ pm/V for $LiNbO_3$), a large electric field is required to produce a moderate phase shift. This creates practical difficulties in bulk modulators due to the significant drive voltage required. However, in a waveguide-type integrated-optic modulator, a big electric field is achievable with a much lower drive voltage since the optical field and electric field are localized in a much smaller region of the modulator.

The Photline NIR-LN series modulators use X-cut Y-propagation $LiNbO_3$ crystals. Figure 4.3 shows the geometric configuration of a X-cut $LiNbO_3$

[1] Photline Technologies 16, route de Gray - Bâtiment DF - BP 71025, F-25001 Besançon Cedex 3 - FRANCE. Phone: (33)-0381666622. http://www.photline.com

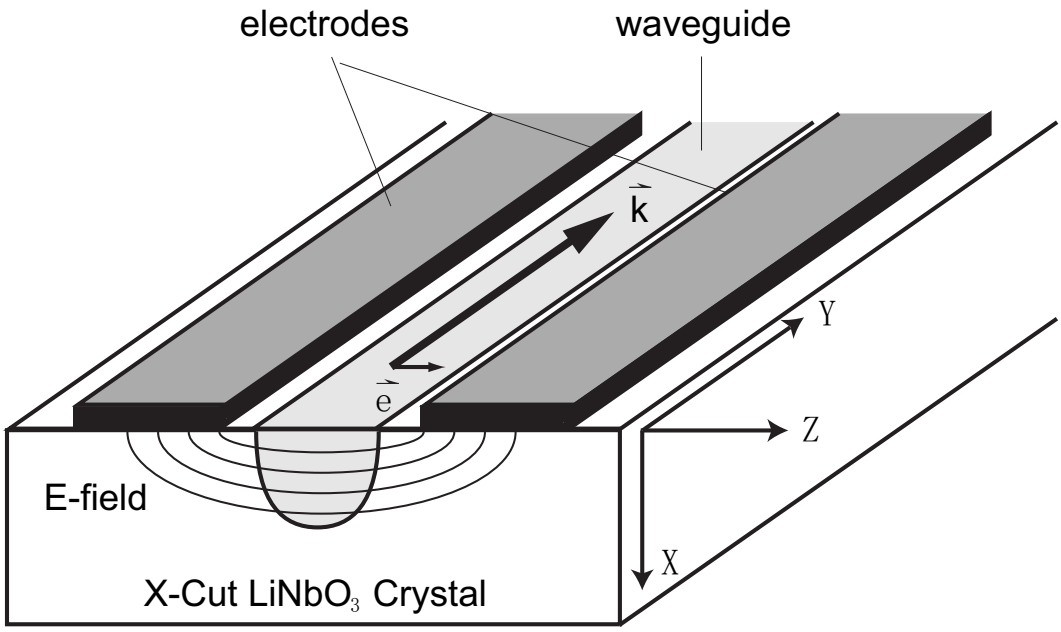

Figure 4.3: The schematic shows a X-cut $LiNbO_3$ crystal being used to construct a electro-optical modulator chip. The principle axes of the crystal are shown in the right corner of the crystal. The electrodes and waveguide are along the Y axis and the electric field in the waveguide is along the Z axis. $\vec{k}$ and $\vec{e}$ represent the light propagation direction and the polarization axis in the crystal, respectively.

crystal being used in a phase modulator. The electrodes are manufactured along the Y axis on the Y-Z plane and the optical waveguide is fabricated between the two electrodes which apply the electric field along the Z axis. The light is also polarized along the Z axis. It enters the waveguide from the X-Z plane and travels along the Y axis. The waveguides in these Photline modulators are fabricated using proton exchange technology in which Li+ ions in the $LiNbO_3$ crystal are exchanged with protons by placing the patterned crystal in a proton-rich acid bath. This results in a permanent increase in the index of refraction of the extraordinary light in the patterned region that guides the light in both width (Z) and depth (X). Cr-Au travelling wave electrodes are deposited over a thick dielectric buffer layer to minimize undesirable optical absorption and satisfy the microwave to optical phase matching condition. The modulator chips are hermetically sealed in 100 mm $\times$ 15 mm $\times$ 9mm metal cases. To ensure that the polarization of the input light is properly aligned with the electric field, a polarization-maintaining (PM) fiber is attached to the input face of the Modulator chip. The output fiber can be either PM or SM (single mode). The fiber pigtails are connected with standard FC/APC connectors with 8° angled ferrules for reducing reflection back into the fibers.

4.2.1 Phase Modulator

The phase modulator works as follows. Apply a sinusoidal radio-frequency (RF) signal with amplitude V and frequency ω_m to the two parallel electrodes of the modulator (see Figure 4.4 (a)), where it can be shown that the total phase delay introduced to the light travelling along the waveguide with

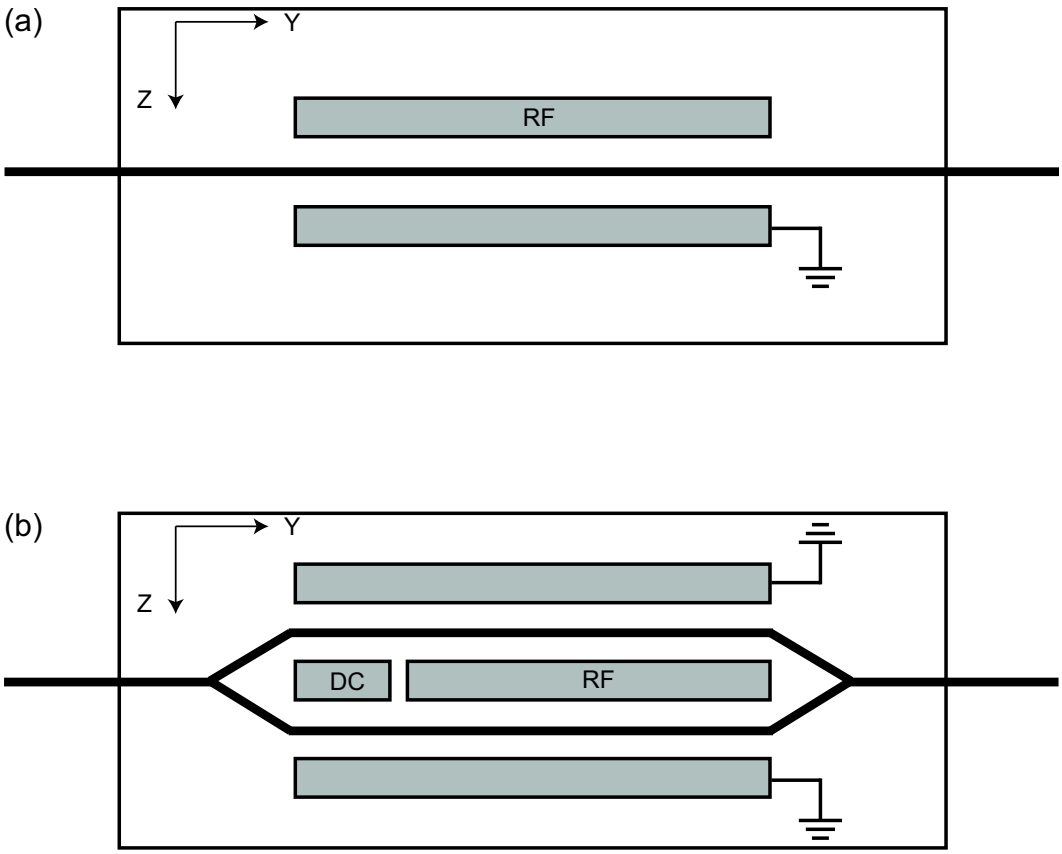

Figure 4.4: Schematic layouts of phase modulator and amplitude modulator on X-cut $LiNbO_3$ crystals. The principle axes of the crystal are shown in the corner of the graph. (a) The phase modulator; (b) The amplitude modulator. Note that the actual electrode layout may be slightly different, but the principle is the same

wavelength λ and polarization along the Z-axis (extraordinary light) is given by

$$\phi(t) = \kappa M(\omega_m)V(t) = \kappa M(\omega_m)V\sin(\omega_m t), \tag{4.1}$$

with

$$\kappa = \frac{\pi}{\lambda G} n_e^3 r_{33} \eta L,$$

where G and L represent the gap and the length of the electrodes. r_{33} denotes the electro-optic coefficient and n_e is the index of refraction for the extraordinary light. The frequency dependence of the phase delay, resulting from RF losses and RF to optical phase mismatch, is defined by the dimensionless parameter $M(\omega_m)$. The overlap coefficient between the electric field and the optical field is indicated by the dimensionless η (see the Photline webpage).

A characteristic quantity of a phase modulator is the half-wave voltage V_π, the voltage required to produce a π phase shift. V_π is also frequency dependent. The effective half-wave voltage at a given frequency can be obtained from

$$V_\pi(\omega_m) = \frac{\lambda G}{n_e^3 r_{33} \eta L M(\omega_m)},$$

At DC $M = 1$, so the expression becomes

$$V_\pi = \frac{\lambda G}{n_e^3 r_{33} \eta L}.$$

With a fixed sinusoidal RF modulation signal, the phase modulated op-

tical field can be expressed as

$$E(t) = E_0 \cos[\omega_l t - \beta \sin(\omega_m t)], \tag{4.2}$$

where E_0 is the amplitude of the light field and ω_l is the angular frequency of the unmodulated light field. β is termed as the modulation index and is defined as below:

$$\beta = \kappa M(\omega_m) V = \frac{\pi}{\lambda G} n_e^3 r_{33} \eta L M(\omega_m) V = \frac{\pi V}{V_\pi(\omega_m)}. \tag{4.3}$$

Determining $V_\pi(\omega_m)$ for a phase modulator is not a simple task. One way to measure $V_\pi(\omega_m)$ is to calculate the modulation index from the measured Fourier spectrum of the phase modulated optical field with a sinusoidal modulation voltage applied. We will describe this in detail in the next chapter.

Phase modulation is equivalent to frequency modulation in the sense that the instantaneous angular frequency of a light signal is the time derivative of the overall phase. Therefore, the instantaneous angular frequency for a phase-modulated light signal is

$$\omega(t) \equiv \frac{d\Phi(t)}{dt} = \omega_l - \beta \omega_m \cos(\omega_m t). \tag{4.4}$$

Sinusoidal phase modulation thus results in sinusoidal frequency modulation at the same frequency ω_m, but with a 90° phase lag.

4.2.2 Amplitude Modulator

Compared to the phase modulator, the amplitude modulator works in a more complicated way. It is constructed by patterning a Mach-Zehnder interferometer ([64]) onto a $LiNbO_3$ substrate (see Figure 4.4 (b)). Instead of a single light path as in the phase modulator, the input optical waveguide is split into two paths and then recombined at the output end. Three parallel electrodes are deposited on the substrate to sandwich the two waveguides. The central electrode is divided into two sections in order to apply a DC bias and RF signal separately. The two side electrodes are grounded. A voltage applied to the center electrode results in opposite electric fields across the two paths of the interferometer and thus a change in the index of refraction in opposite directions. The induced optical phase shift increases in one path and decreases in the other path. The light going through the two paths combines coherently at the output. A $2n\pi$ net phase difference between the two paths leads to constructive interference while a $(2n+1)\pi$ net phase difference leads to destructive interference.

The output electric field can be generally described as

$$E(t) = \frac{E_0}{2}[\cos(\omega_l t + \phi(t)) + \cos(\omega_l t - \phi(t))] = E_0 \cos\phi(t) \cos\omega_l t, \qquad (4.5)$$

where $\phi(t)$ represents the phase shift induced on one arm of the Mach-Zehnder interferometer that is proportional to the applied voltage as in the phase modulator. Note that the phase shift on the other arm has an opposite sign, the total phase difference is then given by $2\phi(t)$. If a DC voltage is applied

to the electrodes, the output field has a constant amplitude $E_0 \cos\phi$ since ϕ is a constant. On the other hand, if an RF signal is applied to the electrodes, the output optical field has an amplitude envelope of $E_0 \cos\phi(t)$ and it is obvious that it is amplitude modulated with the modulation frequency equal to the RF frequency.

Theoretically, the optical power output of the amplitude modulator is given by

$$P_{out} = \frac{P_0}{2}[1 + \cos 2\phi(t)], \tag{4.6}$$

where P_0 is the maximum output power. The theoretical output power verses the phase shift on one arm is plotted in Figure 4.5.

Since a Mach-Zehnder amplitude modulator is an interferometric device exhibiting a sine transfer function, it is very sensitive to variations in the operating conditions. Having the DC electrodes separated from the RF electrodes allows us to adjust the operating point of the Mach-Zehnder modulator independently from the high frequency modulation signal applied. Depending on the specific application, the desired operating point can be set by a fixed voltage applied to the DC bias electrodes. The modulators are often biased at a half-power point (QUAD+ or QUAD-) of its transfer function for linear operation, e.g. for applications such as analog or digital transmissions. However, for pulse generation, as in our case, the modulator should be biased at an extreme points (MIN or MAX) of its transfer function. The minimum power point is more favorable in operation due to its stability. Since a quarter-wave voltage is enough to bring the output optical power from minimum to maximum, the RF amplitude should be limited to half $V_\pi(\omega_m)$ at the given frequency ω_m. Here

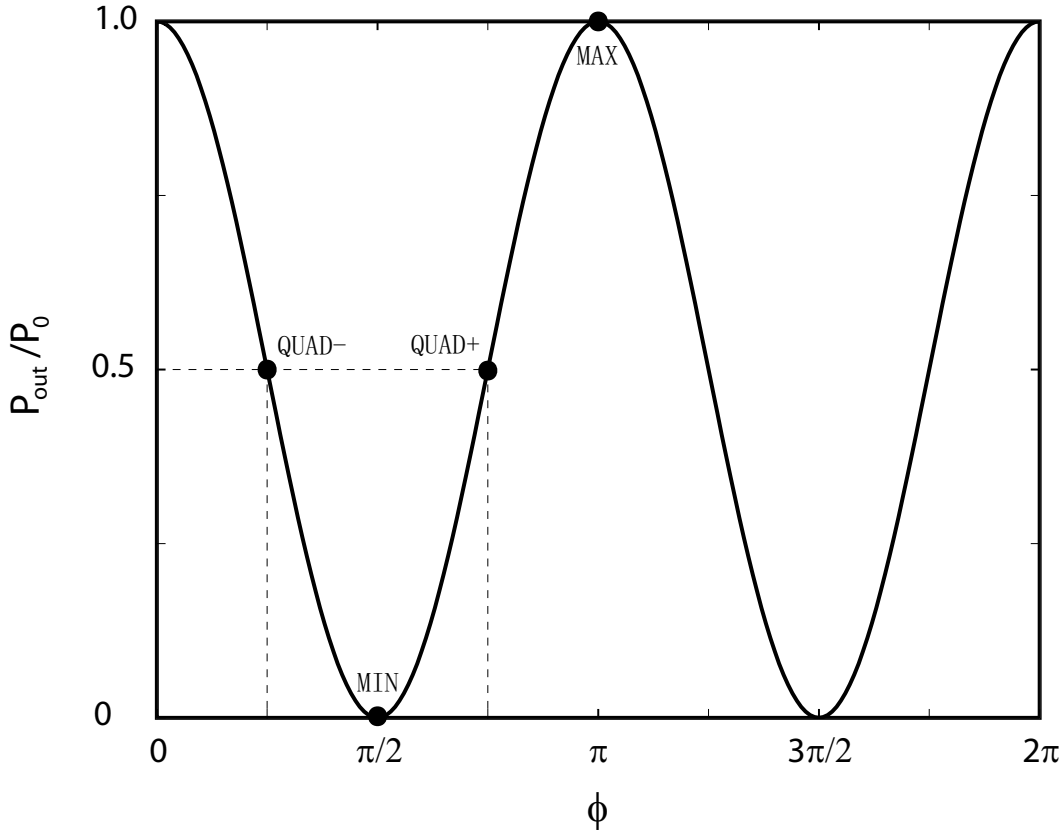

Figure 4.5: Plot of output optical power versus the phase shift on one arm of the Mach-Zehnder amplitude modulators. The phase shift on the other arm has the same magnitude but an opposite sign due to the symmetric electrodes layout, so the total phase shift is double. The operating points can be set to the extreme points (MIN or MAX) or the quadrature points (QUAD+ or QUAD-) of the plot depending on the specific application

V_π is the voltage which produce π phase shift on one arm of the Mach-Zehnder amplitude modulator. It is different from the manufacture's value by a factor of 2 since they refer the total phase difference of the two arms.

4.2.3 Chirped Pulse Production

In the ARP experiment, each adiabatic rapid passage is induced by a chirped pulse. Multiple repetition of ARP sweeps with chirped pulses from counter-propagating light beams enables the huge force used for pushing the atoms. The first step of the experiment is to produce the periodic chirped pulses.

Periodic chirps are easily produced with the NIR-MPX-LN03 phase modulator. The optical field, phase modulated with a sinusoidal RF signal is described in Eq. (4.2) and the instantaneous frequency is given by Eq. (4.4). If the frequency of the laser is set at the resonance frequency, i.e. $\omega_l = \omega_a$, the instantaneous frequency of the modulated light chirps from $\omega_a - \beta\omega_m$ to $\omega_a + \beta\omega_m$ at each first-half period and chirps back at each second-half period. This automatically generates the desired periodic frequency chirp.

In practice, the 160 MHz RF drive signal of the phase modulator originated from a HP8657D signal generator that was amplified by a Mini-Circuits ZHL-5W-1 high power amplifier. The amplifier has a fixed gain of 45 dB when powered with a 24 Volts DC from a Power Design Inc. model 6105 universal power supply. The output power level is determined by the RF input power from the HP8657D. The maximum power output of the amplifier (37 dBm) is higher than the maximum allowable input power (34 dBm) of the phase

modulator. Therefore, extra caution must be taken in varying the power level in the HP8657D, so no more than -11 dBm (which is 63 mV RMS for a sine wave) should be delivered by the HP8657D to avoid overloading the phase modulator RF termination.

Periodic pulses are accomplished with the NIR-MX-LN03 amplitude modulator. A pulse generator is required for this purpose. The amplitude modulator bias voltage is provided by a Power Design Inc. model 2005 precision power supply. A HP8082A pulse generator triggered by a HP8657A signal generator is used to drive the amplitude modulator at a trigger frequency of 80 MHz. The 8082A operates at approximately 25% duty cycle at this frequency with its shortest pulse output $\sim$ 3 ns. The purpose of the 75% dark time is going be more evident in Section 4.5. The electrical pulse has a triangular-like shape when operating at the minimum pulse width. The output voltage is $\sim$ 4 V which is about half V_π. The RF pulses are then applied to the modulator. The pulse generator has a complementary output which is used as a monitor signal. The output light signal from the amplitude modulator was measured by a Thorlabs D400FC Fiber optic detector. The D400FC has a 100 ps rise time which is short enough to accurately measure the nanosecond optical pulse. The measured amplitude envelope as well as the electronic monitor signal are displayed on and saved by a Lecroy WS434 digital oscilloscope. The captured electric and optical pulse profiles are shown in Figure 4.6. However, the pulse profiles, especially the optical pulse profile, exhibit some electronic noise which makes the pulse length measurement inaccurate.

To produce chirped pulses, we need to synchronize the frequency chirp-

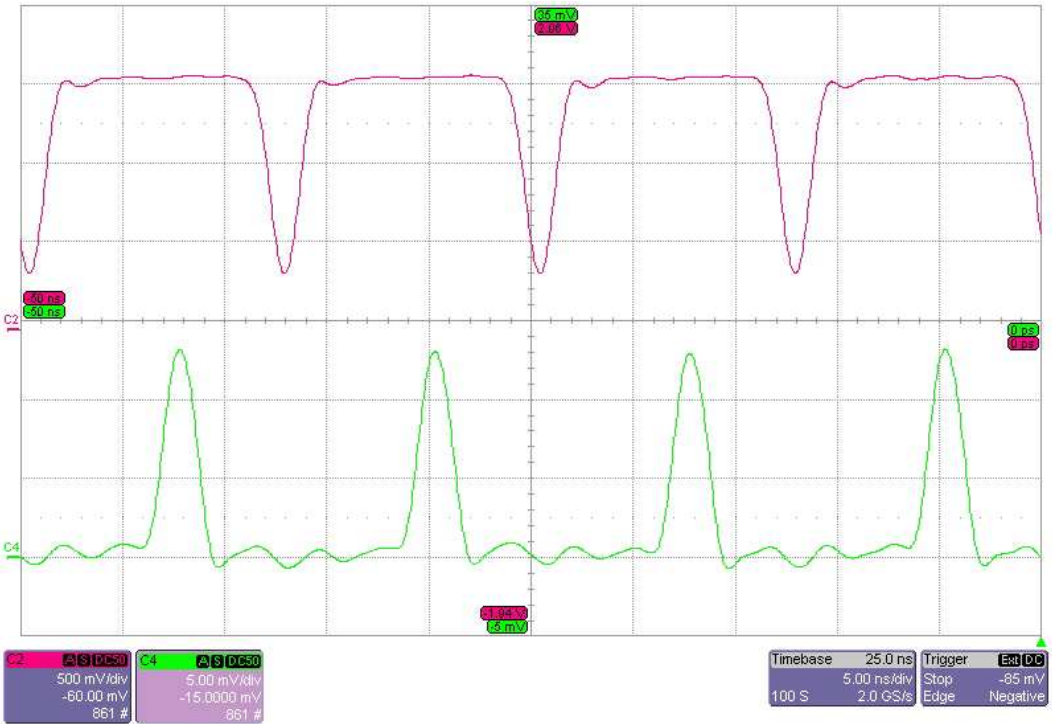

Figure 4.6: Oscilloscope image of the periodic optical pulse delivered by the NIR-MX-LNO3 amplitude modulator (lower trace) as well as the complement of the RF drive signal (upper trace). Both signals have a frequency of 80 MHz and a pulse of width about 3.5 ns (measured from the baseline). The optical signal shows some ringing at the base which might be induced by the after-pulse tail of the electric signal together with some RF reflection.

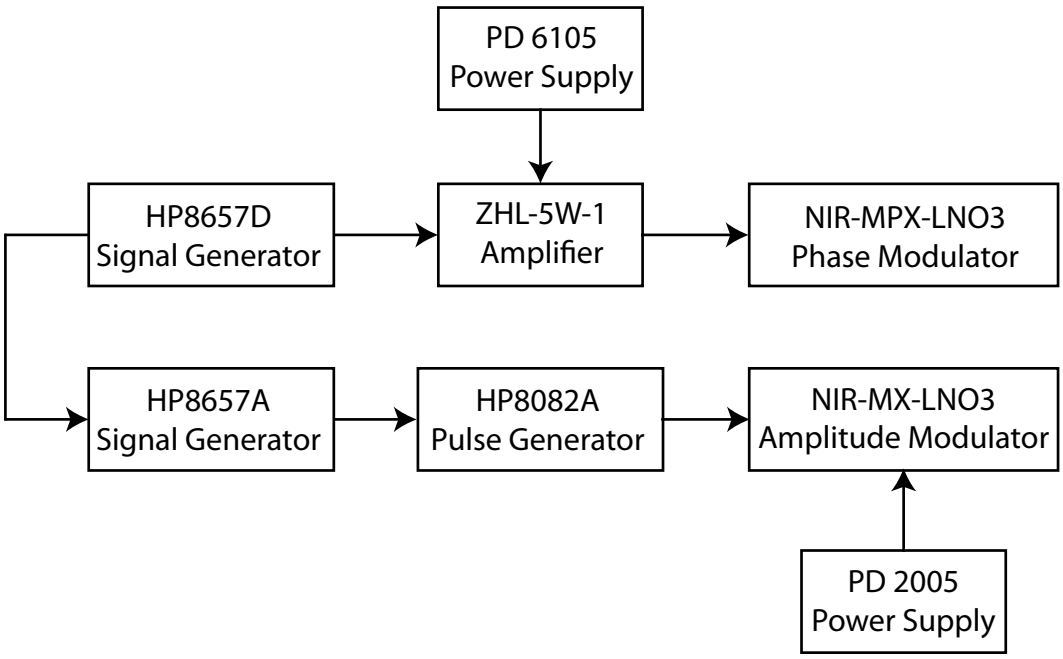

Figure 4.7: The RF signal used to drive the NIR-MPX-LN03 phase modulator originated from a HP8657D signal generator and was then amplified by a Mini-circuit ZHL-5W-1 amplifier which was powered by PD 6105 power supply. A HP8082A pulse signal generator triggered by a HP8657A signal generator was used to drive NIR-MX-LN03 amplitude modulator. The DC bias voltage of NIR-MX-LN03 was supplied by a PD 2005 power supply. Synchronized driving was achieved by synchronizing the HP8657D and HP8657A

ing and amplitude pulsing. The problem can be solved by synchronizing the HP8657D and HP8657A. More specifically, a high precision timebase output from the HP8657D was used to drive both the HP8657D and HP8657A. The relative phase between the phase modulator drive signal and the amplitude modulator drive signal can be coarsely adjusted by the delay knob in the pulse generator and be fine adjusted by the phase control button of the HP8657D signal generator. A block diagram of the electronics used for chirped pulse production is shown in Figure 4.7.

4.3 Fabry-Perot spectrometer

In the ARP experiment, the monochromatic laser output was first sinusoidally phase modulated and then amplitude modulated with a periodic pulse signal, so that the resulting light field was not simple. To characterize the modulated light field, an optical spectrometer is needed. We designed and built two Fabry-Perot (FP) spectrometers for the purpose of spectrum analysis. Though commercial ones with better performance are also available, they may cost several thousand dollars.

A FP spectrometer is basically a scanning FP interferometer whose principles are described in detail in [64, 10]. Another useful reference on FP spectrometer is [67]. A couple of things need to be taken into consideration in designing a FP spectrometer for our experiment. First, the FP needs to be able to to measure a strongly frequency modulated signal. The modulation frequency is around $100-200$ MHz, and the modulation index can be larger than a few π, so the free spectral range (FSR) of the FP needs to be a few

GHz. However, a large FSR means a short cavity which causes some practical difficulties in the construction. Moreover, we need to be able to distinguish the neighboring peaks separated by the modulation frequency, therefore the width of the FP transmission needs to be lower than the modulation frequency, which demands a high finesse for a FP with a large FSR. With all these restrictions taken into consideration, a FSR = 3 GHz was chosen for our experiment. The FP spectrometer was in the usual confocal configuration [64]. The cavity length can be calculated from FSR $= c/4l$ to be $l = 25$ mm. The cavity mirrors are partial reflectors from CVI laser. They have a flat surface antireflection coated for 1083 nm and a curved surface with 98.7% reflectivity. The mirrors are 0.5 inch in diameter, 0.375 inch in thickness and with 25 mm focal length. The cavity length is also 25 mm. The PZT cube from is 0.5 inch O.D. $\times$ .44 inch I.D. $\times$ 0.5 inch length. Considering the short length of the cavity, the body of the FP was built into two parts. The exact design is shown in Figure 4.8.

The body is made from invar for its low thermal expansion coefficient. It consists of two parts, a tube and a cap. A mirror was epoxied on one side of the tube. A PZT and a mirror were epoxied on the cap and the whole piece was then inserted in the other side of the tube. The two parts were mounted together by three screws with a rubber O-ring inserted in between. The length and the alignment of the FP cavity are adjustable by turning the three screws to squeeze the O-ring. Another smaller O-ring was put on the inserted mirror for support. Electric wires were attached to the inner and the outer surface of the PZT. Grooves in the FP body were designed for

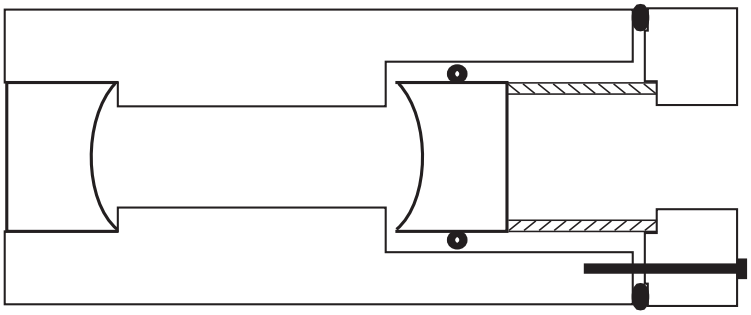

Fabry-Perot Spectrometer

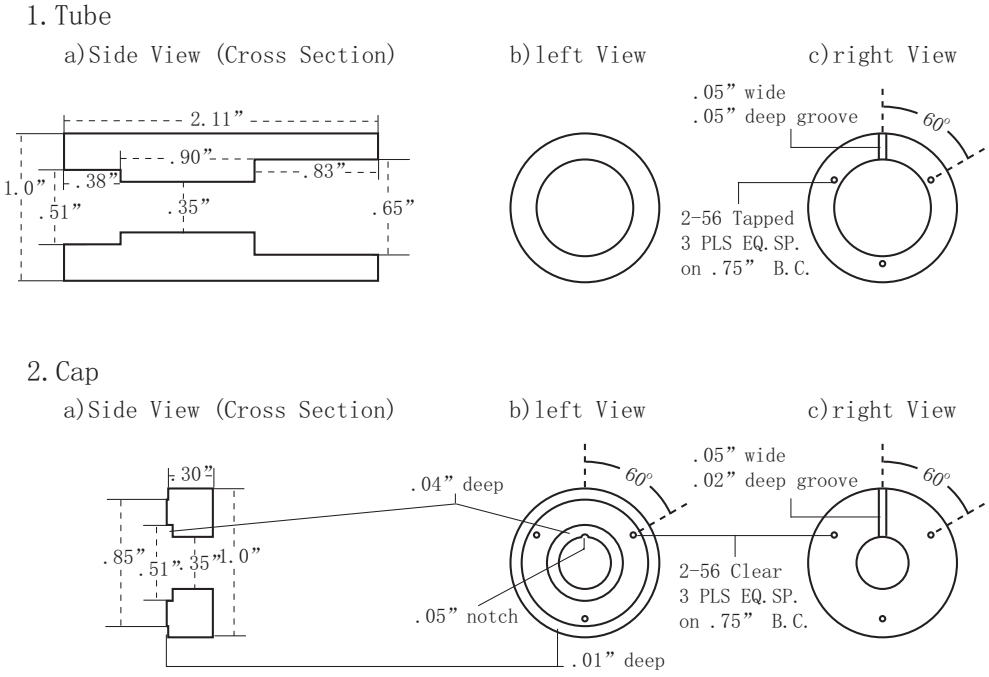

Figure 4.8: The construction of the Fabry-Perot spectrometer. The cross section of the assembled FP spectrometer is shown on the top of the plot. The detailed dimension of the FP body is shown on the lower part. The body is made from invar for its low thermal stability. It is made up of two parts with a mirror attached on one part and a mirror and a PZT on the other. The two parts are then mounted together with three screws. The length of the FP cavity is adjustable with a rubber O-ring inserted between the two parts.

the wires to go through. By applying a voltage to the PZT with a home-made PZT controller, the cavity length and thus the resonance frequency of the FP interferometer is tunable. A photo detector (Thorlabs 110) was put behind the FP to measure the transmitted optical power. In this way, the scanning Fabry-Perot interferometer acts as an optical spectrum analyzer. A frequency spectrum of the input signal is produced when the voltage on the PZT is ramped. We built two Fabry-Perot spectrometers of the same design. A Finesse of 60 can be obtained for both of them with careful alignment and a $f = 500$ mm lens for mode matching.

4.4 Fiber Optic Amplifiers

The EC diode laser has a linearly polarized output of around 20 mW in the main beam in normal operating conditions. Each modulator has $\sim$4 dB insertion loss, which amounts to about 60% loss for each. At 25% duty cycle pulse operation for the amplitude modulator, at least another 75% optical power loss is expected. With the additional fiber coupling loss of the free space laser output to the modulator, and fiber to fiber coupling loss, the optical power is easily dropped to less than 0.1 mW which is too low to do the experiment. For the atomic state to adiabatically follow the optical field in an ARP process, a high peak Rabi Frequency ($\Omega \gg \omega_m$) is required. Furthermore, to map the ARP force in parameter space, we need to scan along the axis of Rabi Frequency, so a lot more optical power is demanded in the experiment. To resolve the power issue, two optical fiber amplifiers are utilized for the experiment.

Fiber optic amplifiers are widely used in the telecommunications industry for signal amplification in long-haul lightwave systems [68]. However, the wavelength used in telecommunication systems is 1.55 μm where erbium-doped fibers provide the gain media. For the 1083 nm wavelength in He*, Ytterbium(Yb)-doped fibers are used as the gain media. The Yb-Doped fiber amplifiers (YDFA) we used are manufactured by Keopsys[2]. Yb ions doped in the fiber core result in a broad absorption spectrum peaked at 977 nm, where high-power, broadstrip diode lasers are commercially available. When pumped at this wavelength, a population inversion is achieved in the fiber and provides amplification of the input signal at wavelength 1083 nm by stimulated emission. The Yb-doped fiber has a double cladding. The pump light is injected from a V-groove mechanically formed in the outer cladding and propagates in the inner cladding to provide amplification along the input light path in the fiber core [69]. Both the input and output fibers of the YDFA are Single Mode (SM) for 1083 nm and are connected with FC/APC connectors. FC/APC to FC/APC mating sleeves are used to couple the fiber modulators to the fiber amplifiers directly with a coupling efficiency of $\sim 80\%$.

YDFA is suitable for ultrashort pulse amplification thanks to its broadband, long tail emission spectrum from 1060 nm to 1200 nm [70, 69]. A model KPS-BT2-YFA YDFA was used to boost the power of the chirped pulses to the required level for the experiment. The KPS-BT2-YFA has two gain stages with an optical isolator in front of each amplification stage to prevent any

[2] Keopsys SA. 21, rue Louis de Broglie 22300 Lannion FRANCE. (33)-296050800. http://www.keopsys.com/

high power optical feedback. The first stage is a saturated amplification stage which provides a constant output of ∼190 mW. The second stage is pumped by two diode lasers whose current can be turned on successively. The gain of the amplifier is proportional to the injection current of the laser diodes with a slope of ∼ 590 mW/A. Setting the first diode current to its maximum of 5 A yields 3 W output. Further amplification can be obtain by adding current to the second laser diode. The maximum output power of the amplifier is 4.3 W [53]. The power output level was measured to be the same for CW operation and the pulse operation in our experiment.

The YDFA demands a certain minimum input signal power to operate preoperly. When the input signal is too low to deplete the population inversion of the doped Yb ions, Amplified Spontaneous emission (ASE) and self lasing can occur in the YDFA which can lead to a breakdown of the internal isolator and possible damage of other optical element in the optical train [68].

A minimum input power of 0.5 mW is required for the KPS-BT2-YFA. However, the optical power level after two modulation steps is too low to meet this requirement. For this reason, a 1 W YDFA (model OIYb30) was inserted between the phase modulator and the amplitude modulator as a preamplifier. But with this older fiber amplifier, ASE and self lasing were often problems since there is no internal isolator in the system. To protect the diode laser from possible damage due to ASE light, a OFR model IO-3-1083-HP Faraday isolator was placed after the DBR laser. This isolator allows ∼90% transmission in the forward direction and provides an isolation of ∼40 dB in the reverse direction. The free space light which passed through the isolator was

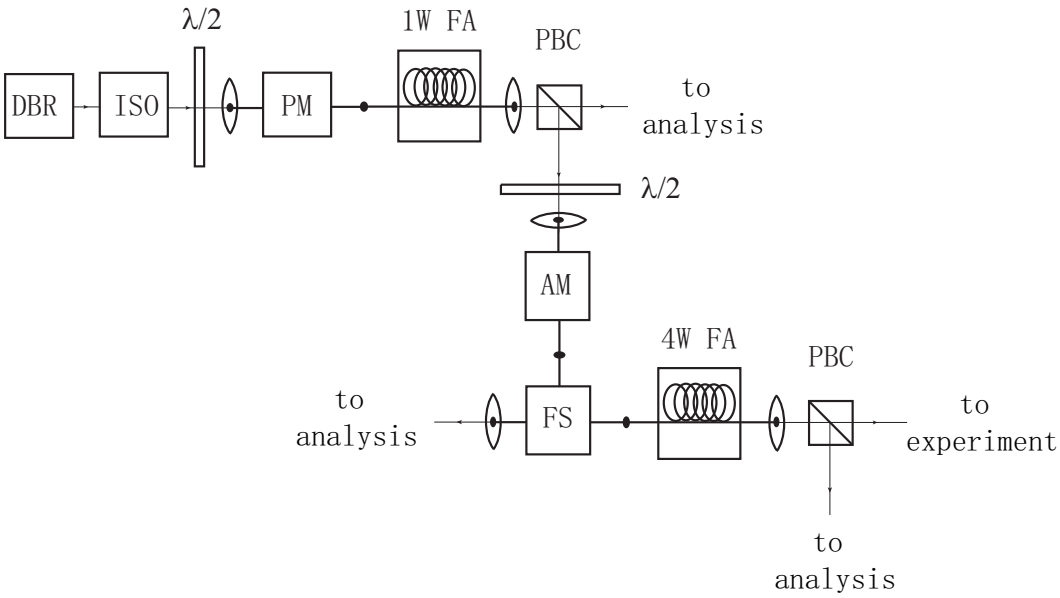

Figure 4.9: The optical system for the chirped pulses production and amplification. The DBR laser output goes thought an isolator and then into the phase modulator. The output of the phase modulator is preamplified by a 1 W YDFA and then sent to the amplitude modulator. The resulting chirped pulses pass through a fiber splitter to the 4 W YDFA to boost the power to the level required for the experiment. The light was split after the 1 W YDFA, the fiber splitter, and the 4 W for spectrum analysis.

then coupled into the input fiber of the NIR-MPX-LNO3 phase modulator by an OFR PAF-X-7-1083 fiber coupler. Since the input fiber of the phase modulator is a polarization maintaining fiber, a $\lambda/2$ plate is needed to get the correct linear polarization input at the input.

The output of the phase modulator was coupled to the input fiber of the 1 W YDFA by a standard FC/APC to FC/APC mating sleeve. The 1 W YDFA had been used in experiments for 5 years before being used in our experiment, both the input and output fiber connectors had been damaged

and reconnectorizd. Although the lab owns the tools for fiber connection and polishing, it is still very difficult to produce the high quality of fiber termination needed for high power operation. The reconnected fiber is easily damaged under high power operation. We experienced ASE and self lasing which not only damaged the input fiber connector of the fiber amplifier but also damaged the output fiber connector of the phase modulator. Later, additional precautions were taken by inserting a short SM patchcord in between the phase modulator and 1 W YDFA, which we expected would serve as an optical fuse. Extreme care was also taken in slowly turning up the gain of the 1 W YDFA. Fortunately, a low current setting of < 0.8 A (with 76 mW output power) is satisfactory in the experiment if we have good fiber coupling in the later stages of the optical system.

The output of the 1 W YDFA was collimated by a ThorLabs F220FC-C fiber coupler and was sent through a polarization splitting cube (PBC) to split off a small portion for analysis. Since physical stresses can induce birefringence in an optical fiber [71], the polarization of the input signal is changed when it is going through a SM fiber. To set the polarization of the output light, both input and output fibers were coiled, bent, and secured to maximize the desired polarization component going to the next step of the experiment. Another $\lambda/2$ plate and a OFR PAF-X-7-1083 fiber coupler were used to coupled the light into the NIR-MX-LNO3 amplitude modulator. A 90/10 fiber splitter for 1083 nm was connected afterwards with the 90% output coupled to the input of the 4 W YDFA and the 10% output used for analysis. Finally, the amplified output of the 4 W YDFA was again collimated and split by a PBC to direct the main

laser beam toward the atomic beam and the split beam for analysis. Similarly, fibers were coiled, bent, and secured to maximize the desired polarization component for the experiment. Fine-tuning of the polarization of the 4 W YDFA was also feasible by a build-in polarization control element in the fiber amplifier that precisely squeezed and twisted a small section of the output fiber to get the polarization right. The schematic optical setup for producing the amplified chirped pulses for the experiment is shown in Figure 4.9

4.5 Interaction Regions

Before being sent to the interaction region, the amplified chirped pulses were further collimated and expanded with a spherical telescope and a cylindrical telescope to make an elongated spatial profile. The purpose of expanding the beam is to produce a flat spatial intensity profile in the interaction region. Another $\lambda/2$ plate and a PBC are inserted between the two telescopes to vary the intensity of the light that goes into the interaction region. The spatial profile of the ARP beam was measured by a ~ 100 μm scanning slit. The resulting beam has a Gaussian profile with waists of $w_{long} = 7.0$ mm and $w_{short} = 2.1$ mm, where w is the $1/e^2$ radius of the Gaussian Intensity fit. The major axis of the light was oriented to be along the propagation direction of the atomic beam. A variable vertical slit was inserted in the laser beam just before the interaction region to cut off the wings of the beam. The light has a linear polarization perpendicular to its major axis. The beam was then sent through a $\lambda/4$ plate to produce the circular polarized light demanded by the $2^3S_1 \rightarrow 2^3P_2$, $\Delta m_J = +1$ He* transition.

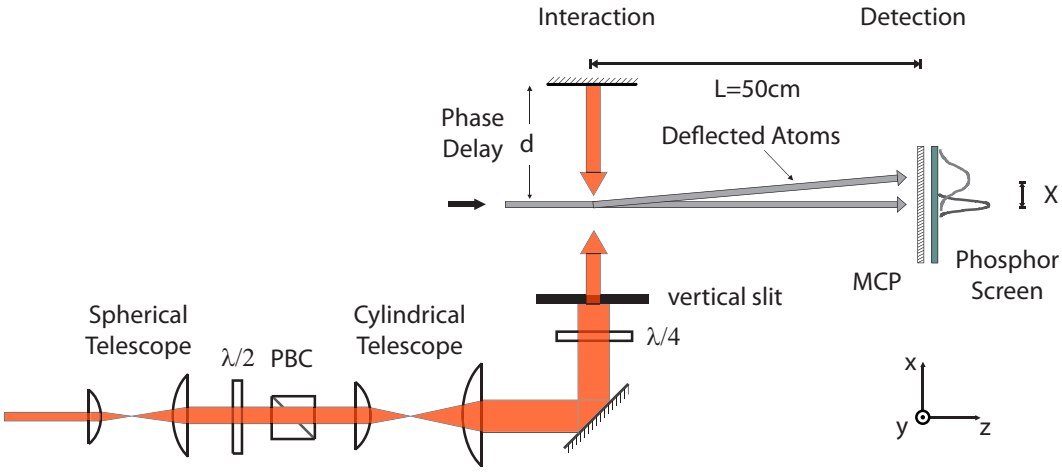

Figure 4.10: The Schematic of the optical setup in the interaction region. The optical beam of the chirped pulses was collimated and expanded with a spherical telescope and a cylindrical telescope. The resulting beam has a Gaussian profile with $w_{long} = 7.0$ mm and $w_{short} = 2.1$ mm. The major axis that was aligned with the atomic beam was further defined with a vertical slit to produce a flat intensity in the interaction region. The light was circularly polarized with a $\lambda/4$ plate. The light is retroreflected with a high reflection mirror to intersect with the atomic beam twice. The delay path was set to provide the necessary $\pi/2$ phase delay to the retroreflected light for the production of the unidirectional force. The deflection of the atomic beam is measured with a MCP/phospher screen detector.

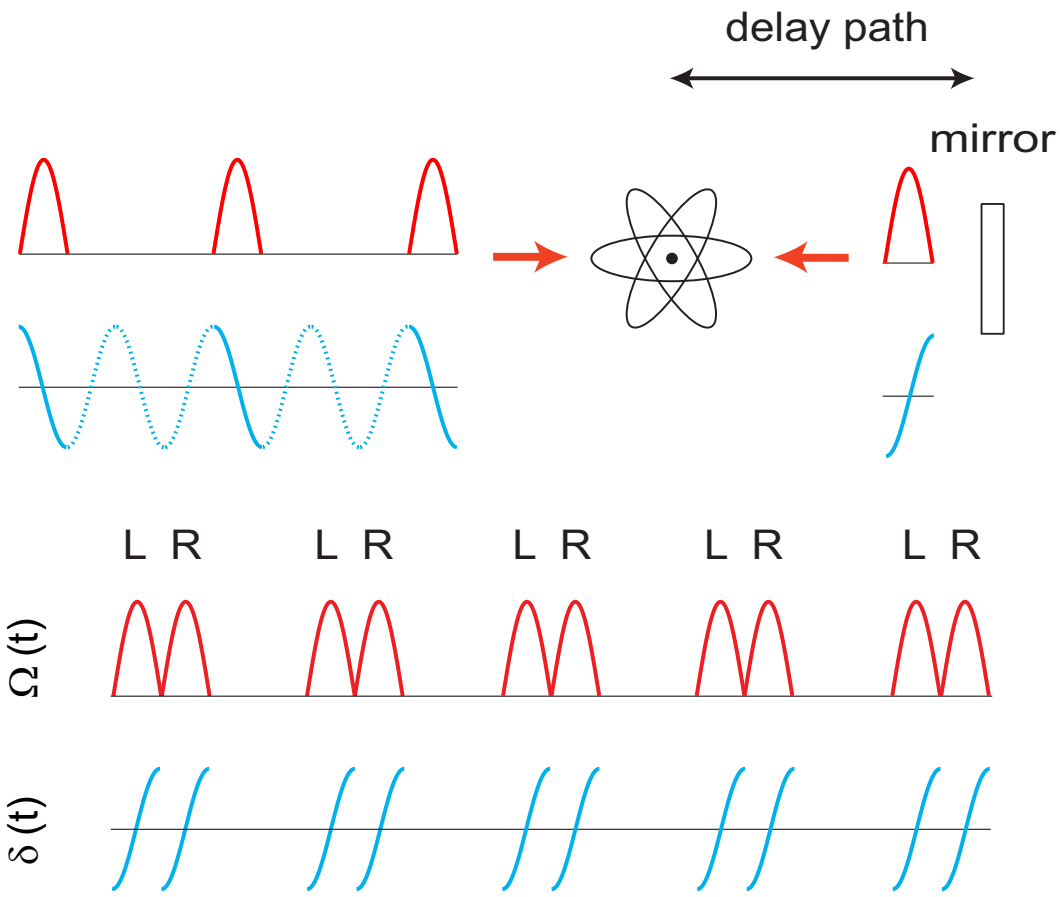

Figure 4.11: The Schematic of the periodic ARP pulse train used for atomic beam deflection. The production of the periodic chirped pulses with 25% duty cycle (right top of the diagram) is as described in Section 4.2.3. The pulses are retroreflected with a high reflection mirror to cross the atomic beam twice. The delay path was set to provide the necessary $\pi/2$ phase delay to the retroreflected light for the production of the unidirectional force. The resulting ARP pulse train is exactly the same as depicted in Figure 2.6(b)

The light is sent across the atomic beam and then retroreflected with a high reflection mirror to cross with the atomic beam again on its way back. The distance between the crossing point and the mirror is chosen to be $\lambda_m/8 = 15/32$ m where λ_m is the wavelength of the amplitude modulated pulse train. The purpose of this is to produce a $\pi/2$ phase delay to the retroreflected light. As illustrated in Figure 4.11, the resulting chirped pulse train at the position of the atomic beam is exactly the same as sketched in Figure 2.6(b). The atomic beam is pushed by the periodic chirped pulse pairs. The $T/2$ dark time in between the pulse pairs on average serves to prepares the He* atom in the ground state by spontaneous emission as we discussed in Section 2.5. Our experimental scheme is very similar to what was proposed in [36] except for the realization of chirped pulse train. The advantage of producing a periodic pulse train in our scheme over using the multiple reflection of a single pulse in a cavity as proposed in [36] is that the pulse amplitude does not decay in time, so that the force is stronger and more stable.

Finally, the deflection of the atomic beam was imaged by a MCP/phospher screen in combination with a CCD camera 50 cm downstream. The force produced by the periodic chirped pulses on the He atoms can be calculated from the deflection distance measured from the image. A schematic drawing of the optical setup in the interaction region is shown in Figure 4.10.

Chapter 5

Spectrum Analysis

In principle a Fabry-Perot spectrometer performs a Fourier transform of the input light field. However, only the amplitude information of each frequency component is captured by the photo detector, the phase information is lost. More accurately, the Fabry-Perot spectrometer gives us $I^F(\omega) = A^F(\omega)^2$, where $I^F(\omega)$ and $A^F(\omega)$ stand for the intensity and the amplitude of the Fourier component at frequency ω. In spite of the loss of phase information of each Fourier component, the phase information of the light field is still partially captured by the Fabry-Perot spectrometer. As we will explain in detail, the Fabry-Perot spectrometer is a powerful and very useful tool in the calibration and control of this experiment.

5.1 Spectrum of Periodically Modulated Light

Mathematically, we know there are three equivalent representations of Fourier expansions of a periodic real function of time. A monochromatic light modulated with periodic signals has the following generic form at a fixed po-

sition,

$$E(t) = A(t)\cos(\omega_l t + \phi_p(t)), \tag{5.1}$$

where ω_l is the light carrier frequency, $A(t)$ and $\phi_p(t)$ are the modulated amplitude and phase respectively. The frequencies of the amplitude modulation and the phase modulation may not necessarily be the same. With the common frequency of the two denoted by ω_c, *e.g.* the common period is $\frac{2\pi}{\omega_c}$, the field in the form of Eq. (5.1) has Fourier component at frequencies $\omega_l \pm n\omega_c$ where n is a integer. Generally its Fourier spectrum can be written in three equivalent forms,

$$\begin{aligned} E(t) &= \sum_{n=-\infty}^{\infty} \{a_n \cos(\omega_l + n\omega_c)t + b_n \sin(\omega_l + n\omega_c)t\}, & (5.2)\\ &= \sum_{n=-\infty}^{\infty} A_n^F \cos[(\omega_l + n\omega_c)t - \varphi_n], & (5.3)\\ &= \sum_{n=-\infty}^{\infty} \{c_n e^{i(\omega_l + n\omega_c)t} + c_n^* e^{-i(\omega_l + n\omega_c)t}\}. & (5.4) \end{aligned}$$

The Fourier expansion coefficients in Eq. (5.2) are given by

$$\begin{aligned} a_n &= \frac{2}{T}\int_0^T dt E(t)\cos(\omega_l + n\omega_c)t,\\ b_n &= \frac{2}{T}\int_0^T dt E(t)\sin(\omega_l + n\omega_c)t, \end{aligned}$$

where $T = 2\pi/\omega_c$. The Fourier expansion coefficients in Eq. (5.4) are given by

$$c_n = \frac{1}{T}\int_0^T dt E(t) e^{-i(\omega_l + n\omega_c)t}. \tag{5.5}$$

Comparing Eqs. (5.2) and (5.3), we have

$$\begin{aligned} A_n^F &= \sqrt{a_n^2 + b_n^2}, \\ \varphi_n &= \arctan \frac{b_n}{a_n}. \end{aligned}$$

Comparing Eqs. (5.2) and (5.4), we have

$$c_n = \frac{1}{2}(a_n - ib_n).$$

It is obvious that $A_n^F = |2c_n|$. The output of a Fabry-Perot spectrometer gives the following spectrum,

$$I_n^F = (A_n^F)^2 = |2c_n|^2. \tag{5.6}$$

Since the expansion Eq. (5.4) has the simplest coefficients given by Eq. (5.5), especially for modulated light that has a complicated form, it is convenient to calculate the spectrum with Eq. (5.5).

$$\begin{aligned} I_n^F = |2c_n|^2 &= |\frac{2}{T}\int_0^T dt E(t) e^{-i(\omega_l + n\omega_c)t}|^2, \\ &= |\frac{2}{T}\int_0^T dt A(t)\cos(\omega_l t + \phi_p(t)) e^{-i(\omega_l + n\omega_c)t}|^2, \\ &= |\frac{1}{T}\int_0^T dt A(t)[e^{i(\omega_l t + \phi_p(t))} + e^{-i(\omega_l t + \phi_p(t))}] e^{-i(\omega_l + n\omega_c)t}|^2, \\ &= |\frac{1}{T}\int_0^T dt A(t) e^{i(\phi_p(t) - n\omega_c t)}|^2 \end{aligned} \tag{5.7}$$

The second term in the integral is high frequency oscillatory term and averages out to zero.

5.2 Phase Modulated Spectrum

The phase modulated light field in the experiment is described in Eq. (4.2) and we repeat it here for convenience,

$$E = E_0 \cos[\omega_l t - \beta \sin \omega_{pm} t] \tag{5.8}$$

ω_{pm} is the phase modulation frequency and β is the modulation index. Comparing with Eq. (5.1), we have

$$\begin{aligned} A(t) &= E_0, \\ \phi_p(t) &= -\beta \sin \omega_{pm} t. \end{aligned}$$

By using the Jacobi-Anger Expansion (see [72]), one can derive the Fourier spectrum of the phase modulated light field. It has the well known spectrum of the Bessel functions as below,

$$E = E_0 \cos[\omega_l t - \beta \sin \omega_{pm} t] \equiv E_0 \sum_{n=-\infty}^{\infty} J_n(\beta) \cos((\omega_l - n\omega_{pm})t), \tag{5.9}$$

where $J_n(\beta)$ is the n'th order Bessel function of the first kind. A plot of Bessel functions J_n (n=0, 1, 2, 3) is shown in Figure 5.1. There are many properties of the Bessel Function J_n, we list two of them that will be used later.

1. The symmetry relation

$$J_{-n}(\beta) = (-1)^n J_n(\beta). \tag{5.10}$$

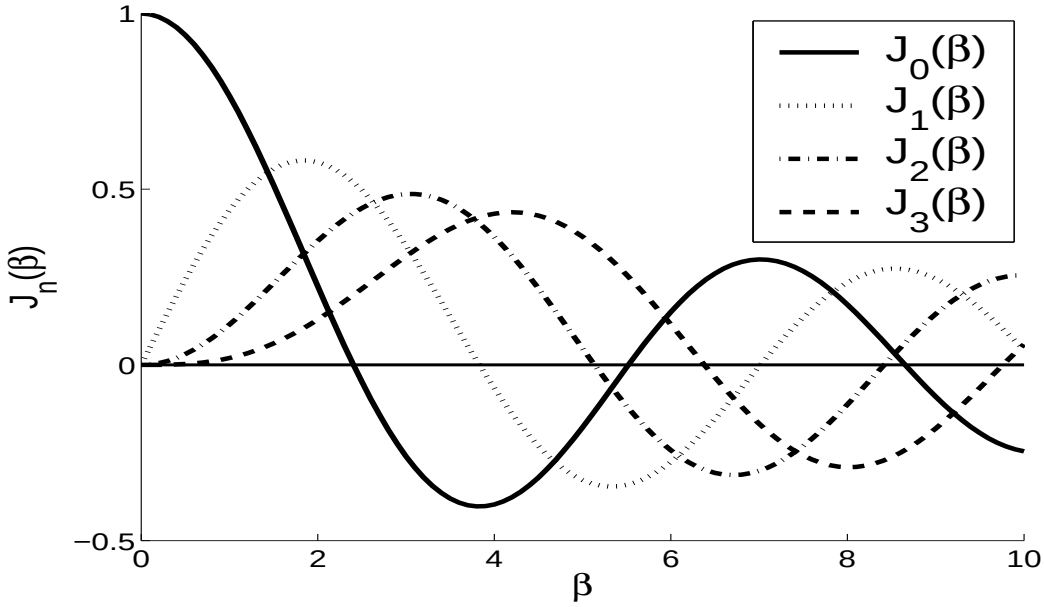

Figure 5.1: The Bessel functions J_0, J_1, J_2, J_3 as functions of β.

Comparing Eq. (5.9) with Eq. (5.3) and making use of Eq. (5.6), we have

$$I_n^F = E_0^2 J_n^2(\beta). \tag{5.11}$$

From the symmetry relation we can see that the phase modulated field has a symmetric Fabry-Perot spectrum.

2. The recurrence relation

$$J_{n-1}(\beta) + J_{n+1}(\beta) = \frac{2n}{\beta} J_n(\beta). \tag{5.12}$$

Using the recurrence relation, we can obtain the value of β from three neighboring components in the spectrum.

5.2.1 Determining V_π for the phase modulator

Experimentally, the modulated light spectrum signal measured by a Thorlabs 110 photo detector behind the homemade scanning FP interferometer was displayed and captured by a Lecroy WS434 digital oscilloscope, where the associated data for each spectrum could be stored as well. Figure 5.2 shows a series of screen captures of the phase modulated spectrum for 160 MHz modulation frequency. The RF signal used to drive the phase modulator originates from a signal generator. The signal is amplified and applied to the phase modulator (See Section 4.2.3). The corresponding signal generator output level was indicated under each spectrum image.

As indicated by Eq. (5.11), the intensity of each frequency component in the spectrum of the sinusoidally modulated light is proportional to $J_n^2(\beta)$. The relative value of $J_n(\beta)$ can thus be obtained by taking the square root of the peak intensity of each spectrum data. Since $J_n(\beta)$ is not always positive (see Figure 5.1), extra caution must be taken in determining the sign of the square root. Eq. (5.10) can be used to determine the sign of $J_{-n}(\beta)$. Having obtained $J_n(\beta)$'s, we can use Eq. (5.12) with various n to calculate β. For each spectrum, β was averaged over the values obtained with different n's. The modulation index β is plotted against the signal generator output V_{SG} in Figure 5.3 (a). The linear fit of the data gives a slope of 0.116 mV^{-1}, so

$$\beta = 0.116 V_{SG} \tag{5.13}$$

with V_{SG} in unit of mV. In Figure 5.3 (b), β is plotted against the RF input

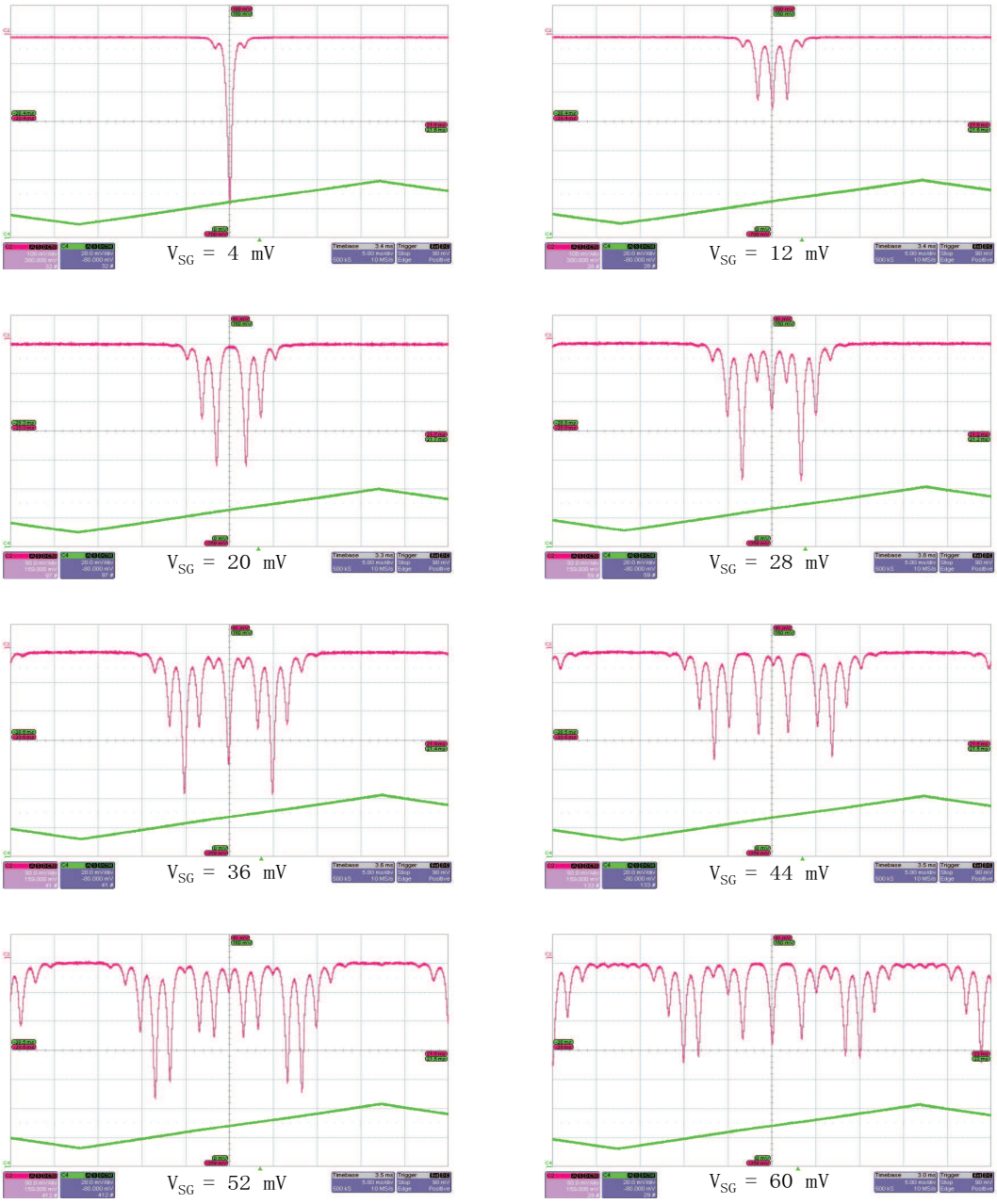

Figure 5.2: The phase modulation spectra for $\omega_{pm} = 160$ MHz measured by the homemade Fabry-Perot interferometer behind the big FA. The corresponding signal generator driving voltage is shown under each scope image. Note that the amplitude of the carrier frequency is zero for $V_{SG} = 20$ mV.

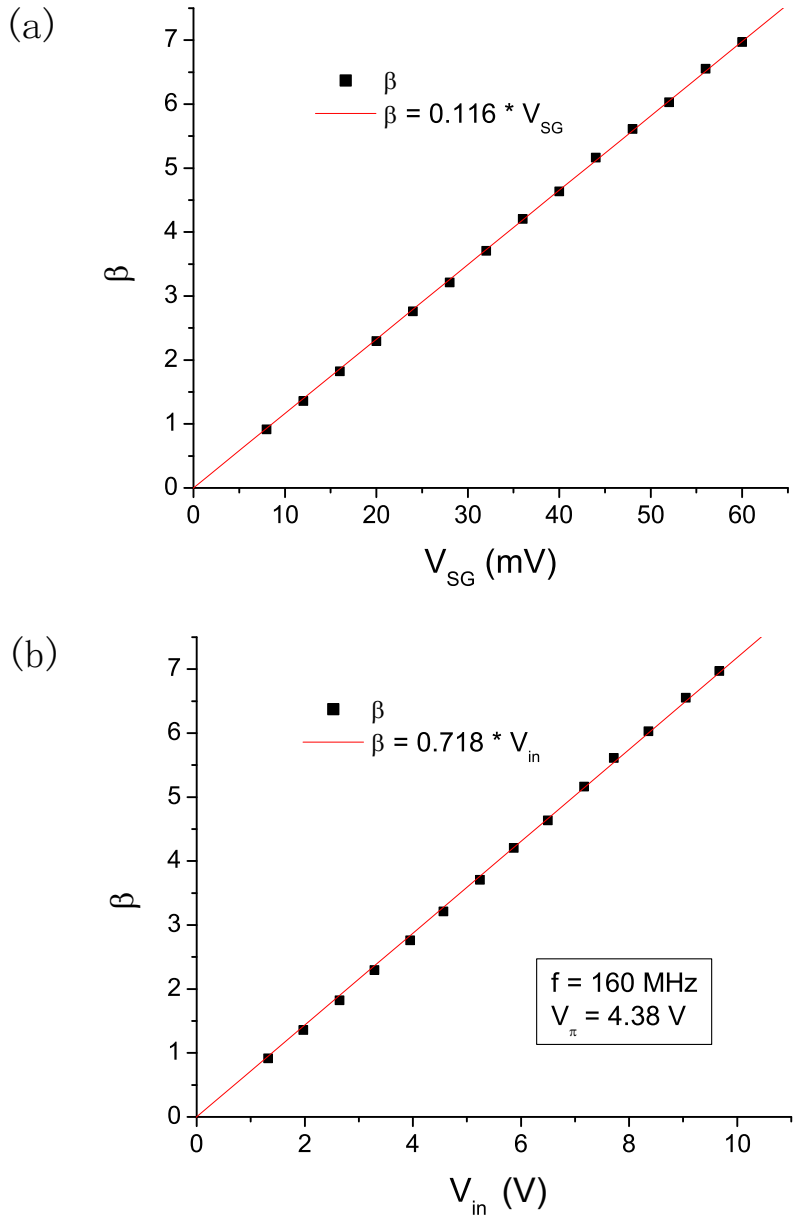

Figure 5.3: (a) The calibration curve of the phase modulation index β *vs.* the signal generator voltage V_{SG}. (b) The calibration curve of β *vs.* the input power of the phase modulator V_{in}. V_π was measured to be 4.38 V for the modulation frequency $\omega_{pm} = 160$ MHz.

of the phase modulator V_{in}, which is the amplified RF signal from the Mini-circuits amplifier. The linearly fitted slope is 0.718 V^{-1}, from which we can get $V_\pi = 4.38$ V for $\omega_{pm} = 160$ MHz.

The above phase modulated spectrum was measured behind the big fiber amplifier, so it is the final phase modulated signal delivered to the experiment. Two FP spectrometers were used simultaneously to compare between the phase modulated spectrum directly after the phase modulator and the one after the 1 W amplifier, and also between the spectrum after 1 W amplifier and the one after the 4 W amplifier. No visible differences were found. However, detailed analysis showed that the phase modulated spectrum right after the modulator fit better to the Bessel functions.

5.3 Amplitude Modulated Spectrum

The amplitude modulator output has the form described in Eq. (4.5), and we repeat it here,

$$E(t) = E_0 \cos \phi_a(t) \cos \omega_l t, \tag{5.14}$$

where $\phi_a(t)$ is proportional to the applied voltage

$$\phi_a(t) = \frac{\pi V(t)}{V_\pi}. \tag{5.15}$$

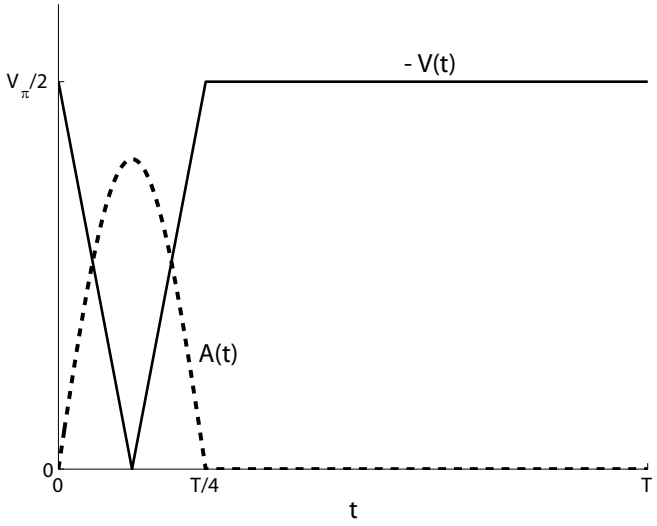

(a) modulating voltage and light amplitude

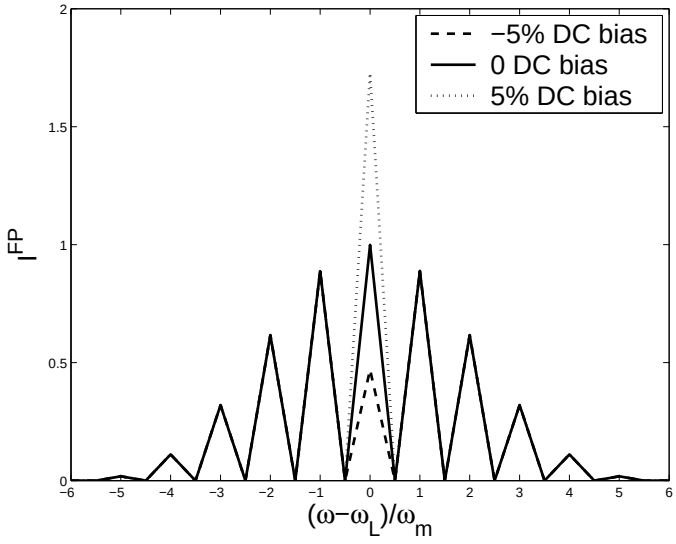

(b) Fabry-Perot spectrum of the light field

Figure 5.4: The idealized amplitude modulation scheme. The voltage $V(t)$ applied on the amplitude modulator is a triangular pulse, and the resulting light is a sinusoidal pulse of amplitude $A(t)$.

The Fabry-Perot spectrum of the light is

$$I^{FP}(\omega_l + n\omega_{am}) = |\frac{1}{T}\int_0^T dt E_0 \cos\phi_a(t) e^{-in\omega_{am}t}|^2, \tag{5.16}$$

where ω_{am} is the amplitude modulation frequency. The spectrum does not have an analytical formula except for special classes of $V(t)$. For example, an ideal case for our ARP experiment involves a syncopated (25% duty cycle) triangle-shaped electric pulse on the amplitude modulator as formulated below.

$$V(t) = -\frac{V_\pi(\omega_{am})}{2} + \frac{V_\pi(\omega_{am})}{2} \begin{cases} \frac{8t}{T} & 0 < t < \frac{T}{8} \\ \frac{8}{T}(\frac{T}{4} - t) & \frac{T}{8} < t < \frac{T}{4} \\ 0 & \frac{T}{4} < t < T \end{cases},$$

where $T = \frac{2\pi}{\omega_m}$ is the period of the amplitude modulation. For such electric pulse the light amplitude is

$$A(t) = \begin{cases} E_0 \sin 2\omega_{am}t & 0 < t < \frac{T}{4} \\ 0 & \frac{T}{4} < t < T \end{cases}. \tag{5.17}$$

The compliment of the electric pulse and the corresponding optical pulse are sketched in Figure 5.4(a). The resulting optical pulse is exactly the sinusoidal pulse as in our theoretical analysis.

For this case, the amplitude modulated spectrum is

$$I^{FP}(\omega_l + n\omega_{am}) = \left(\frac{4}{4 - n^2}\right)^2 \cos^2\frac{n\pi}{4}, \tag{5.18}$$

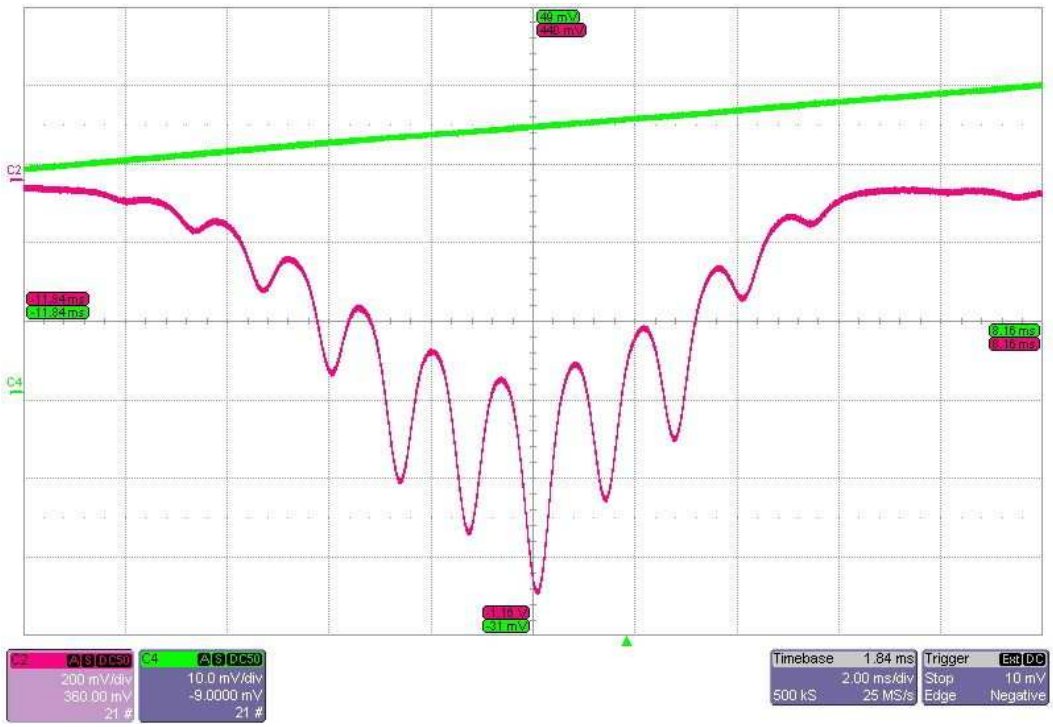

Figure 5.5: A Fabry-Perot spectrum of the amplitude modulated light in experiments. The straight line shows the ramping voltage applied on the PZT of the Fabry-Perot.

and it is plotted in Figure 5.4(b).

In the real experiments, the shape of the driving pulse is not exactly triangular, its amplitude is not exactly $V_\pi/2$, its width is not exactly $T/4$, and it also has some afterpulse ringing as indicated by Figure 4.6. So the optical pulse can never be ideally sinusoidal. But the Fabry-Perot spectrum of the amplitude modulated light is not too far from the ideal spectrum (see Figure 5.4(b)). A small level of CW light induced by DC offset of the electric pulse would cause the overlapping of the counterpropagating light pulses and could

ruin the ARP processes. It may not be manifested in the pulse profile taken by the fast photo detector (Thorlabs D400FC), but it is clearly shown in the Fabry-Perot spectrum. It can be minimized through the adjustment of the DC bias of the driving pulse. The Fabry-Perot interferometer is very handy for monitoring that since the peak at ω_l in the light spectrum is sensitive to the CW light level while other peaks are insensitive, as shown in Figure 5.4(b).

5.4 Phase and Amplitude Modulated Spectrum

In our experimental scheme, the phase modulation frequency, $\omega_{pm} = \omega_m = 160$ MHz; due to the syncopation, the amplitude modulation frequency $\omega_{am} = \omega_m/2 = 80$ MHz. Therefore, the common modulation frequency is $\omega_c = 80$ MHz. The modulated light field is

$$E = E_0 \cos\phi_a(t) \cos[\omega_l t - \beta \sin(\omega_m t + \delta\phi)], \tag{5.19}$$

and the Fabry-Perot spectrum is

$$I^{FP}(\omega_l + n\omega_c) = |\frac{1}{T}\int_0^T dt E_0 \cos\phi_a(t) e^{-i(\beta \sin(\omega_m t + \delta\phi) + n\omega_c t)}|^2, \tag{5.20}$$

where $\delta\phi$ in Eqs. (5.19) and (5.20) stands for the relative phase between the phase modulation and the amplitude modulation. For symmetric pulses with pulse width being T/4, ARP requires $\delta\phi = \pm\pi/2$ so that the frequency sweeps through resonance at the maximum pulse amplitude. In that case, the light field Eq. (5.19) is symmetric within the pulse, and the average frequency is

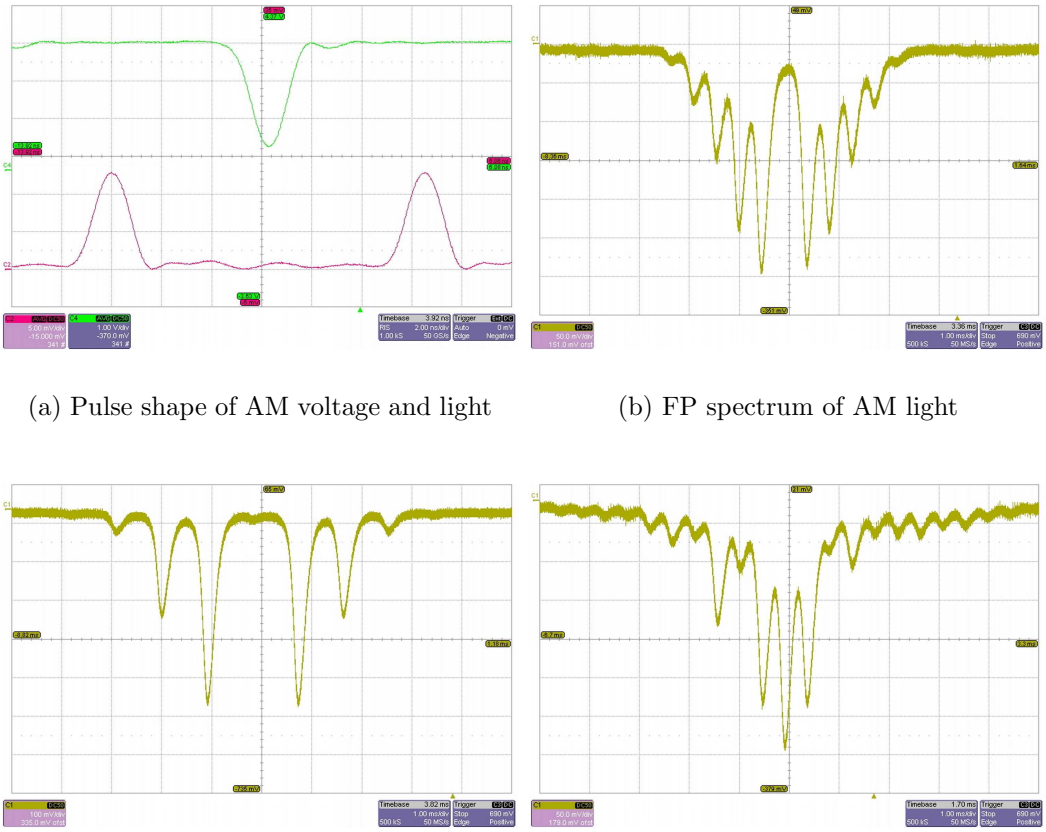

(a) Pulse shape of AM voltage and light

(b) FP spectrum of AM light

(c) FP spectrum of PM light

(d) FP spectrum of PM and AM light

Figure 5.6: Modulated light pulses and their Fabry-Perot spectra. $V_{SG} = 20$ mV for the phase modulator. AM voltage has about $-V_A/8$ DC bias, V_A is the amplitude of the RF voltage on the amplitude modulator.

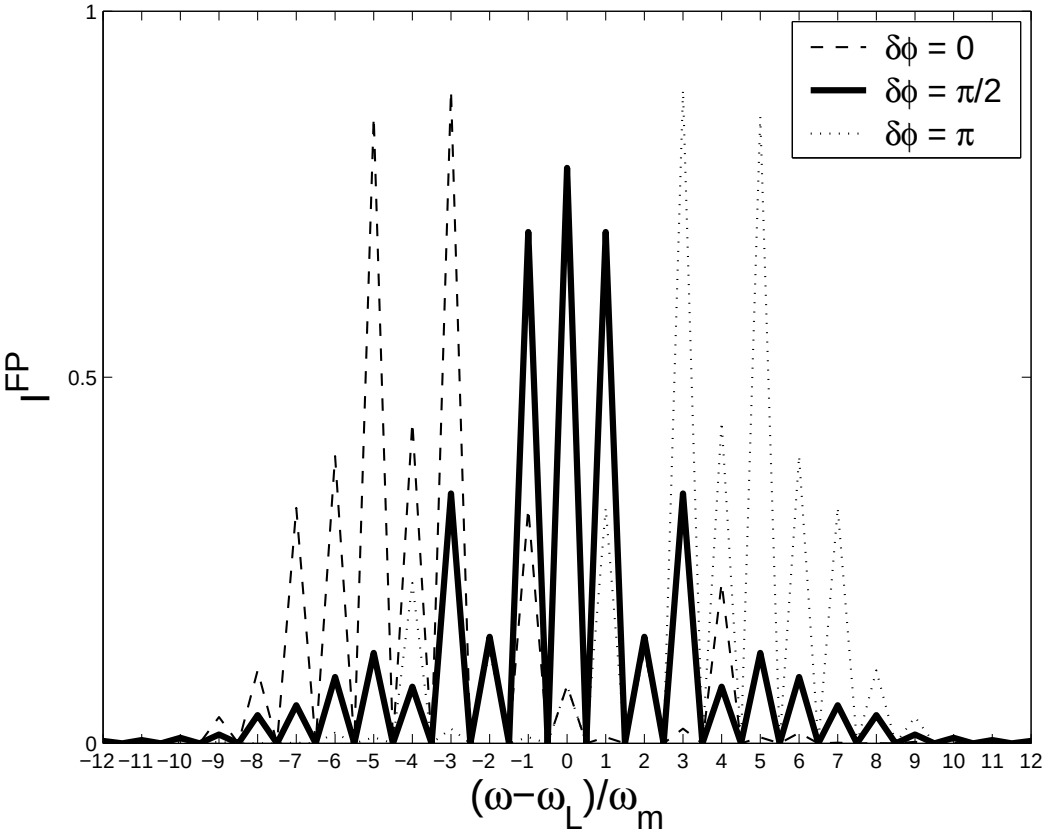

Figure 5.7: Fabry-Perot spectrum of the light pulses in Figure 5.6(d) numerically calculated from Eq. (5.20). $V_{SG} = 20$ mV for the phase modulator. AM voltage has $-V_A/8$ DC bias, V_A is the amplitude of the RF voltage on the amplitude modulator.

ω_l. On the other hand, If $\delta\phi \neq \pm\pi/2$, the pulse sweeps through resonance before or after the maximum amplitude, and the average frequency is blue or red shifted. By monitoring the Fabry-Perot spectrum of the modulated light, the spectrum is symmetric with respect to ω_l when $\delta\phi = \pm\pi/2$, while it is either blue or red shifted when $\delta\phi \neq \pm\pi/2$.

Figure 5.6 shows a set of FP spectra of modulated light captured by the digital scope. The voltage on the amplitude modulator shown in Figure 5.6(a) has about $-V_A/8$ DC bias, V_A is the amplitude of the RF voltage on the amplitude modulator, so that the FP spectrum of the amplitude modulated light shown in Figure 5.6(b) is small at the center. The control voltage on the phase modulator is $V_{SG} = 20$ mV, which corresponds to $\beta = 0.116\ V_{SG} = 2.32$. The FP spectrum of the phase modulated light is shown in Figure 5.6(c). When both modulators are turned on, the FP spectrum is shown in Figure 5.6(d), and the numerical calculated spectrum using Eq. (5.20) is plotted in Figure 5.7. The calculated spectra for $\delta\phi = \pi/2$ is in good agreement with the measured spectrum in Figure 5.6(d). This confirms that the phase modulation followed by the amplitude modulation does produce chirped pulses as expected. Figure 5.7 also plots the FP spectrums for $\delta\phi = 0$ and $\delta\phi = \pi$, which are red and blue shifted respectively. However, in the deflection experiment, we would like to have the amplitude modulated spectrum as shown in Figure 5.5, so that the optical pulse is more clean in the sense that the light level is minimized at the dark time.

The FP spectra in Figure 5.5 and Figure 5.6 were measured right after the amplitude modulator. That specific modulator failed in the experiment due to

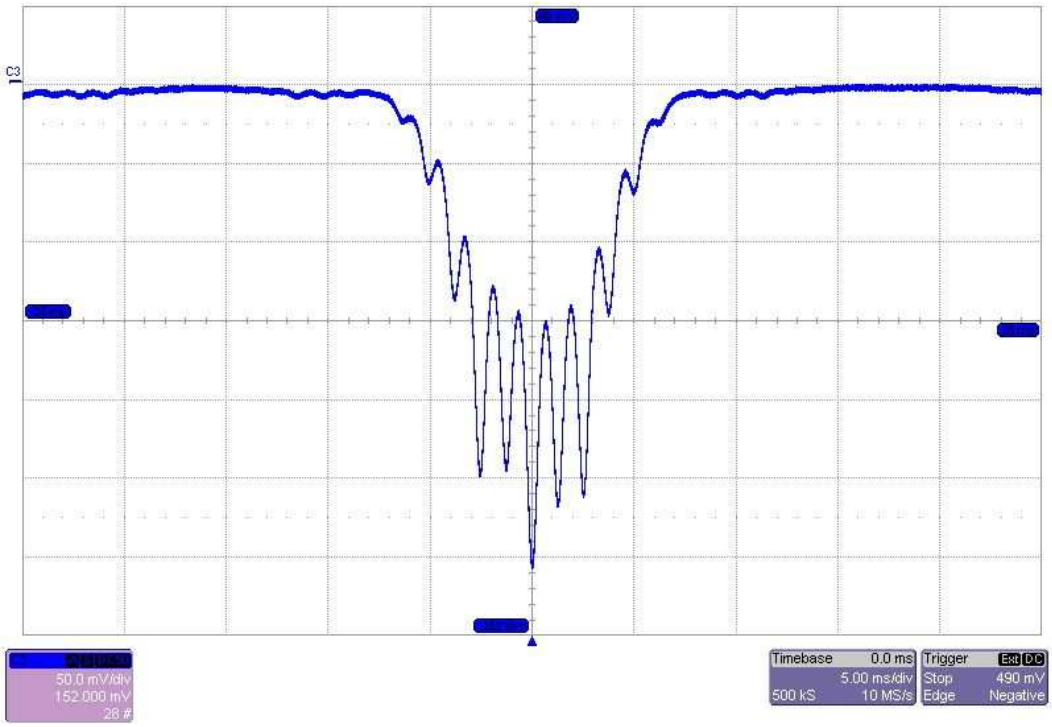

Figure 5.8: FP spectrum of the final amplitude modulated light pulse measured after the 4 W amplifier. The spectrum has more deviation from the spectrum of the ideal sinusoidal pulse than the previous one. The asymmetry of the spectrum is induced by the 4 W fiber amplifier.

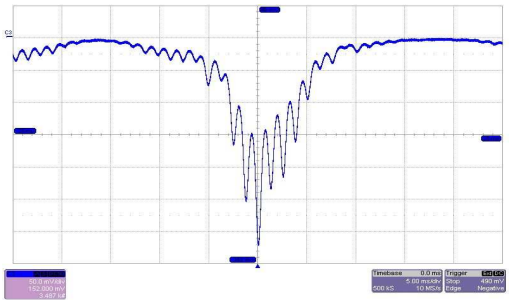

(a) Measured spectrum, $V_{SG} = 20mV$

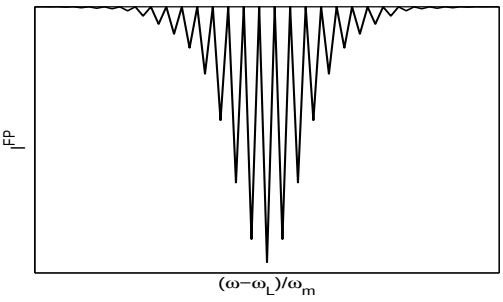

(b) Calculated spectrum, $V_{SG} = 20mV$

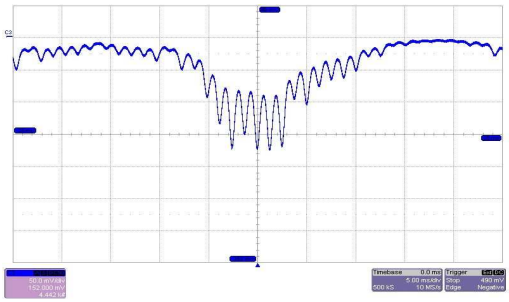

(c) Measured spectrum, $V_{SG} = 36mV$

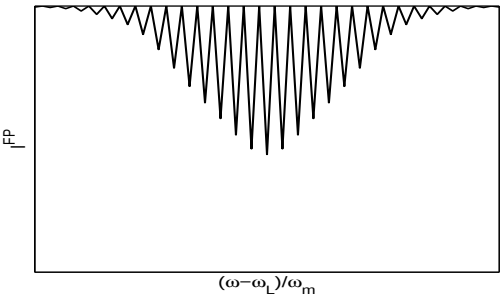

(d) Calculated spectrum, $V_{SG} = 36mV$

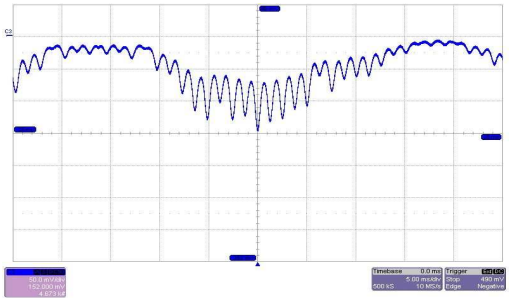

(e) Measured spectrum, $V_{SG} = 48mV$

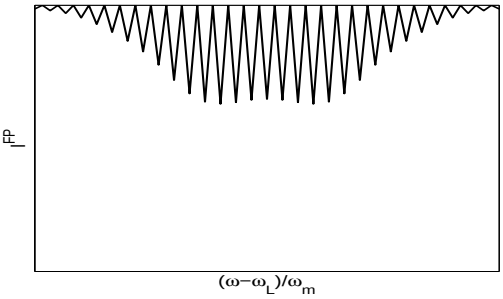

(f) Calculated spectrum, $V_{SG} = 48mV$

Figure 5.9: FP spectrum of modulated light after the fiber amplifier. Figures on the left are measured, the ones on the right are calculated by Eq. (5.20). The DC bias of the voltage on the amplitude modulator is nearly zero.

some intrinsic problem of the product. A modulator of the same model loaned by Photline was used to continue the experiment. The amplitude modulated spectrum taken with this modulator has more deviation from the spectrum of the ideal sinusoidal pules. Moreover, in the experiment, the modulated light has to pass through a fiber amplifier to gain more power before it interacts with the atomic beam. We found out that the amplified light induced some asymmetry in the amplitude modulated spectrum. The final amplitude modulated spectrum is shown in Figure 5.8. The combined spectrum for the chirped pulse are not exactly symmetric even for $\delta\phi = \pi/2$. We can try to adjust the phase delay to get the spectrum as symmetric as possible. The combined spectrum of the phase and amplitude modulated light are shown in Figure 5.9, they still more or less agree with the calculated spectra for the ideal pulse.

Chapter 6

Measurement of Optical Forces

6.1 Experimental Overview

As discussed in the previous chapters, the goal of this experiment is to investigate the optical force on atoms associated with periodic adiabatic rapid passages. We do this by measuring the deflection of He* atomic beam by periodic ARP sequences. A complete diagram of the experiment is presented in Figure 6.1. The atomic beam apparatus is covered in Chapter 3. The components of the optical system are described in detail in Chapter 4.

Under the constant acceleration assumption, which requires that the final transverse velocity is much smaller than the velocity capture range of the optical force, the final transverse velocity v_t of the He* atoms is

$$v_t = \frac{F}{m} \cdot t_{int} = \frac{F}{m} \frac{L_{int}}{v_l},$$

where F is the optical force on He* atoms, m is the atomic mass of He*, t_{int} is the interaction time, $L_{int} = 3 \sim 6$ mm is the interaction length, and v_l is the

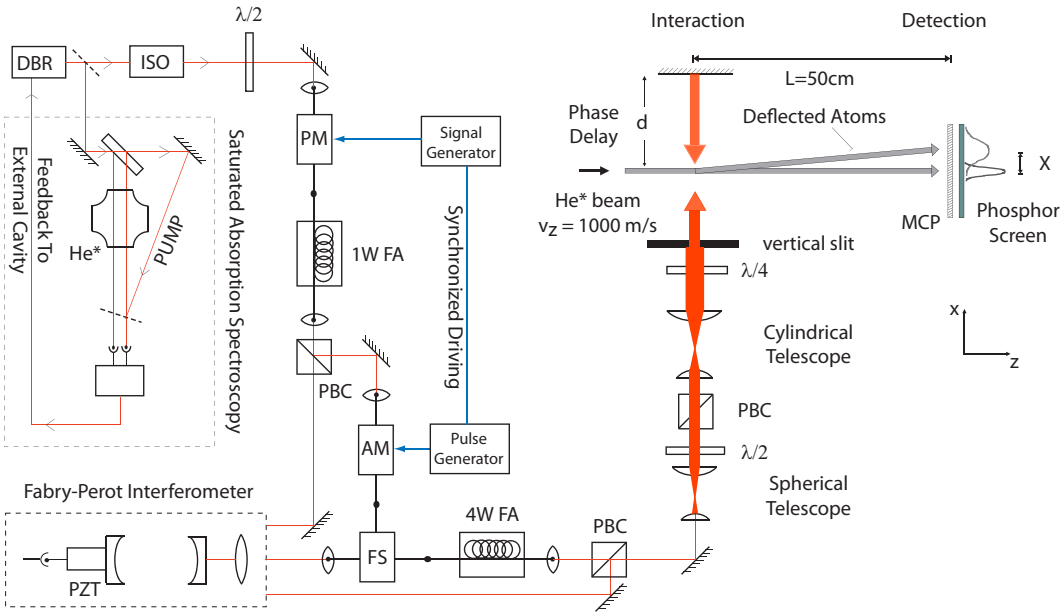

Figure 6.1: The complete diagram of the experiment. Each part of the optical system is explained in detail in Chapter 4. The He* atomic beam apparatus is described in Chapter 3. The flight distance of the deflected He* beam downstream of the interaction region is 50 cm.

longitudinal velocity of the atoms. The distribution of v_l determined by the TOF measurement is shown in Figure 3.3 [52]. F can then be calculated by measuring the deflection, X, of the atomic beam on the MCP/PS detector,

$$X = v_t \cdot t_{flight} = \frac{F}{m}\frac{L_{int}}{v_l}\frac{L_{flight}}{v_l}, \tag{6.1}$$

where the flight time t_{flight} is determined by the 50 cm flight distance, L_{flight}, and v_l. F is uniform under the constant acceleration assumption, so by Eq. (6.1) X is proportional to the inverse square of v_l. Since v_l has a wide distribution, X also has a wide spreading. For a characteristic X measured from the images of deflected atoms, a characteristic v_l must be obtained so that Eq. (6.1) can be used to calculate the optical force.

In the data processing below, we have used two types of characteristic value of X, namely, the peak value X_p and the average value X_a. Since X is proportional to v_l^{-2}, the peak/average value of X corresponds to the peak/average value of v_l^{-2}, rather than of v_l. The distribution of v_l^{-2} can be obtained by converting from the distribution of v_l in Figure 3.3. The profile of v_l^{-2} is plotted in Figure 6.2. From the figure, the peak of the v_l^{-2} distribution is at $v_l = 1080$ m/s, which is labelled as v_p; the average of v_l^{-2} corresponds to $v_l = 956$ m/s, which is labelled as v_a. Note that v_p and v_a are not the peak and average values of v_l with respect to its own distribution, as shown in Figure 6.2 instead they represent the v_l corresponding to X_p and X_a respectively.

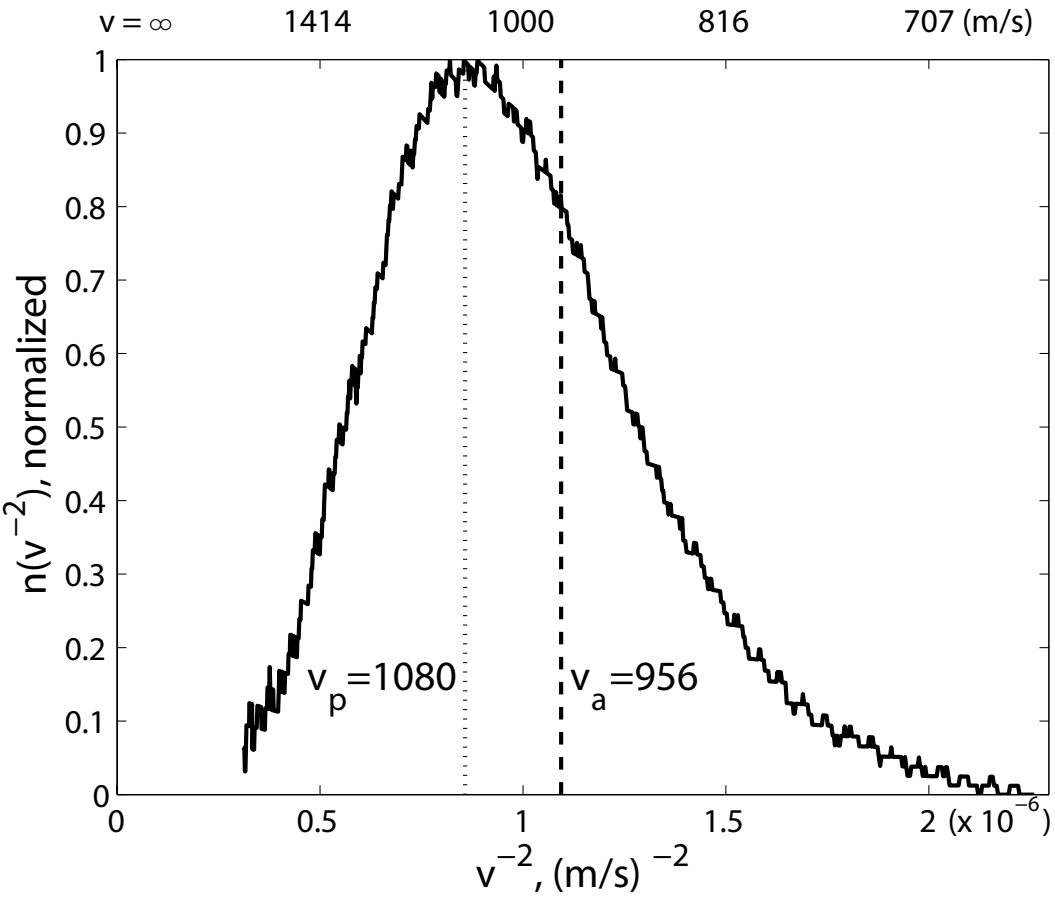

Figure 6.2: The distribution of the inverse square of the longitudinal velocity of He* beam. The source discharge current is 6 mA. The distribution is converted from the longitudinal velocity plotted in Figure 3.3. The vertical axis $n(v^{-2})$ is proportional to $v^3 n(v)$. The peak of inverse square velocity distribution is shifted from the peak in Figure 3.3 at 980 m/s to $v_p = 1080$ m/s. The inverse root of the mean of the inverse square velocity $v_a = 956$ m/s is also slightly different from the mean velocity 993 m/s in Figure 3.3.

6.2 ARP Force

We first measured the optical forces associated with the ARP sequences with $L_{int} = 6.0$ mm. The size of the laser beam was set by a cylindrical telescope to be $w_y = 2.1$ mm in the vertical direction and $w_z = 7.0$ mm in the longitudinal direction. The light intensity has the following Gaussian distribution,

$$I = I_0 \exp(-\frac{2y^2}{w_y^2} - \frac{2z^2}{w_z^2}). \tag{6.2}$$

A vertical slit of width 6.0 mm is used to cut off the wings of Gaussian beam along the long axis and set the interaction length. The light intensity drops by 31% from the center to the edge along the interaction length and the amplitude (Rabi frequency) drops by 17%.

The force of the ARP processes was measured with laser parameters $V_{SG} = 48$ mV, $\bar{P} = 1.75$ W, where V_{SG} is the output voltage of the phase modulator driver and $\bar{P}$ is the average optical power. The chirping frequency was 160 MHz, the pulsing frequency was 80 MHz and the laser was pulsed at $\sim$ 25% duty cycle. To compare with the theoretical prediction related to the nonadiabatic transition probability plotted in Figure 2.3, or more directly to the calculated force in Figure 2.7, we need to know the corresponding phase modulation index $\beta = \delta_0/\omega_m$ and the maximum Rabi frequency Ω_0. The phase modulation index β is related to V_{SG} by Eq. (5.13), which gives $\beta = 0.116 \times 48 = 5.57$, and so $\delta_0 = 5.57\omega_m = 2\pi \times 891$ Mhz. The maximum Rabi frequency Ω_0 of the light pulse can be derived from the average light power $\bar{P}$.

The light intensity I_0 is related to the Rabi frequency Ω by the saturation intensity I_s,

$$\frac{I_0}{I_s} = 2(\frac{\Omega}{\gamma})^2, \tag{6.3}$$

where the natural linewidth $\gamma = 2\pi \times 1.62$ MHz and $I_s = 0.167$ mW/cm^2 for the He* transition we used in the experiment [4]. For periodically pulsed light in one direction, the average power is

$$\begin{aligned} \bar{P} &= \frac{1}{T}\int_0^T dt \int dy \int dz I_0(t) \exp(-\frac{2y^2}{w_y^2} - \frac{2z^2}{w_z^2}) \\ &= \frac{\pi}{2} w_y w_z \frac{1}{T}\int_0^T dt I_0(t) \\ &= \pi w_y w_z I_s \frac{1}{T}\int_0^T dt (\frac{\Omega(t)}{\gamma})^2. \end{aligned}$$

Assuming $\Omega(t) = \Omega_0 f(t)$, where $f(t)$ is the pulse shape function, the average power is

$$\bar{P} = \pi w_y w_z I_s (\frac{\Omega_0}{\gamma})^2 \cdot \frac{1}{T}\int_0^{T_p} dt f^2(t). \tag{6.4}$$

Presuming a sinusoidal pulse shape as in Figure 5.4(a) and Eq. (5.17), we have $f(t) = \sin \omega_m t$, and $T_p = \pi/\omega_m$, $T = 4T_p$. Therefore, $\frac{1}{T}\int_0^{T_p} dt f^2(t) = \frac{1}{8}$, and

$$\bar{P} = \frac{\pi}{8} w_y w_z I_s (\frac{\Omega_0}{\gamma})^2. \tag{6.5}$$

So $\bar{P} = 1.75\ W$ gives us $\Omega_0 = 426\gamma = 4.31\omega_m$. Combined with $\delta_0 = 5.57\omega_m$, the predicted nonadiabatic transition probability is 0.025 from Figure 2.3, and the corresponding theoretical optical force is about $16F_{rad}$ from Figure 2.7.

The atomic beams were imaged on the MCP/PS detector, and the images

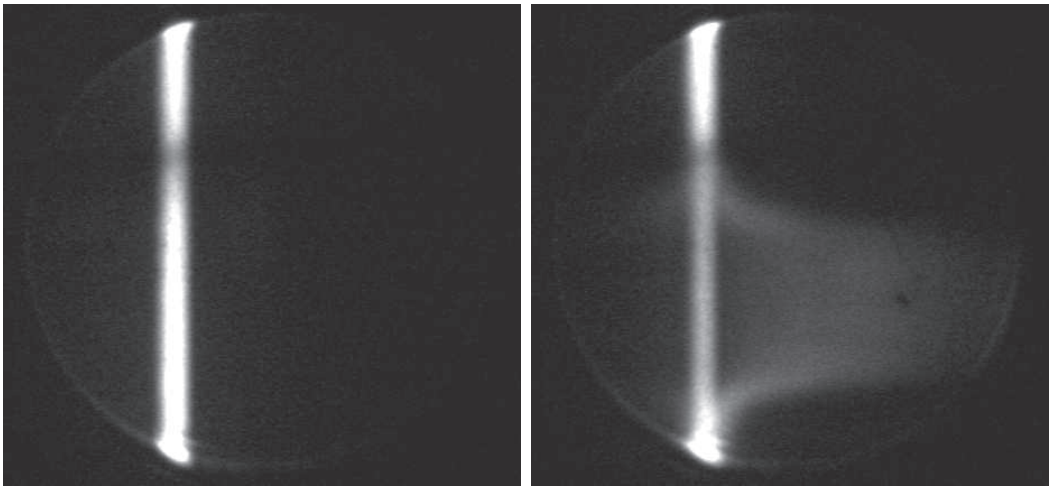

(a) Undeflected signal with UV

(b) Deflected signal with UV

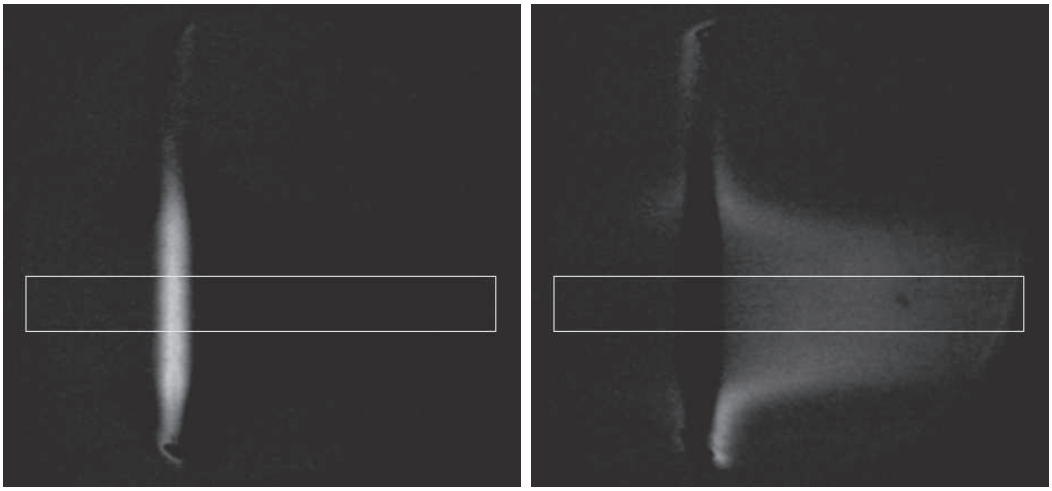

(c) Undeflected atoms without UV

(d) Deflected atoms without UV

Figure 6.3: Atomic deflection with Periodic ARP pulses. V_{SG} = 48 mV, $\bar{P}_{optical}$ = 1.75 W, laser beam size = 2.1 mm × 7.0 mm, L_{int} = 6.0 mm. (a) and (b) are the original images on the phosphor screen; (c) and (d) are processed images with UV background subtracted. The rectangular boxes in (c) and (d) are the region over which the atom intensity was averaged to get a profile of the atomic distribution for the undeflected and deflected atoms.

were captured by the CCD camera. The image of the beam with laser beam blocked is shown in Figure 6.3(a); the image of the beam with laser beam on is shown in Figure 6.3(b). In the lower part of Figure 6.3(b), most atoms were deflected to the right side of the screen to leave a dark region between the slit region and deflected atoms. Assuming that all atoms in the interaction region were deflected, we attribute the remaining signal in the slit region of Figure 6.3(b) to the UV background from the discharge. In practice, it could be obtained as the minimum of the intensity distribution in Figure 6.3(a) and Figure 6.3(b).

The UV background was then subtracted from Figure 6.3(a) and Figure 6.3(b), which gave us the distribution of the atomic signal in the undeflected beam and the deflected beam. The UV subtracted images are shown in Figure 6.3(c) and 6.3(d). The intensity variation of the deflected atoms in the vertical direction in Figure 6.3(d) corresponds to the Gaussian profile of the laser beam along the y-axis. The optical force was measured for the atoms deflected at the vertical center of the laser beam, where the light intensity was the strongest. For that purpose, the intensity of the atomic signals was averaged along a long box as shown in Figure 6.3(c) and Figure 6.3(d). The resulting profiles are plotted in Figure 6.4. The peak of the deflected atoms is shifted from the peak of the undeflected atoms by $X_p \sim 7.5$ mm. Using Eq. (6.1) and the corresponding longitudinal velocity $v_p = 1080\ m/s$, we estimated the optical force to be

$$F = \frac{m v_p^2 X_p}{L_{int} L_{flight}} = 6.2 F_{rad}. \tag{6.6}$$

The measured force is about 40% of the theoretical prediction of $16 F_{rad}$.

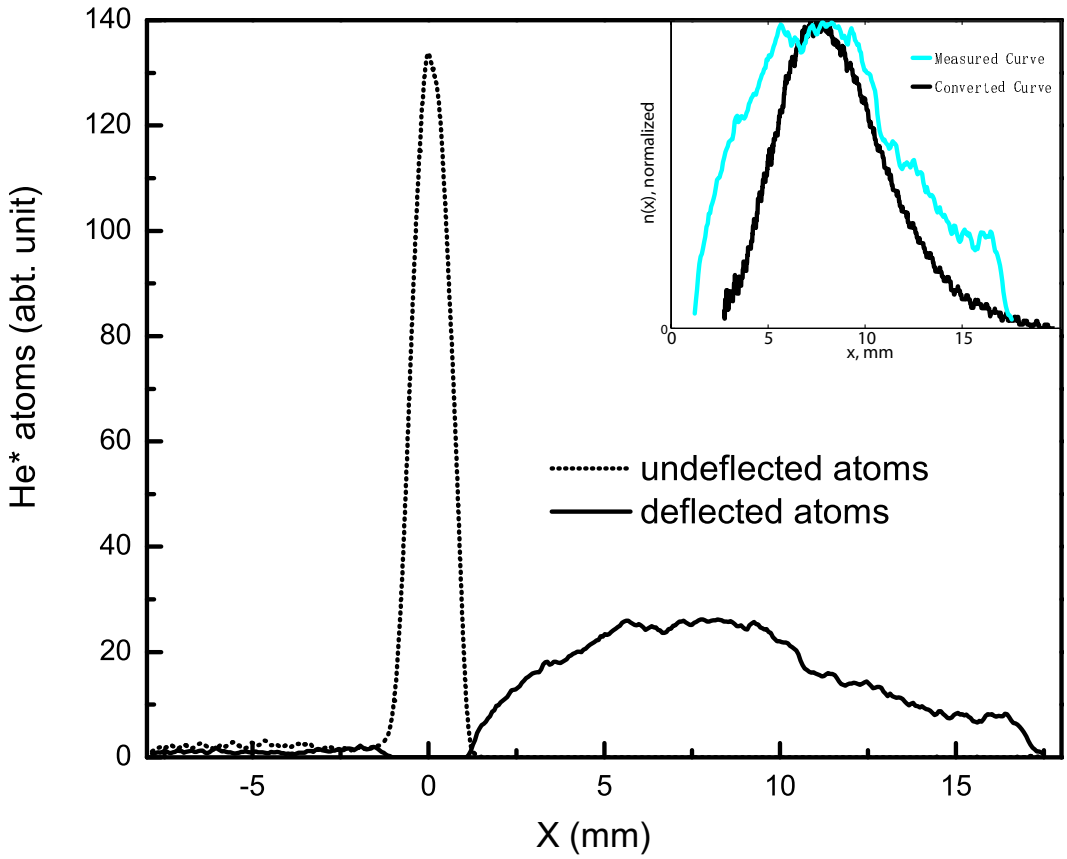

Figure 6.4: The signal profiles of deflected/undeflected atoms in the interaction region. The profiles are averaged over the box indicated in Figure 6.3(c) and Figure 6.3(d). The peak of the deflected atoms shifted from the peak of the undeflected atoms by $\sim$ 7.5 mm. The inset of Figure 6.4 shows the profile for the deflected atoms together with v_l^{-2} distribution of Figure 6.2 converted from the TOF measurement. Except some artifacts, the main difference is that the measured profile of the deflected atomic has a broader peak. This can be attributed to the width of the initial atomic distribution. Except these, the two distribution have similar shapes.

In the inset of Figure 6.4, we plotted the profile for the deflected atoms measured in the experiment together with v_l^{-2} distribution of Figure 6.2. There are some artifacts in the measured profile due to the phosphor screen non-uniformity. The little bump at the tail on the right-hand edge of the measured curve is produced by the edge of the screen and the measured profile is cut off after that point. Besides these artifacts, we see that the measured profile has a broader peak. The measured curve on the inset of Figure 6.4 is about 1.7 mm wider on each side than the v_l^{-2} curve. Most of the broadening can be attributed to the finite width of the initial atomic distribution as shown by the undeflected beam profile in Figure 6.4. The slit used to define atomic beam is about 0.3 mm, the initial atomic distribution measure on the screen has a 1.2 mm (FWHM) width. The resulting distribution of deflected atoms is thus a convolution of this initial atomic distribution and the converted distribution from Figure 6.2. The rest of the broadening could have to do with the peak height which is affected by the non-linearity of the detector. Including these broadening effects, the two peaks have similar shapes. This supports our method of the force calculation.

6.3 Force Map

Our next step is to systematically study the dependence of the optical force associated with chirped pulses on the chirping amplitude δ_0 and the pulsing amplitude Ω_0, so that we can compare forces with theoretical predictions in the two dimensional pulse parameter space. The modulation scheme and the light beam size are the same as above. However, the interaction length

was reduced to $L_{int} = 3.0$ mm so that the variation of the Rabi frequency along the interaction length was reduced to 4.5%. An essentially uniform field along the interaction length guarantees the accuracy of the force mapping in the pulse parameter space. Also a shorter interaction length assures that all of the deflected atoms fall into the detection area of the MCP/PS detector. Images of the undeflected He* beam were recorded. While doing the force mapping, the phase modulator driving voltage V_{SG} varied from 0 to 56 mV in increments of 4 mV. The corresponding modulation index were calculated with Eq. (5.13). For each V_{SG}, the current of the fiber amplifier pumping diode was fixed at 4000 mA with a total power of slightly more than 2 W. Due to the loss along the optical path, the maximum power delivered to the atomic beam is about 1.75 W. The intensity of the laser pulses was then conveniently adjusted by rotating a $\lambda/2$ (with a PBC) in front of the interaction region. The rotation angle ranged from 12° to 52° with a step size of 4°. At each angle, the atomic deflection image was taken, the corresponding power of the transmitted light (by the PBC) was also measured and Eq. (6.5) was used to calculate the peak Rabi frequency. The measured intensity variation fits well with the $\sin^2\theta_{\lambda/2}$ curve as expected for the linearly polarized light passing through the $\lambda/2$ plate.

A total of 15×11 deflection images were taken for an experimental run. In Figure 6.5, we show a 3×3 subset of the deflection images. The images on the same column have the same chirping amplitude δ_0 and the images on the same row have the same Rabi frequency Ω_0. The experimental parameters and the calculated pulse parameters are indicated under each image. The first

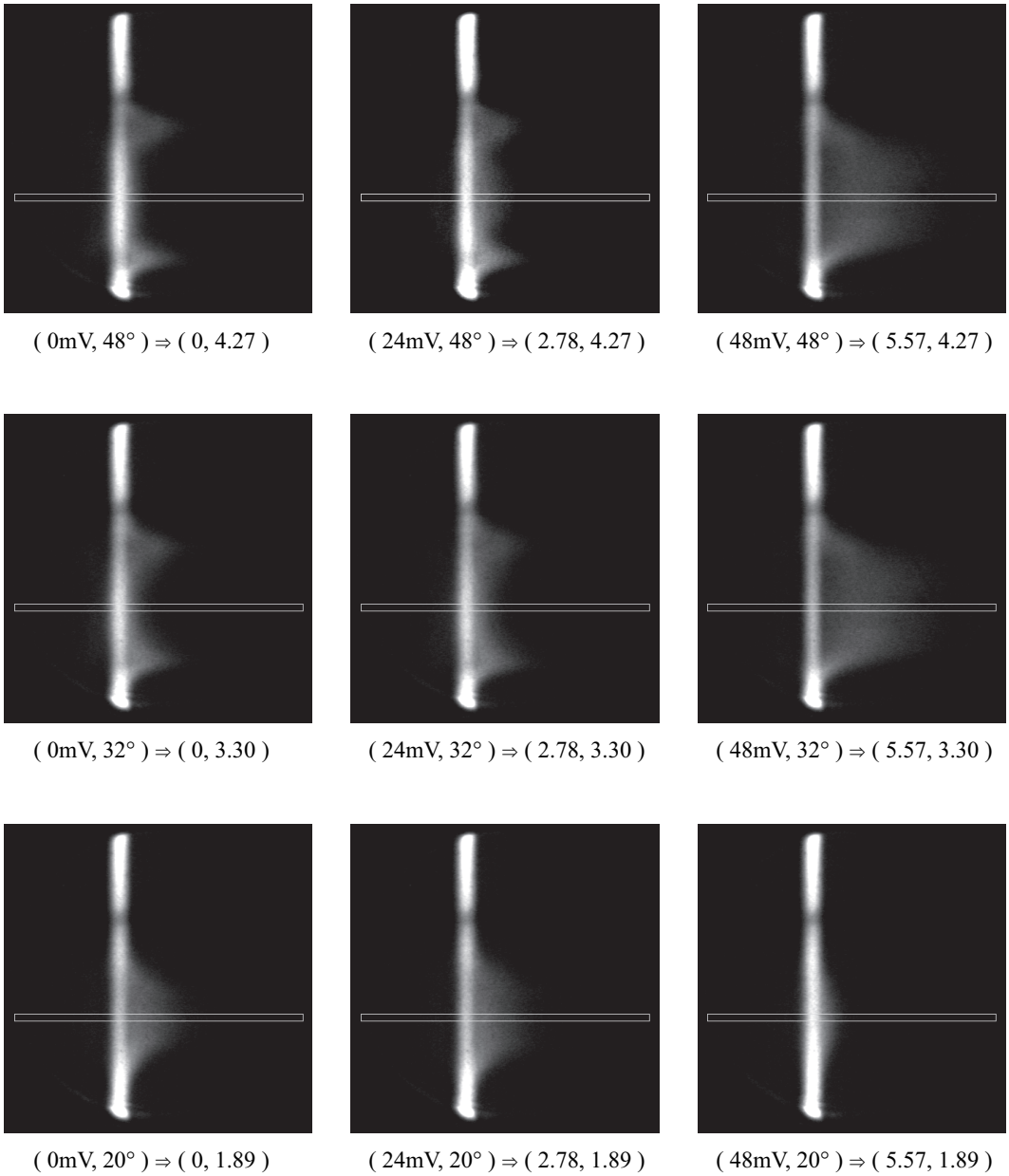

Figure 6.5: A subset of deflection images. The experimental parameters are indicated below each image. Parameters in the first parentheses are $(V_{SG}, \theta_{\lambda/2})$. Parameters in the second parentheses are $(\delta_0/\omega_m, \Omega_0/\omega_m)$. The boxes show the region over which the atom intensity was averaged for the force calculation.

column has $\beta = 0$ so the laser pulses are non-chirped. The top and the middle image on the third columns ($\beta = 5.57$) demonstrate the large deflection of the atoms by periodic chirped pulses. The images on the second column show the force variation for medium range ($\beta = 2.78$) chirped pulses.

A Matlab code was written for systematic analysis of these image. The image analysis procedures are basically the same as described in Section 6.2. The force calculations are slight different. First, since the deflected atomic distributions have broad peaks, it is more systematically consistent and more easily automated to compute the average atomic deflection than to pick peaks from the distribution profiles of the deflected atoms. Therefore, X_a rather than X_p was obtained for each deflection image. Correspondingly, $v_a = 956$ m/s should be used for the longitudinal velocity in Eq. (6.1) to evaluate the force. Second, a narrower box was used in obtaining the average atomic profile distribution for all the images since the force in the non-ARP region is more intensity sensitive and has a narrower deflection peak than in the ARP region. The regions over which the atomic intensity was averaged are drawn on the images in Figure 6.5. Finally, at each point of the $(\delta_0/\omega_m, \Omega_0/\omega_m)$ space, the optical force on atoms produced by periodic chirped pulses was obtained. In Figure 6.6 the obtained force value in units of F_{rad} is plotted in the parameter space of $(\delta_0/\omega_m, \Omega_0/\omega_m)$. The magnitude of the force is indicated by the color. The maximum force measured in the ARP region is $7.6F_{rad}$, which again yields 40% of the predicted value.

As we see from the averaging box drawn on images in Figure 6.5, the force map Figure 6.6 was calculated from the center of the deflection area

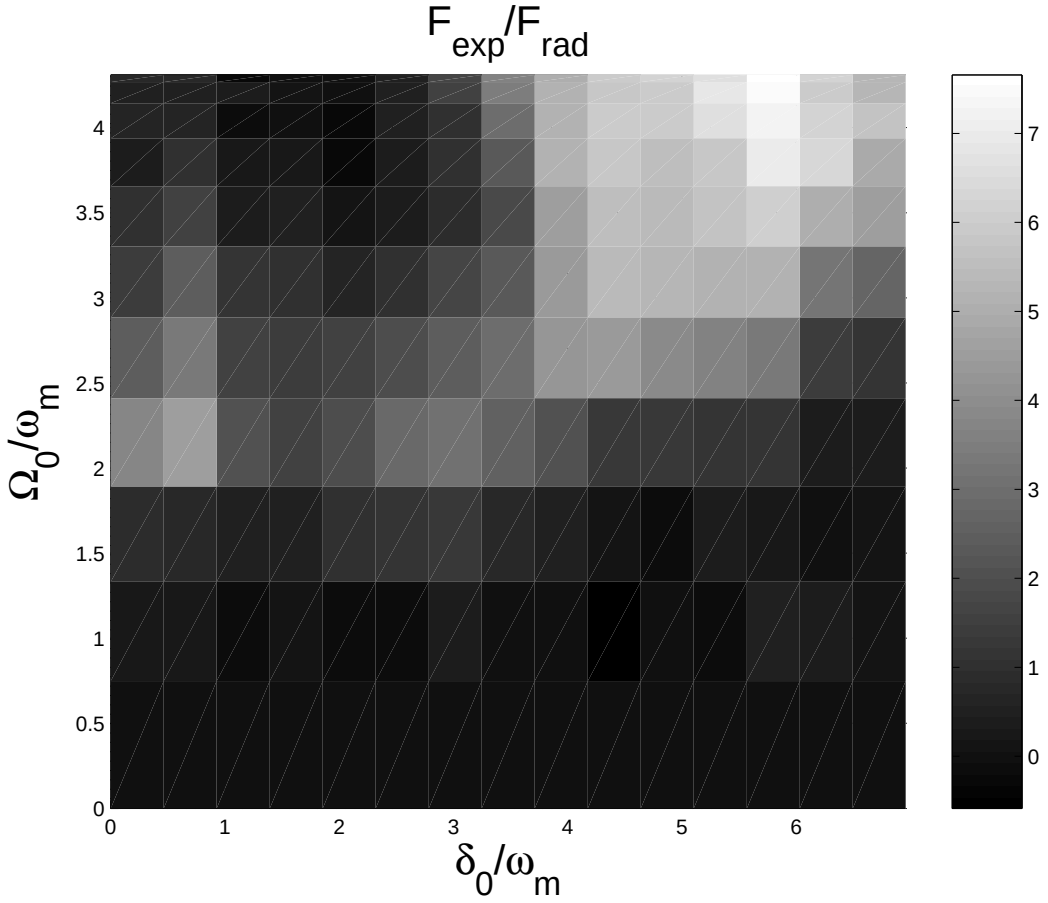

Figure 6.6: Force map. Interaction region = 3 mm. The force at each point was calculated with Eq. (6.1) by measuring the average deflection of the atoms from the captured MCP/PS image. The unit of the force is F_{rad}.

in each image. Since the laser beam has a Gaussian profile in the y (vertical) direction with $w_y = 2.1$ mm, the light intensity (and thus the Rabi frequency) is strongest in the center of the interaction region and fades out towards the edges. This explains the vertically symmetric deflection image on the MCP/PS. Looking at the first column of Figure 6.5 where the pulses are non-chirped, the bottom image shows a maximum deflection at the center of the interaction region where light intensity is maximum. This means the Ω_0 satisfies the π-pulse condition and thus induces a big force. When Ω_0 increases, it does not satisfy the π-pulse condition anymore. However, the wings of the Gaussian beam have lower intensity and the π-pulse condition is satisfied somewhere on the wings. This contributes to the two side peaks in the deflection image in the middle. In the top image where we have higher Ω_0, we see the two side peaks moving further apart (down to the Gaussian wings). Further increasing of Ω_0 presumably would show the rise of the third peak in the center again if Ω_0 satisfies the 3π-pulse condition. Unfortunately, the experimental conditions didn't allow us to reach such high intensity.

In the second column of Figure 6.5 where $\beta = 2.78$, the lower and the middle images show characteristics similar to the characteristics of the images for $\beta = 0$. However, in the top image, we did see the rise of the third peak in the middle. The reason can be found in Figure 2.3 and Figure 2.7, where the contour curve extended from the π-pulse point and the curve from the 3π-pulse point join in the ARP region, and so the top branch has a negative slope. The total inversion condition for the top branch is satisfied with lower intensity for chirped pulses. This agrees with what we saw in the experiment.

Lastly, the deflection images in the third column show the robustness of ARP forces. Once the intensity is above the threshold, the force is in general large and does not vary much with intensity.

Additional information beyond that available from the center deflection can be extracted from the images by projecting the Gaussian profile of the light in the vertical direction to the detection region. Since the aperture in the He* source skimmer plate is very small, we assume it is a point source. The distance from the source to the interaction region is 1/3 of the distance from the source to the detection region. This means that a vertical deviation Y from the deflection center on the MCP/PS images corresponds to a deviation $y = Y/3$ in the interaction region, where the peak Rabi frequency drops to $\Omega_0 \exp(-y^2/w_y^2)$. With this in mind, we can use off-center deflection signals to calculate the force and map it onto the parameter space. In Figure 6.7 we plotted the calculated force versus the Rabi frequency for $\beta = 0$, 2.78, and 5.57 with the vertical deviation from the deflection center on the images being $Y = 0$ mm, 1 mm, 2 mm, 3 mm, and 4 mm respectively. The corresponding position and averaging area for every Y are shown as the rectangular boxes in Figure 6.5. We can see that the force curves calculated with different Y's overlap with each other for all three β values.

Although the force measured in the experiment is only about 40% of the theoretical value in the ARP region and 20% in the π-pulse region, the variation of the relative force in parameter space agrees with the theoretical prediction. In Figure 6.8 we plot in the space of $(\delta_0/\omega_m, \Omega_0/\omega_m)$ the contours of the force measured in the experiment and the contours of $1 - \sqrt{P_{nad}}$ side

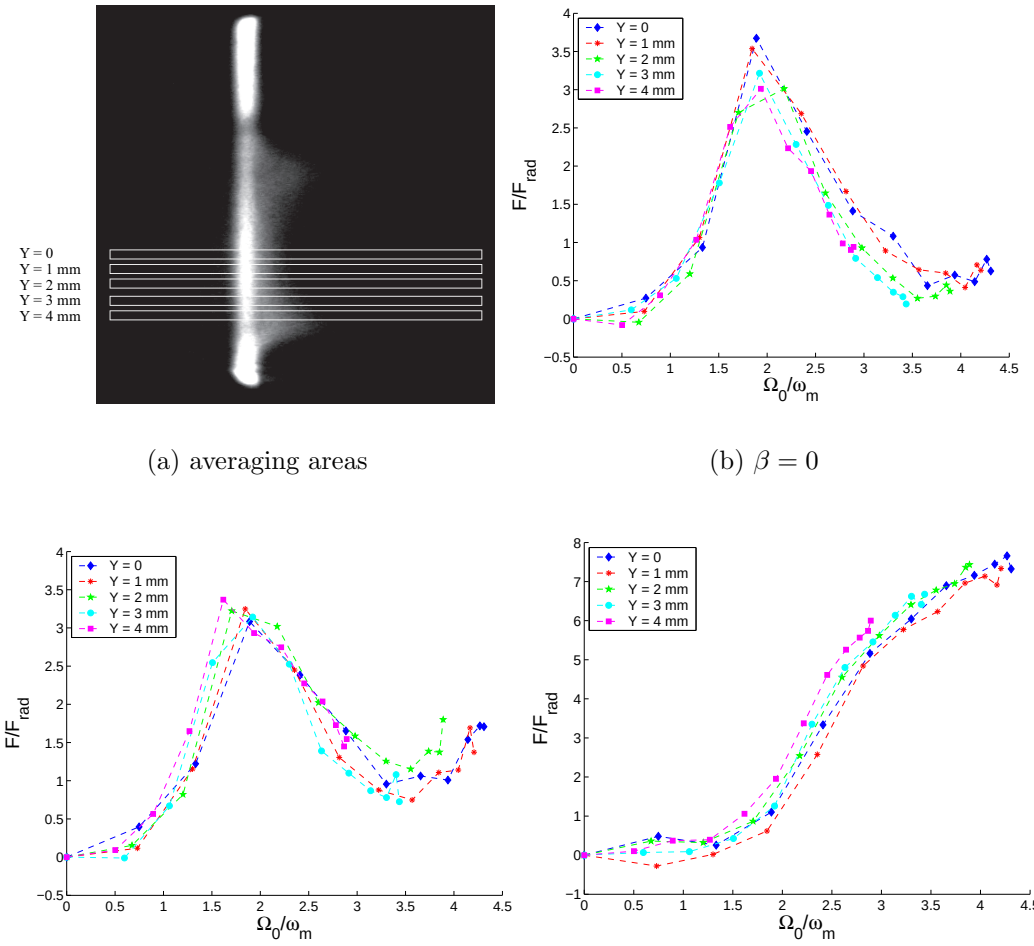

(a) averaging areas

(b) $\beta = 0$

(c) $\beta = 2.78$

(d) $\beta = 5.57$

Figure 6.7: The force were calculated from the measured deflections with $Y = 0$ mm, 1 mm, 2 mm, 3 mm, and 4 mm on the deflection images. Y is the vertical deviation from the center of the interaction region on the screen. The position and averaging area of each Y is shown in (a). (b), (c) and (d) show the force calculated with different Y vs. Ω_0/ω_m for $\delta_0/\omega_m = \beta = 0$, 2.78, and 5.57 respectively. Forces curve with different Y agree with each other. In (b) we can clearly see the that force increases again for higher Rabi frequency. This confirms the oscillation of the force with Ω_0/ω_m.

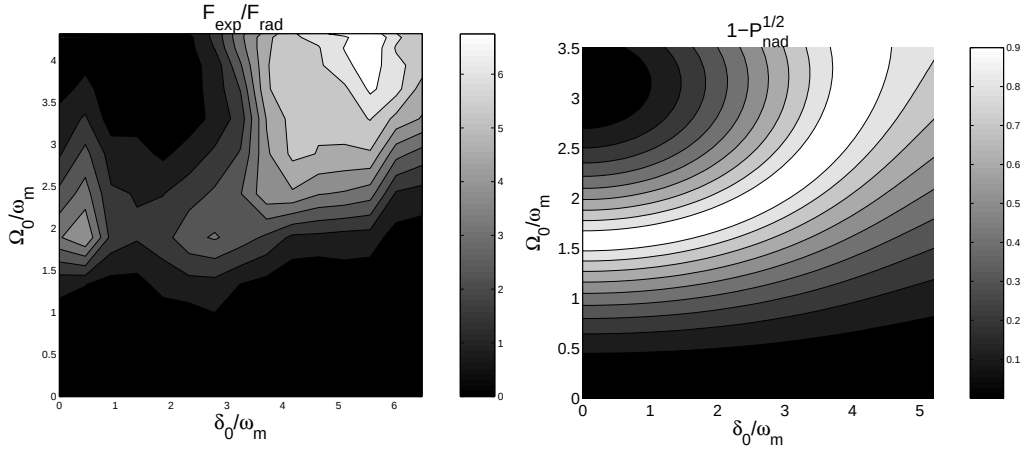

(a) Undeflected signal with UV

(b) Deflected signal with UV

Figure 6.8: The contours of the force measured in the experiment and the contours of $1-\sqrt{P_{nad}}$ are plotted in (a) and (b) in the space of $(\delta_0/\omega_m, \Omega_0/\omega_m)$. The two plots are scaled differently, but they do look very similar.

by side, where P_{nad} is the non-adiabatic transition probability for a single cosinusoidally chirped sinusoidal pule. The theoretical analysis gives that $1-\sqrt{P_{nad}}$ is proportional to the force. The similarity between the contour plots indicates that the relative change of the optical force in the parameter space is correctly predicted by the theory of nonadiabatic transitions in Chapter 2.

As for the small absolute value of the force compared with the theoretical expectation, besides the experimental error in power measurement, and the systematic errors from the nonlinear and the nonuniform phosphor screen response, the discrepancy can be mainly attributed to the non-ideal pulse shape. As shown in Figure 5.6(a), the pulse shape in the experiment was not an ideal sinusoid shape as in the theoretical derivation, and the tails of the laser pulses

extended longer than 3.125 ns required for 25% duty cycle pulsing so that the counterpropagating light pulses slightly overlapped. Furthermore, the 4 W fiber amplifier induced degradation of the chirped pulse as revealed in Figure 5.9. The even smaller force in the π-pulse region can be explained by the poor measurement resolution. The increasing step of the peak Rabi frequency is too big in that region, so we could just miss the peak. Despite all these non-ideal effects, the experiment realized large optical forces and confirmed the theoretical distribution of the force in the parameter space.

6.4 Velocity Capture Range

Finally, we measured the velocity capture range of the optical force associated with the ARP sequences by tilting the light beam relative to the normal of the atomic beam propagation direction. In general, the larger the transverse velocity of the atoms, the smaller the optical force should be. Figure 6.9 shows the deflected atoms for various angles of light beam tilt. The tilt angle is defined to be the deviation of the direction of the light beam from the normal to the side window of the interaction chamber. At every tilt angle, the last $\lambda/2$ plate in front of the interaction region has to be readjusted to guarantee circular polarization. The retro-reflection mirror also has to be realigned. Due to mechanical restrictions, the tilt angle in the measurement was confined between -1.4° and 2.8°, where the negative angle means tilting away from the MCP/PS detector and the positive angle means tilting toward the detector. However, the measurement result was more qualitative than quantitative for various reasons.

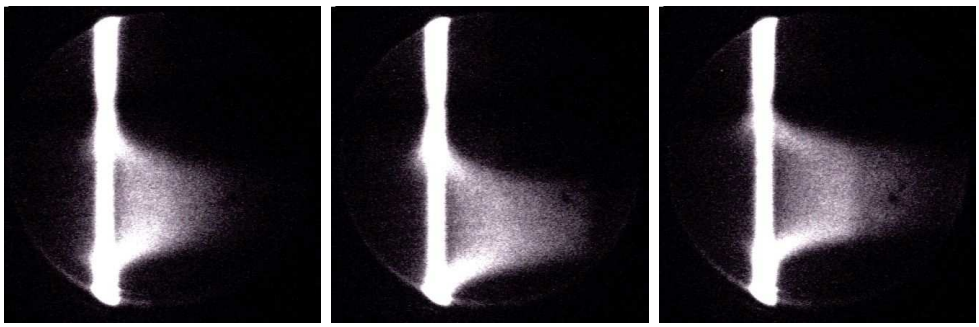

(a) $\theta_{tilt} = 2.8°$ (b) $\theta_{tilt} = 2.2°$ (c) $\theta_{tilt} = 1.6°$

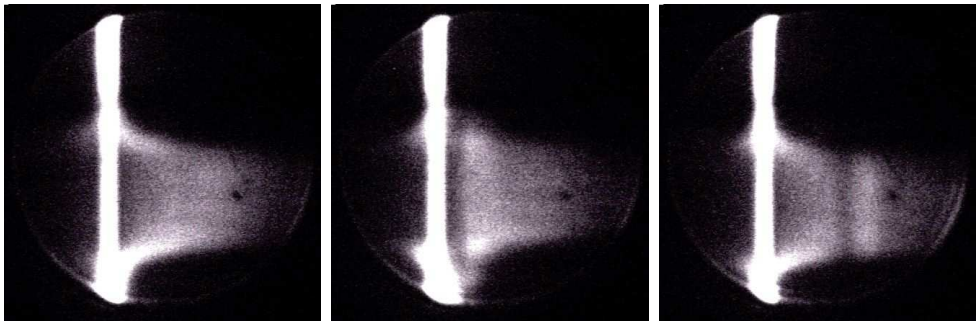

(d) $\theta_{tilt} = 1.0°$ (e) $\theta_{tilt} = 0.4°$ (f) $\theta_{tilt} = -0.2°$

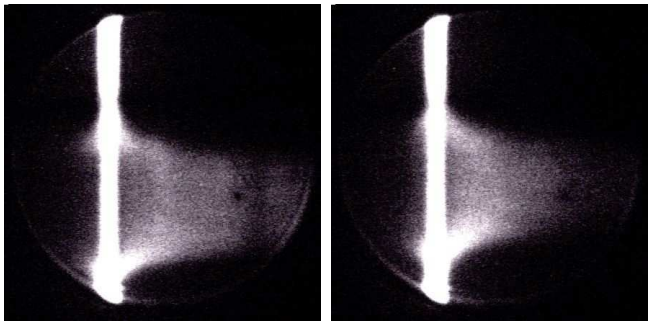

(g) $\theta_{tilt} = -0.8°$ (h) $\theta_{tilt} = -1.4°$

Figure 6.9: The deflection of He* atoms by tilted light beams. The interaction length is 6 mm. $V_{SG} = 48$ mV, $\bar{P} = 1.75$ W. The figures shown here are contrast-enhanced for visualization.

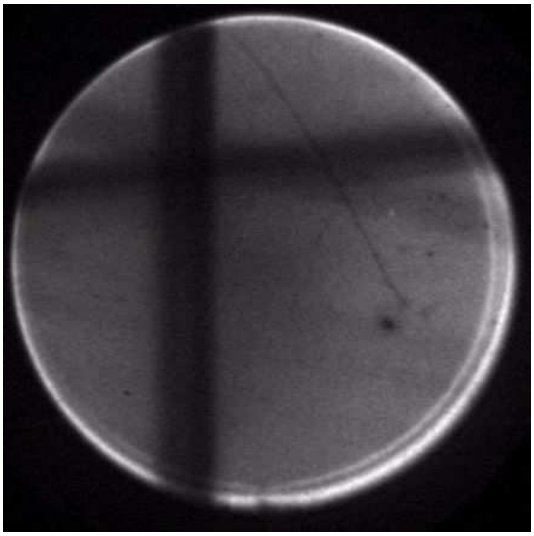

Figure 6.10: The phosphor screen under uniform illumination. The dark (burnt) region is the location of the undeflected atomic beam.

The horizontal tilting of the light beam was often accompanied by a vertical displacement, which made the deflection center position shift vertically on the phosphor screen, while the non-uniform phosphor screen sensitivity introduced errors in the force comparison. In Figure 6.10, an image of the phosphor screen under uniform illumination of the He* beam is shown. The image shows that the phosphor screen is extremely nonuniform. The dark regions on the screen are the burn marks of the high intensity beam flux from the slit. We have rotated the screen by 90° during the experiment. This accounts for the dark cross on the image. The MCP was actually rotated more than 90°, as indicated by the tilted lighter stripe on the upper part of the image. There were some bad points and scratches on the MCP which are also visible on the images. While doing the force mapping, we used the lower-right corner of the

MCP/PS detector.

A more severe problem was caused by the artifacts produced by the reflections of the two windows when the light beam was close to normal incidence. These windows were AR coated for 1083 nm, but the reflectivity was not low enough and we did see reflections from the windows. As shown in Figure 6.9(e) to 6.9(g), there was a dark stripe moving on the screen image from left to right as the light beam sweeps through the normal direction of the windows. We think this was due to optical interference between the reflections from the two windows. This dark stripe on the screen made accurate force measurement impossible for light beams nearly perpendicular to the windows. For the force mapping, we had tilted the light beam at -1° so that this dark stripe moved out of the way. However, this could compromise the force measurement. Furthermore, the optimization of circular polarization and the alignment of retro-reflection mirror varied from angle to angle; and the flight time was shorter for positive tilt angle due to the movement of the interaction region toward the phosphor screen. All in all, the optical force measured from Figure 6.9 can only be interpreted qualitatively.

The largest deflection in Figure 6.9 occurred in Figure 6.9(f), where $\theta_{tilt} = -0.2^\circ$ and the peak deflection is about 7.8 mm, corresponding to the optical force $F = 6.4F_{rad}$. The force is smaller for tilted beams. At $\theta_{tilt} = 2.8^\circ$, the peak deflection is 4.2 mm, corresponding to $F = 3.5F_{rad}$. A very rough estimate gives a force about half of the maximum value when the light beam is tilted by $\sim 3^\circ$. Taking the longitudinal velocity to be 1000 m/s, a tilt angle of 3° corresponds to transverse velocity of 50 m/s. Therefore the FWHM

velocity capture range of the ARP force is at least 100 m/s or $60\gamma/k$. It is much larger than the velocity capture range of the radiative force, which is about γ/k. However, it is smaller than the theoretically predicted value. The force calculation with optical Bloch equation in Figure 2.9 shows that the expected velocity capture range is about $200\gamma/k$ for ARP, which is more than 300 m/s. Except all the measurement errors discussed above, the factor of 3 reduction could be partially due to the extending tails of the optical pulse used in the experiment (see Figure 4.6). These tails induce overlaps between counter-propagating pulses, which consequently mess up the adiabaticity and reduce the velocity capture range of the force.

6.5 Conclusion

We experimentally observed the force associated with the periodic adiabatic rapid passage sequences induced by counter-propagating chirped light pulses. The maximum ARP force measured in the experiment is about $7.6F_{rad}$, where F_{rad} is the usual radiative force. The force is very robust against the variations of the peak Rabi frequency and the amplitude of the frequency chirp. The velocity capture range of the force is estimated to be more than 100 m/s, which is 60 times bigger than the velocity capture range of F_{rad}. However, the measured force is about 40% of the theoretic prediction, the velocity capture range is also smaller than the predicted value by a factor of 3. Except measurement errors, the reductions of the force and the velocity capture range are partly accounted for by the non-ideal pulses used in the experiment. Especially, the pulse length is about 3.6 ns with its tails included,

which is longer than the ~ 3.1 ns ideal pulse. This causes overlap between the counter-propagating pulses and affects the adiabatic processes. Another important factor which we have not included is the optical pumping effect among different magnetic sublevels of the 2^3S_1 and 2^3P_2 states of He*. It could be the main reason of the force reduction.

Moreover, we mapped out experimentally the distribution of the force with periodic counter-propagating chirped pulses in the parameter space of (δ_0, Ω_0), *e.g.* the amplitude of the chirping frequency and the peak Rabi frequency of the pulse. Even though the force amplitude is in general small, and the force in π-pulse region is even smaller ($\sim 20\%$), the measured force still shows a distribution qualitatively agreeing with the theoretical distribution of the force we have obtained in Chapter 2. This substantiates our theoretical analysis of the atomic evolution under periodic adiabatic rapid passage processes and the force modelling.

Appendix A

Nonadiabatic Transition in ARP

The ARP problem is basically a level crossing problem. As far as one-time population inversions is concerned, the sweep time can be regarded as infinite. Extensive research has been done in this area, which include the well known Landau-Zener formula [45, 46] and the Demkov-Kunike model [47, 48]. More discussions on these infinite time level crossing problem can be found in literature [39, 40, 41]. However, for repetitive sweeps the pulse length is finite, and the nonadiabatic transition probability has different properties, which are the subject of this appendix. This work is credited to Dr. Tianshi Lu.

A.1 Approximate Formula for P_{nad}

The Schödinger equation with Hamiltonian in Eq. (2.1) does not have an analytical solution for a generic light pulse. However, we have been able to obtain an approximate formula for the nonadiabatic transition probability using the technique of unitary integration in the rotating adiabatic frame (the precise meaning of the rotating adiabatic frame will be given below). Solutions

for finite time requires forms such as the Dyson expansion involving nested time integrations and time-ordered products [73, 74].

Consider light pulses of width T. Since we are mostly interested in symmetric pulses, it is convenient to assume that the pulses extend from $t = -T/2$ to $t = T/2$. In the concomitant rotating frame, both $\int_{-T/2}^{T/2} \Omega(t)dt$ or $\int_{-T/2}^{T/2} \delta(t)dt$ could be much larger than 1 so that the Dyson expansion converges too slowly to evaluate. To improve the convergence, we can switch the reference frame to the adiabatic frame [43, 44], *i.e.* the instantaneous eigenspace of the Hamiltonian - the frame spanned by the instantaneous dressed atom eigenstates. However, as we will see shortly, the Dyson expansion in the adiabatic frame still converges slowly. A second frame transformation was utilized to look at the problem in the adiabatic frame rotating with the instantaneous generalized Rabi frequency $\Omega'(t)$. The Hamiltonian then has magnitude of order $\hbar/T$ with rapidly changing phase and the Dyson expansion converges quickly. Berry has extended this idea by considering successive transformation through a series of superadiabatic basis to further reduce the magnitude of the Hamiltonian [75]. In our problems, we will show for typical pulses, the first integral term in the Dyson expansion in the rotating adiabatic frame is already a good approximation.

For a Hamiltonian system, if the states undergoes a unitary frame transformation, the transformation of the Hamiltonian can be derived from the Schödinger equation. Denote the Hamiltonian and states in the original frame by H_0 and ψ_0. If the state in the new reference frame is connected with the

state in the old reference frame by U, where U is a unitary transformation,

$$\psi_1 = U\psi_0, \tag{A.1}$$

the correspondent Hamiltonian in the new reference frame is:

$$H_1 = UH_0U^\dagger - i\hbar U\frac{d}{dt}U^\dagger. \tag{A.2}$$

Here we consider a sequence of two such transformations. The first transformation is composed of the instantaneous eigenvectors of the $H(t)$ in Eq. (2.1). Take $\theta(t) = \arctan(\Omega(t)/\delta(t))$, U1 can be written as

$$U_1(t) = \begin{pmatrix} \cos(\theta/2) & \sin(\theta/2) \\ -\sin(\theta/2) & \cos(\theta/2) \end{pmatrix}.$$

From Eq. (A.2), the new Hamiltonian is

$$H_1(t) = \frac{\hbar}{2}\begin{pmatrix} \Omega' & i\dot{\theta} \\ -i\dot{\theta} & -\Omega' \end{pmatrix},$$

where $\Omega' = \sqrt{\delta^2 + \Omega^2}$. This frame is the eigenspace of H(t) and is called the *adiabatic frame*. Although the off-diagonal elements of H_1 are small, its diagonal elements are still large and cause slow convergence of the Dyson expansion in the solution. A "rotating wave" transformation of angular frequency $\Omega'(t)$ removes the diagonal elements from H_1 and accelerate the convergence of the Dyson expansion. For the second frame transformation, the transformation

matrix is

$$U_2(t) = \begin{pmatrix} e^{is/2} & 0 \\ 0 & e^{-is/2} \end{pmatrix},$$

where $s(t) = \int_0^t \Omega'(\tau) d\tau$. The new Hamiltonian is

$$H_{ad}(t) = \frac{\hbar}{2} \begin{pmatrix} 0 & i\dot{\theta}(t) e^{is(t)} \\ -i\dot{\theta}(t) e^{-is(t)} & 0 \end{pmatrix}. \tag{A.3}$$

The new frame is the so called *rotating adiabatic frame*. The evolution operator matrix elements in this frame can be expressed in simpler Dyson expansions. The general evolution operator of a two level system can be written in SU(2) as below:

$$\psi_{ad}(t_f) = \begin{pmatrix} \alpha^* & \beta \\ -\beta^* & \alpha \end{pmatrix} \psi_{ad}(t_i),$$

then the Schödinger equation with Hamiltonian in Eq. (A.3) gives

$$\dot{\beta} = \frac{\dot{\theta}}{2} e^{is} \alpha \tag{A.4a}$$

$$\dot{\alpha} = -\frac{\dot{\theta}}{2} e^{-is} \beta. \tag{A.4b}$$

The formal solution of the Schödinger equation can be obtained by integrating

Eq. (A.4a) and (A.4b) by part and substituting into each other repeatedly,

$$\begin{aligned}\alpha = 1 &- \int_{t_i}^{t_f} dt_1 \int_{t_i}^{t_1} dt_2 \frac{\dot{\theta}(t_2)}{2} e^{is(t_2)} \frac{\dot{\theta}(t_1)}{2} e^{-is(t_1)} \\ &+ \int_{t_i}^{t_f} dt_1 \int_{t_i}^{t_1} dt_2 \int_{t_i}^{t_2} dt_3 \int_{t_i}^{t_3} dt_4 \frac{\dot{\theta}(t_4)}{2} e^{is(t_4)} \frac{\dot{\theta}(t_3)}{2} e^{-is(t_3)} \frac{\dot{\theta}(t_2)}{2} e^{is(t_2)} \frac{\dot{\theta}(t_1)}{2} e^{-is(t_1)} \\ &+ \ldots \end{aligned} \tag{A.5a}$$

$$\begin{aligned}\beta = &\int_{t_i}^{t_f} dt_1 \frac{\dot{\theta}(t_1)}{2} e^{is(t_1)} \\ &- \int_{t_i}^{t_f} dt_1 \int_{t_i}^{t_1} dt_2 \int_{t_i}^{t_2} dt_3 \frac{\dot{\theta}(t_3)}{2} e^{is(t_3)} \frac{\dot{\theta}(t_2)}{2} e^{-is(t_2)} \frac{\dot{\theta}(t_1)}{2} e^{is(t_1)} \\ &+ \ldots \end{aligned} \tag{A.5b}$$

Both series converge absolutely since it can be shown from Eq. (A.5) that

$$|\alpha| + |\beta| \leq \exp\left(\int_{t_i}^{t_f} |\frac{\dot{\theta}(t)}{2}| dt\right).$$

Keeping only the first integral term in the Dyson expansion,

$$\psi_{ad}(t) = \begin{pmatrix} 1 & \frac{1}{2}\int_{-T/2}^{t} \dot{\theta} e^{is} d\tau \\ -\frac{1}{2}\int_{-T/2}^{t} \dot{\theta} e^{-is} d\tau & 1 \end{pmatrix} \psi_{ad}(-\frac{T}{2}). \tag{A.6}$$

A problem with the evolution operator in Eq. (A.6) is that it is not a unitary transformation. According to the theory of unitary integration (see [73] and the references therein), the non-unitarity of the transformation not only violates the principles of quantum mechanics, but also leads to numerical in-

stability. We know a generic transformation in SU(2) has the form

$$\psi_{ad}(t) = \begin{pmatrix} e^{i\alpha_1}\cos\alpha_2 & e^{i\alpha_3}\sin\alpha_2 \\ -e^{-i\alpha_3}\sin\alpha_2 & e^{-i\alpha_1}\cos\alpha_2 \end{pmatrix} \psi_{ad}(-\frac{T}{2}). \tag{A.7}$$

By comparing Eq. (A.6) and (A.7), we obtained the first order approximation for α_1, α_2 and α_3 as follows,

$$\begin{aligned} \alpha_1 &= 0 \\ \alpha_2 &= |\beta| \\ \alpha_3 &= \arg(\beta), \end{aligned}$$

where

$$\beta(t) = \frac{1}{2}\int_{-T/2}^{t} \dot{\theta} e^{is} d\tau.$$

Thus after unitarization, Eq. (A.6) becomes

$$\psi_{ad}(t) = \begin{pmatrix} \cos|\beta| & \beta\frac{\sin|\beta|}{|\beta|} \\ -\beta^*\frac{\sin|\beta|}{|\beta|} & \cos|\beta| \end{pmatrix} \psi_{ad}(-\frac{T}{2}). \tag{A.8}$$

Eq. (A.8) clearly converges to Eq. (A.6) in the adiabatic limit where $\beta \to 0$. It is also exact in the limit that $\Omega \to 0$ or $\delta \to 0$.

For a generic pulse of duration T, an approximation of the nonadiabatic transition probability P_{nad} can be derived from Eq. (A.8). In the case that the pulse intensity vanishes at the beginning and the end of the sweep, P_{nad} is equal to the probability of the atom state starting from one of the eigenstate

while ending in the eigenstate on the different branch at the end of the pulse. From Eq. (A.8), it can be shown that

$$P_{nad} \doteq \sin^2 |\beta(\frac{T}{2})| = \sin^2 |\frac{1}{2}\int_{-T/2}^{T/2} \dot{\theta} e^{is} dt|. \tag{A.9}$$

For symmetric pulses, *i.e.*

$$\begin{aligned} \delta(-t) &= -\delta(t) \\ \Omega(-t) &= \Omega(t), \end{aligned} \tag{A.10}$$

Eq. (A.9) can be improved by making use of the symmetry and applying successively the unitary integration of Eq. (A.8) for each half pulse (with conjugate β due to the symmetry). P_{nad} is found to be

$$P_{nad} \doteq (\Re(z)\frac{\sin|z|}{|z|})^2, \tag{A.11}$$

where

$$z = 2\beta(0) = \int_{-T/2}^{0} dt\dot{\theta}(t)\exp(i\int_{0}^{t} d\tau\Omega(\tau)).$$

Though both are of first order accuracy, Eq. (A.11) is more accurate than Eq. (A.9) since Eq. (A.11) is obtained by two successive unitary transformations for each half pulse, while Eq. (A.9) is by a single unitary transformation for the entire pulse.

To derive higher order corrections, more terms in the Dyson expansion need to be retained, which involve more nested time integrations and are

expensive to evaluate. One of the key findings in this work is that the main characters of the distribution of P_{nad} over the pulse parameter space are already captured by the first order perturbation in the rotating adiabatic frame. More details will be given in Section A.2.

From Eq. (A.11) we also derived the approximate formula for the zeros of P_{nad}, where the nonadiabatic transition probability vanishes and thus the perfect inversion. The condition is $\Re(z) = 0$, or equivalently,

$$\int_{-T/2}^{T/2} \dot{\theta} e^{is} dt = 0. \tag{A.12}$$

Eq. (A.11) and (A.12) are for a generic symmetric pulse with vanishing amplitude at the beginning and the end. They will be validated by comparison with analytical and numerical integration of Eq. (2.1) for two classes of pulses in the next section. If the pulse amplitude does not vanish, e.g. a square pulse, the calculation of P_{nad} over a finite period requires more work due to the unmatched dressed atom eigenstates to the diabatic states at two ends of the pulse. To find P_{nad} in the adiabatic frame we need to map the diabatic state into the adiabatic frame at the beginning and map back to the diabatic states at the end. An approximate formula of more complicated form for P_{nad} can be derived but is omitted here.

A.2 P_{nad} for Various Pulses

In this section we calculate the P_{nad} for three classes of finite time pulses as sketched in Figure A.1(a)-(c). The first two classes can be solved analytically

while the last one can only be integrated numerically. The calculated P_{nad} will be compared to the result obtained by the approximation formulas.

Figure A.1(a) shows the time dependence of the Rabi frequency and the detuning of a linearly-chirped square pulse. Except from being a finite time light field, it is identical to the Landau-Zener case. Figure A.1(b) stands for a linear-chirped triangular pulse, while Figure A.1(c) shows a cosinusoidally-chirped sinusoidal pulse. These two types are preferable for ARP since the light vanishes at the beginning and the end of the pulse so that the diabatic states match the initial dressed atom eigenstates states and can then allow adiabatical following as shown in Figure 2.2. Experimentally, sinusoidal chirping is most feasible, while the pulse shape can vary from triangular to sinusoidal. In Figure A.1(d), an infinite-time Demkov-Kunike pulse is sketched. The Landau-Zener model and the Demkov-Kunike will be discussed in Section A.3, whose transition probability will also be compared to that of the finite-time cases.

Consider the Schödinger equation for a two-level atom in a time-dependent field

$$i\hbar\frac{\mathrm{d}}{\mathrm{d}t}\begin{pmatrix}\psi_+\\ \psi_-\end{pmatrix} = H\psi = \frac{\hbar}{2}\begin{pmatrix}\delta(t) & \Omega(t)\\ \Omega(t) & -\delta(t)\end{pmatrix}\begin{pmatrix}\psi_+\\ \psi_-\end{pmatrix}. \tag{A.13}$$

For linearly-chirped square pulse

$$\begin{aligned}\Omega(t) &= \Omega_0\\ \delta(t) &= 2\delta_0 t/T,\end{aligned} \tag{A.14}$$

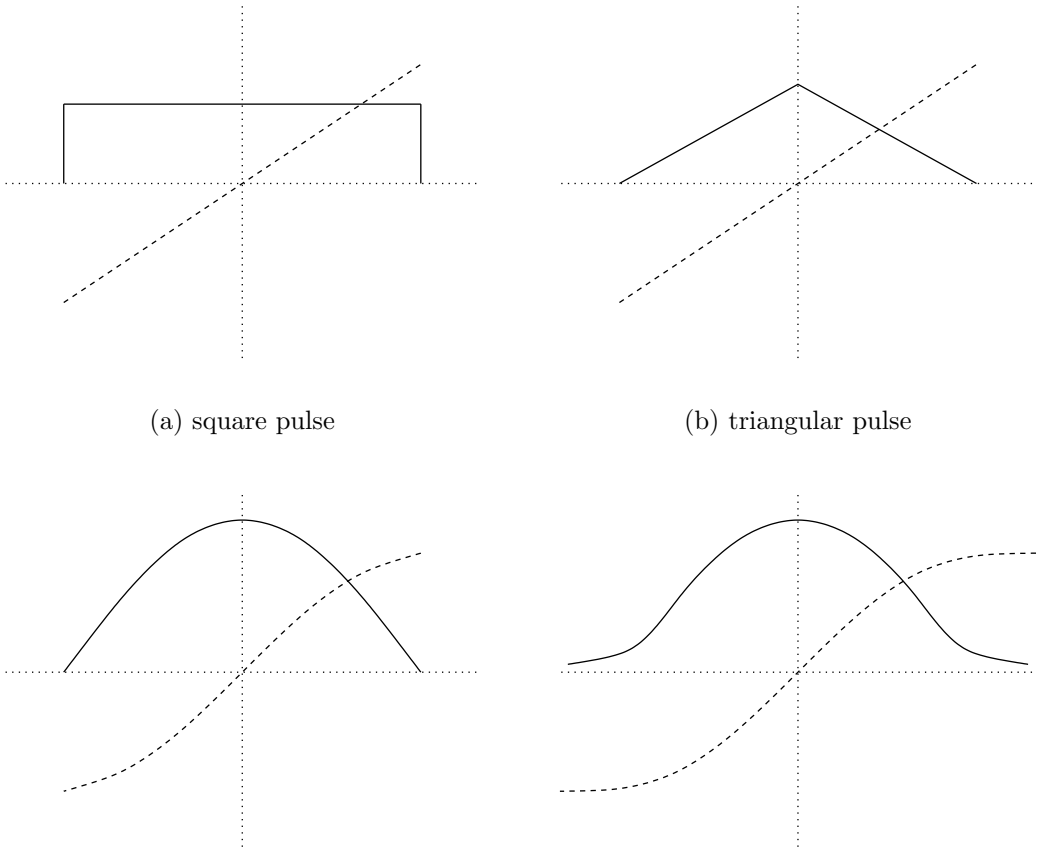

(a) square pulse

(b) triangular pulse

(c) sinusoidal pulse

(d) Demkov-Kunike

Figure A.1: Four classes of chirped pulses. Solid curves stand for $\Omega(t)$, dashed curves stand for $\delta(t)$. The first three are finite-time pulses, the last one is for infinite time. (a) Linearly chirped square pulse (b) Linearly chirped triangular pulse, (c)Cosinusoidally chirped sinusoidal pulse. (d) The Demkov-Kunike model whose definition is given in Eq. (A.19).

where $t \in [-\frac{T}{2},\ \frac{T}{2}]$. Eq. (A.13) has the solution in terms of confluent hypergeometric functions, namely,

$$\begin{aligned}\psi_+(t) &= e^{-i\frac{\delta_0}{2T}t^2} F\left(i\frac{\Omega_0^2 T}{16\delta_0}; \frac{1}{2}; i\frac{\delta_0}{T}t^2\right)\psi_+(0) \\ &- i\frac{\Omega_0}{2} t e^{-i\frac{\delta_0}{2T}t^2} F\left(i\frac{\Omega_0^2 T}{16\delta_0} + \frac{1}{2}; \frac{3}{2}; i\frac{\delta_0}{T}t^2\right)\psi_-(0). \qquad \text{(A.15)}\end{aligned}$$

The nonadiabatic transition probability over the pulse for $t = -T/2 \to T/2$ is given by

$$P_{nad} = \left[\left|F\left(i\frac{\Omega_0^2 T}{16\delta_0}; \frac{1}{2}; i\frac{\delta_0 T}{4}\right)\right|^2 - (\frac{\Omega_0 T}{4})^2 \left|F\left(i\frac{\Omega_0^2 T}{16\delta_0} + \frac{1}{2}; \frac{3}{2}; i\frac{\delta_0 T}{4}\right)\right|^2\right]^2.$$

The formula shows that P_{nad} is a function of two dimensionless quantities $\delta_0 T$ and $\Omega_0 T$. If we let $T \to \infty$ with Ω_0 and δ_0/T fixed, the asymptotic form of hypergeometric functions gives

$$\lim_{T\to\infty} P_{nad} = \exp(-\frac{\pi}{4}\frac{\Omega_0^2 T}{\delta_0}),$$

which is exactly the Landau-Zener formula [45]. A contour plot of P_{nad} calculated by the analytical formula is plotted in the $\delta_0 - \Omega_0$ parameter space in Figure A.2(a). The coordinates are scaled by $T/2$. Since the light has constant intensity, it is an example of non-vanishing light fields as discussed in the last paragraph of Section A.1. The approximate P_{nad} obtained in the way described in that paragraph is plotted in Figure A.2(b), which matches well with Figure A.2(a).

For a linearly-chirped triangular pulse, the time-dependence of the inten-

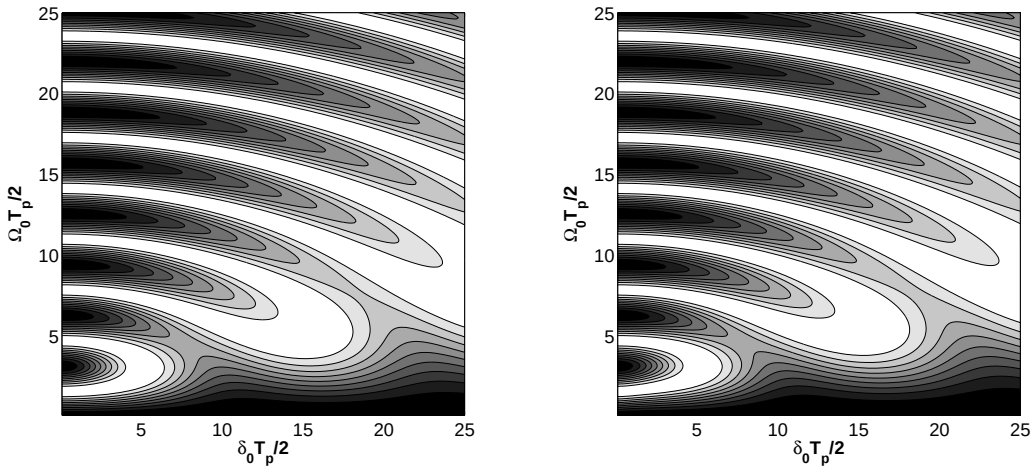

(a) square pulse, analytic

(b) square pulse, approx.

Figure A.2: Nonadiabatic transition probability P_{nad} vs δ_0 and Ω_0 for square pulse. The coordinates are normalized using area theorem. The contour curves are for $P_{nad} = 0.1, 0.2, ..., 0.9$. The white regions stand for $P_{nad} < 0.1$.

sity and the frequency sweep is

$$\begin{aligned}\Omega(t) &= \Omega_0(1-|2t/T|) = 2A\sin\varphi(1-|2t/T|)\\ \delta(t) &= \delta_0(2t/T) = 2A\cos\varphi(2t/T),\end{aligned}$$

where $A = \sqrt{\Omega_0^2+\delta_0^2}$, $\tan\varphi = \Omega_0/\delta_0$, $t \in [-\frac{T}{2}, \frac{T}{2}]$. Eq. (A.13) can be solved for each half pulse. In the Bloch sphere view of the problem, the torque vector moves along a straight line with uniform speed for each half pulse. In a properly rotated frame, the torque vector reduces to the case of linearly-chirped square pulse. We omit the straightforward yet tedious derivation and list here the result for the nonadiabatic transition probability,

$$P_{nad} = [(\Re\alpha)^2 - (\Re\beta)^2 + \cos 2\varphi((\Im\alpha)^2 - (\Im\beta)^2) + 2\sin 2\varphi \Im\alpha\Im\beta]^2, \quad \text{(A.16)}$$

where

$$\begin{aligned}\alpha &= e^{-i\frac{AT^2}{8}\cos 2\varphi}[F(i\kappa,\frac{1}{2},i\frac{aT^2}{4}\cos^4\varphi)\bar{F}(i\kappa,\frac{1}{2},i\frac{aT^2}{4}\sin^4\varphi) - \\ &\quad \frac{(AT)^2}{64}\sin^4 2\varphi F(i\kappa+\frac{1}{2},\frac{3}{2},i\frac{aT^2}{4}\cos^4\varphi)\bar{F}(i\kappa+\frac{1}{2},\frac{3}{2},i\frac{aT^2}{4}\sin^4\varphi)],\\ \beta &= -ie^{-i\frac{AT^2}{8}(\cos^4\varphi+\sin^4\varphi)}\frac{AT}{4}\sin 2\varphi\cdot\\ &\quad [\cos^2\varphi F(i\kappa,\frac{1}{2},i\frac{aT^2}{4}\sin^4\varphi)F(i\kappa+\frac{1}{2},\frac{3}{2},i\frac{aT^2}{4}\cos^4\varphi)\\ &\quad +\sin^2\varphi F(i\kappa,\frac{1}{2},i\frac{aT^2}{4}\cos^4\varphi)F(i\kappa+\frac{1}{2},\frac{3}{2},i\frac{aT^2}{4}\sin^4\varphi)],\end{aligned}$$

in which

$$\kappa = \frac{AT^2}{64}\sin^2 2\varphi.$$

The contour of P_{nad} in the $\delta_0 - \Omega_0$ parameter space is plotted in Figure A.3(a). The scaling factor of the coordinates is chosen to be $T/4$. The approximation value for linearly-chirped triangular pulses is calculated by Eq. (A.11) and plotted in Figure A.3(b) for comparison.

The time-dependence of the intensity and the frequency sweep for sinusoidal pulses is described by Eq. (2.4). The resulting equation is similar to the Mathieu equation. No analytical solution of known type has been derived for Eq. (A.13) except for the special case of $\Omega_0 = \delta_0$, which has been studied in [42]. Numerical calculation of P_{nad} has been done by integrating the optical Bloch equation and to $T/2$ and calculating the remaining ground state population as described in Section 2.2. P_{nad} obtained by the numerical integration and the value calculated by the approximation formula Eq. (A.11) are contoured in Figure A.3(c) and Figure A.3(d) for comparison. The contour plots match very well.

Different scaling factors are chosen for three schemes according to the area integration of the pulse so that we can easily compare among the plots. As mentioned in the beginning of this section, the white region in the figures, which stands for diminishingly small P_{nad}, is larger in Figure A.3(a) and Figure A.3(c) than in Figure A.2(a).

Finally, to demonstrate the accuracy of Eq. (A.12) in locating zeros of P_{nad}, the P_{nad} for triangular (analytical) and sinusoidal (numerical) pulses have been plotted in logarithm scale in Figure A.4(a) and Figure A.4(c) along with their approximation in Figure A.4(b) and Figure A.4(d). For both types of pulses, zeros of P_{nad} indicated by the darkest regions in the corresponding

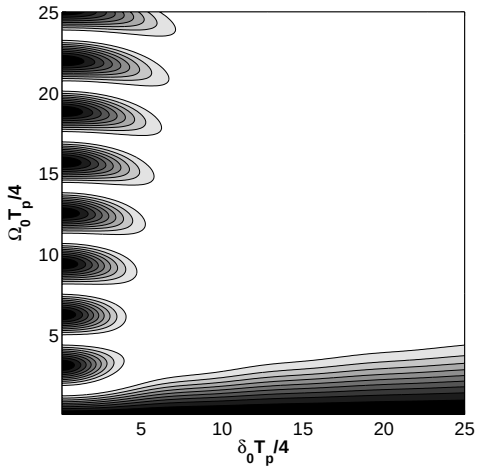

(a) triangular pulse, analytic

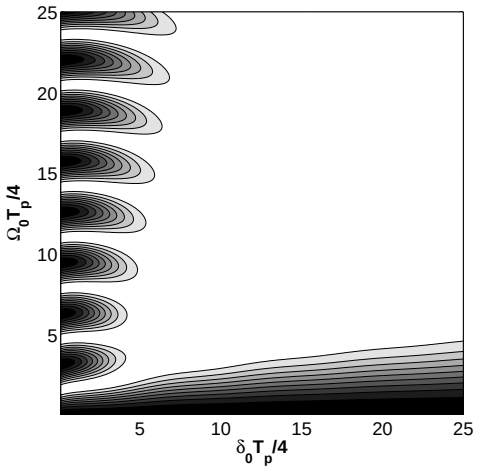

(b) triangular pulse, approx.

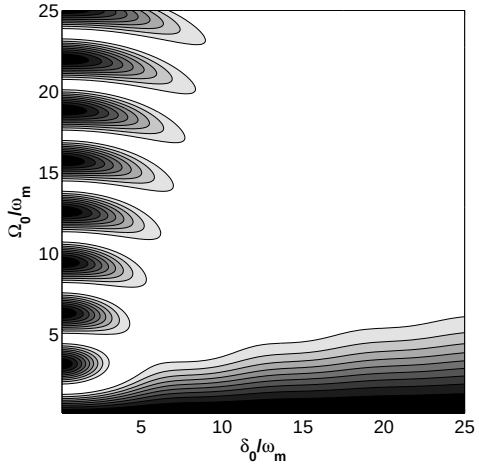

(c) sinusoidal pulse, numerical

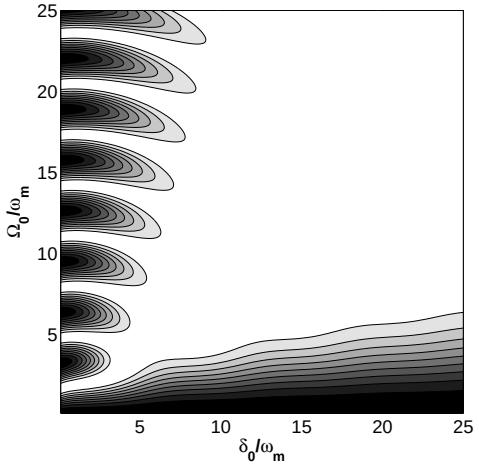

(d) sinusoidal pulse, approx.

Figure A.3: Nonadiabatic transition probability P_{nad} vs δ_0 and Ω_0 for triangular and sinusoidal pulses. The coordinates are normalized using area theorem. The contour curves are for $P_{nad} = 0.1, 0.2, ..., 0.9$. The white regions stand for $P_{nad} < 0.1$.

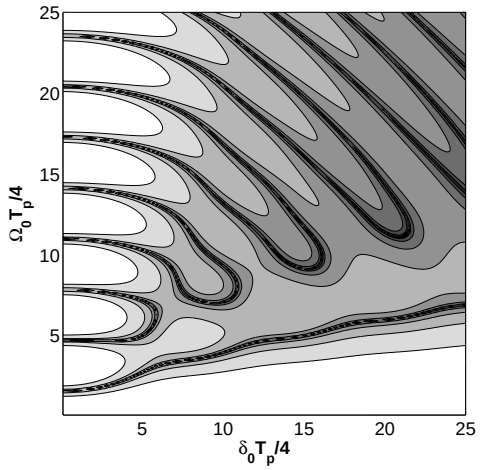

(a) triangular pulse, analytic

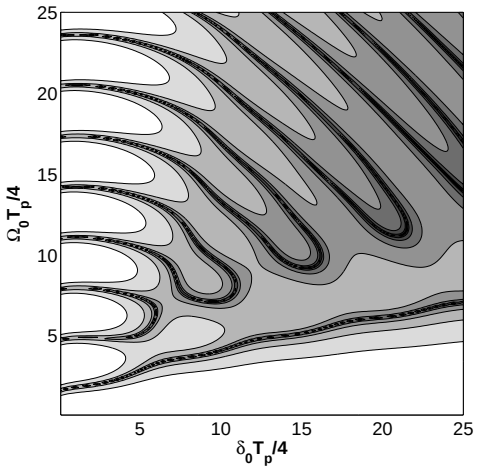

(b) triangular pulse, approx.

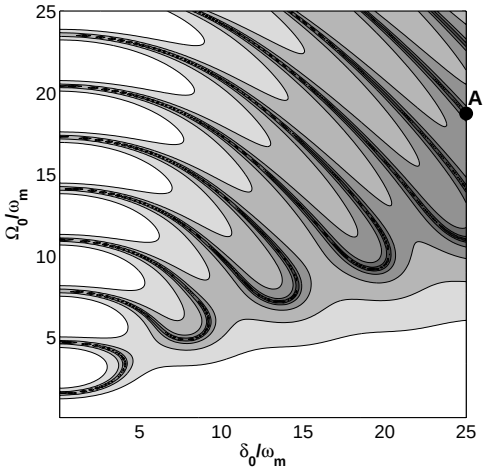

(c) sinusoidal pulse, numerical

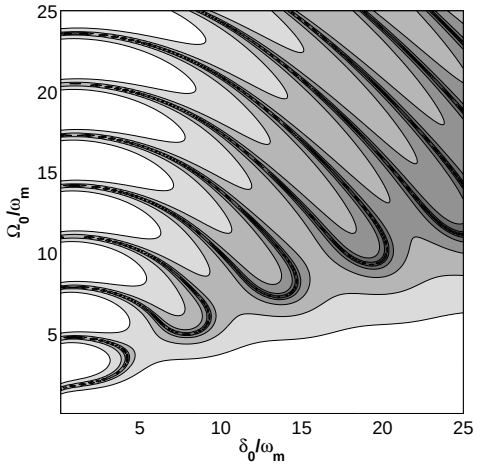

(d) sinusoidal pulse, approx.

Figure A.4: Contour maps of P_{nad} in logarithm scale for triangular and sinusoidal pulses. The contour curves are for $P_{nad} = 0.1, 0.01, ...$ The darkest regions represent zeros of P_{nad}. The point A with coordinates [25.0,18.724] in (c) corresponds to the trace of Bloch vector shown in Figure 2.2.

pair of figures agree very well. The detailed information carried by Figure A.2 and Figure A.4 will be discussed further in the next two sections.

A.3 Landau-Zener and Demkov-Kunike Models

In this section we compare P_{nad} for finite time pulses with the Landau-Zener (LZ) formula and the nonadiabatic transition probability in the Demkov-Kunike (DK) model [47, 48]. Both the LZ model and the DK model are for infinite-time transitions.

The Landau-Zener case has the same time dependent field as Eq. (A.14) and as shown in Figure A.1(a) except that the pulse duration goes to infinite. The nonadiabatic transition probability is given by the Landau-Zener formula

$$P_{LZ} = \exp(-\frac{\pi}{2}\frac{\Omega^2}{d\delta/dt}). \tag{A.17}$$

To apply the LZ formula to a generic finite-time pulse with an avoided crossing at resonance, the index should be evaluated at the resonance. It is a valid approximation for P_{nad} if and only if the nonadiabatic transition is dominated at the avoided crossing. In other words, Eq. (A.17) is valid if $\delta_0 \gg \Omega_0$ (δ_0 and Ω_0 are the maximum detuning and Rabi frequency) so that the nonadiabatic transition away from the resonance is negligible, and the index in Eq. (A.17) is bounded so that P_{LZ} is not too small to be dominant over by the off-resonance contribution. Thus the criterion for $P_{nad} \approx P_{LZ}$ for a finite-time pulse can be

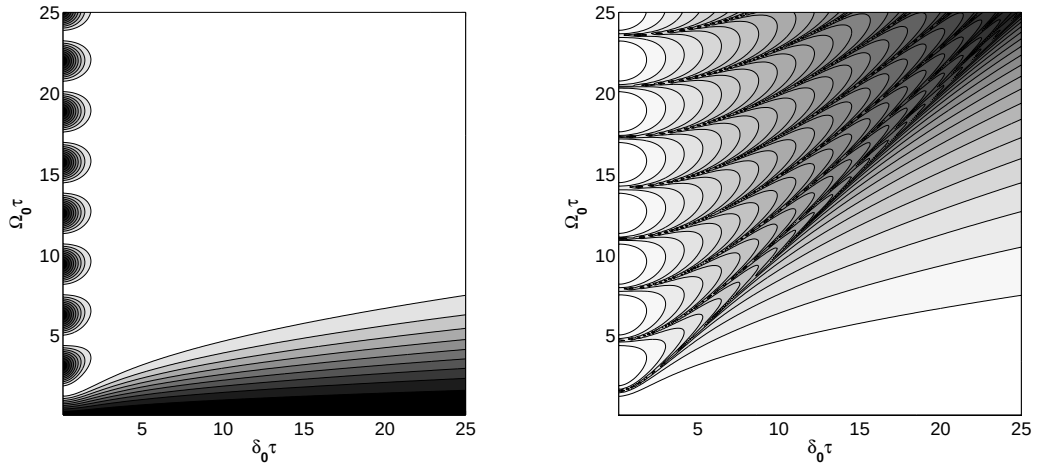

(a) linear scale

(b) logarithm scale

Figure A.5: P_{nad} for Demkov-Kunike model. The formula is Eq. (A.20). The contour curves in (a) are for $P_{nad} = 0.1, 0.2, ..., 0.9$, the white regions stand for $P_{nad} < 0.1$. The contour curves in (b) are for $P_{nad} = 0.1, 0.01, ...$ The darkest regions represent zeros of P_{nad}.

written in the following dimensionless form,

$$\begin{aligned} \delta_0/\Omega_0 \quad &\gg 1 \\ \Omega_0^2 T/\delta_0 \quad &finite \quad . \end{aligned} \tag{A.18}$$

The Demkov-Kunike model has a pulse-shaped intensity profile. The time dependence of the field is

$$\begin{aligned} \Omega(t) &= \Omega_0 \mathrm{sech}(\frac{\pi t}{2\tau}) \\ \delta(t) &= \delta_0 \tanh(\frac{\pi t}{2\tau}). \end{aligned} \tag{A.19}$$

The profile of $\Omega(t)$ and $\delta(t)$ is sketched in Figure A.1(d), which looks similar to the chirped pulse in Figure A.1(c). A special case of the DK model ($\tau^2(\Omega_0^2 - \delta_0^2) = \pi^2/4$) was studied in Ref. [7]. The nonadiabatic transition probability of the DK model was given analytically in [48],

$$P_{nad} = \frac{\cosh^2 \tau\sqrt{\delta_0^2 - \Omega_0^2}}{\cosh^2 \tau\delta_0}. \tag{A.20}$$

The contour of P_{nad} is plotted in Figure A.5(a) (linear scale) and Figure A.5(b) (logarithm scale). similar as the contour plot for the finite time pulse, it also shows oscillations along the y-axis. It was pointed out by Suominen *et. al.* [48] that each oscillation is connected to an integer number of precessions of the Bloch vector during the time evolution. The oscillations of P_{nad} for finite-time pulses can be explained in the similar fashion. For example, Figure 2.2 shows the trace of Bloch vector under the influence of a sinusoidal light pulse at point A in Figure A.4(c) with parameters $(\delta_0, \vec{\Omega}_0) = (25.0, 18.724)$. Point A in Figure A.4(c) lies on the 11th curve counted from the origin along the diagonal. Correspondingly, Figure 2.2(b) shows that in the adiabatic frame, the Bloch vector precesses exactly 11 cycles while the torque vector is fixed at point O. In the case of the finite time sinusoidal pulses, these curves pairs. Along each "loop" of zero locus in ARP maps such as in Figure A.4, there is a special point connecting the upper arc and lower arc, whose precession number differs by one.

The regime where the Landau-Zener formula is valid for the DK model is larger. As shown in [48], the LZ formula is valid for the DK model when

$\Omega_0 \ll \delta_0$ and $\delta_0 \tau \gg 1$. This criterion is weaker than that for finite-time pulses in Eq. (A.18). As a result, we can see that the LZ formula is valid under a parabola-like curve in Figure A.4, while in Figure A.5(b) it is qualitatively correct in the entire region under the diagonal.

A.4 Asymptotic Forms of P_{nad}

For pulses of finite duration, P_{nad} has different asymptotic forms in different regimes of the $\delta_0 - \Omega_0$ space. First, it has been shown that the regime where Landau-Zener formula holds for a generic pulse is

$$\delta_0 \gg \Omega_0,\ \Omega_0^2 T/\delta_0\ finite. \tag{A.21}$$

In the $\delta_0 - \Omega_0$ parameter space such as in Figure A.4, the Landau-Zener regime is the bottom-right corner. The asymptotic form of P_{nad} in this regime is

$$P_{nad} \sim \exp(-\frac{\pi}{2} A_0) \equiv \exp(-\frac{\pi}{2} \frac{\Omega_0^2}{(\frac{\mathrm{d}\delta}{\mathrm{d}t})_{\delta=0}}),$$

where A_0 measures the adiabaticity at resonance.

On the contrary, if

$$\Omega_0 \gg \delta_0,\ \delta_0^2 T/\Omega_0\ finite, \tag{A.22}$$

the coupling is dominant. It can be shown that for generic symmetric pulses,

$$P_{nad} \sim P_A(A_1) \cos^2[\frac{1}{2} \int_{-T/2}^{T/2} \Omega(t) dt + \frac{A_1}{4} \ln(\Omega_0 T) + \phi(A_1)], \tag{A.23}$$

where

$$A_1 \equiv \frac{\delta_0^2}{(\frac{\mathrm{d}\Omega}{\mathrm{d}t})_{\Omega=0}}$$

measures the adiabaticity at two ends of the pulse. Unlike the simple universal form in the Landau-Zener formula, $P_A(A_1)$ and $\phi(A_1)$ are functions that depend on the pulse shape and detuning. Their asymptotic values as $A_1 \to 0$ are

$$\begin{aligned} \phi(A_1) &\to 0 \\ P_A(A_1) &\sim 1 - \frac{\pi}{4} A_1. \end{aligned}$$

In the limit case that $A_1 = 0$, *i.e.* no detuning,

$$P_{nad} = \cos^2(\frac{1}{2}\int_{-T/2}^{T/2} \Omega(t)dt). \tag{A.24}$$

It agrees with the area theorem [7]. Therefore Eq. (A.23) is an extension of the area theorem. In the $\delta_0 - \Omega_0$ parameter space, the regime where Eq. (A.23) applies is the top-left corner.

Lastly, we discuss the regime unique to the finite-time transition. In the adiabatic limit,

$$\Omega_0 T \gg 1,\ \delta_0/\Omega_0\ finite,$$

the Rabi frequency and the detuning are of the same order. The rotating adiabatic frame is most convenient. From Eq. (A.9) we derived the following

asymptotic form of P_{nad} for generic symmetric pulses,

$$\begin{aligned} P_{nad} &\sim \sin^2|\frac{1}{2}\int_{-T/2}^{T/2}\dot{\theta}e^{is}dt| \sim |\frac{1}{2}\int_{-T/2}^{T/2}\dot{\theta}e^{is}dt|^2 \sim [\frac{\dot{\theta}\sin s}{2\Omega'}|_{-T/2}^{T/2}]^2 \\ &= [\frac{(\frac{\mathrm{d}\Omega}{\mathrm{d}t})_{\Omega=0}}{\delta_0^2}\sin(\int_0^{T/2}\Omega'(t)dt)]^2 \\ &= A_1^{-2}\cdot\sin^2(\frac{1}{2}\int_{-T/2}^{T/2}\Omega'(t)dt). \end{aligned} \tag{A.25}$$

Asymptotically P_{nad} oscillates with amplitude A_1^{-2} in this region. Comparison between Eq. (A.25) with Eq. (A.24) shows that there is an $\pi/2$ phase difference between two regimes. In the $\delta_0 - \Omega_0$ parameter space, the regime of adiabatic limit is in the top-right corner.

To summarize this appendix, by transformation to the rotating adiabatic frame and application of the unitary integration technique, an approximate formula has been obtained for the finite-time ARP process in the entire parameter space for generic symmetric pulses. The approximation agrees with the analytical solutions for linearly-chirped pulses and numerical solutions for sinusoidal pulses obtained from simulation of Schödinger equation. The probability has also been compared to Landau-Zener formula and the analytically solvable Demkov-Kunike model. The asymptotic forms of the nonadiabatic transition probability have been derived for the Landau-Zener regime, the "π-pulse" regime (where the area theorem applies) and the adiabatic limit regime respectively.

Appendix B

Force of Periodic ARP Sequence

A geometric method on the Bloch Sphere picture was developed for modelling the average force on the atomic beam by periodic ARP pulses train. This work presented here is credited to Dr. Tianshi Lu.

B.1 Force of Symmetric Light Pulses

The hamiltonian of an atom in a train of light pulses as shown in Figure 2.6(a) is give by Eq. (2.12). Making use of Eq. (A.2), with a frame transformation

$$U_{\pm}(t) = \begin{pmatrix} e^{\mp\frac{i}{2}kx} & 0 \\ 0 & e^{\pm\frac{i}{2}kx} \end{pmatrix}, \tag{B.1}$$

the Hamiltonian in the new frame becomes

$$H_1(t) = UH_0(t,x)U^{\dagger} = \frac{\hbar}{2}\begin{pmatrix} 0 & \Omega_{\pm}e^{-i\phi_{\pm}} \\ \Omega_{\pm}^{*}e^{i\phi_{\pm}} & 0 \end{pmatrix}, \tag{B.2}$$

which is independent of kx.

Denote the rotation of the Bloch sphere associated with each pulse by $R(\boldsymbol{\theta}_\pm)$, where the notation $R(\boldsymbol{\theta})$ stands for the rotation of angle $|\boldsymbol{\theta}|$ around $\boldsymbol{\theta}$. For an atom in the ground state at $t = 0$, which corresponds to the south pole on Bloch sphere, the Bloch vector rotates by $R(\boldsymbol{\theta}_+)$ with the first pulse followed by $R(\boldsymbol{\theta}_-)$ with the second pulse, then the evolution repeats again and again. For each kx, the force $F(kx)$ need to be averaged over many pulses (about the lifetime of the excited state), while the force of each pulse is given by Eq. (2.10). In the case of $\omega_m \gg \gamma$,

$$\begin{aligned} F &= \lim_{n\to\infty} \frac{\hbar k}{2nT}((\vec{R}_1^R - \vec{R}_0) - (\vec{R}_1^L - \vec{R}_1^R) + ... + (\vec{R}_n^R - \vec{R}_{n-1}^L) - (\vec{R}_n^L - \vec{R}_n^R))_3 \\ &= \lim_{n\to\infty} \frac{\hbar k}{2nT}(2\sum_{k=1}^{n}(\vec{R}_k^R)_3 - 2\sum_{k=1}^{n}(\vec{R}_k^L)_3) = \frac{\hbar k}{T}((\overline{\vec{R}_k^R})_3 - (\overline{\vec{R}_k^L})_3), \end{aligned} \tag{B.3}$$

where $\vec{R}_k^R$ ($\vec{R}_k^L$) is the Bloch vector after the k'th right (left) propagating pulse. The periodicity of the pulses implies that $\vec{R}_k^L$'s form a circle passing through the south pole, and $\vec{R}_k^R$'s form another circle passing through the north pole, as visualized in Figure B.1. $\overline{\vec{R}_k^R}$ and $\overline{\vec{R}_k^L}$ are the centers of the two circles indicated by the black dots in Figure B.1.

Denote the rotation for $kx = 0$ by $\boldsymbol{\theta}_\pm^0$. For $kx \neq 0$, Eq. (B.1) corresponds to a rotation of angle $\mp kx$ around the z-axis on the Bloch sphere. Since $H_0(t) = U^\dagger H_1(t, x)U$, the rotation angle $\boldsymbol{\theta}_\pm(kx)$ associated with H_0 differs from $\boldsymbol{\theta}_\pm^0$ in the azimuthal angle by $\mp kx$. The relative azimuthal angle between $\boldsymbol{\theta}_+$ and $\boldsymbol{\theta}_-$ is changed by $2kx$ from that between $\boldsymbol{\theta}_+^0$ and $\boldsymbol{\theta}_-^0$, therefore the average over kx is equivalent to the average over the relative azimuthal angle between $\boldsymbol{\theta}_+$ and $\boldsymbol{\theta}_-$, which implies that the net force depends only on $|\boldsymbol{\theta}_\pm|$ and

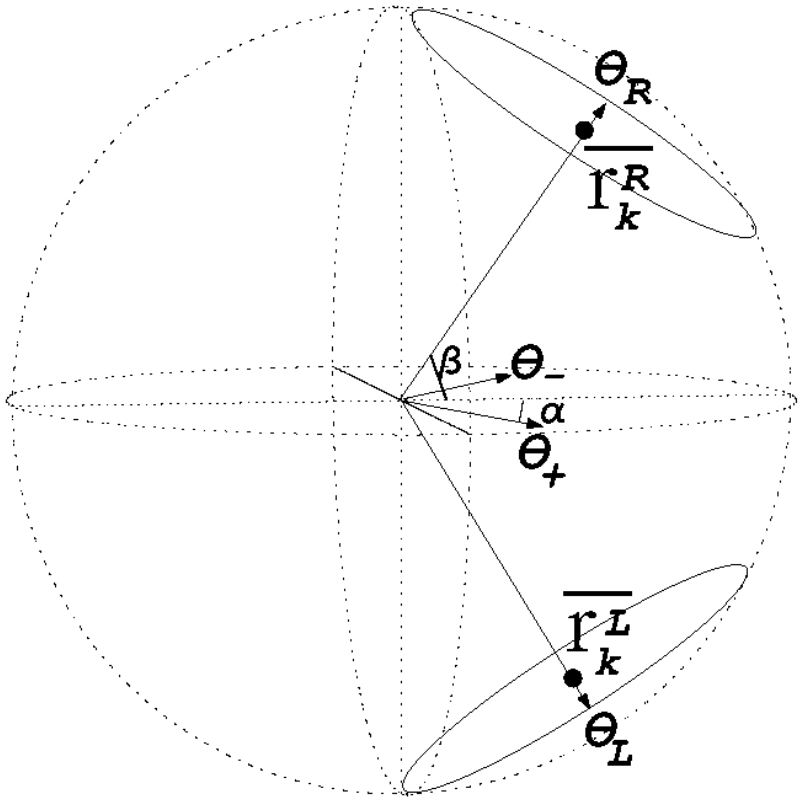

Figure B.1: Rotation of the Bloch vector on the Bloch sphere with periodic chirped pulse train.

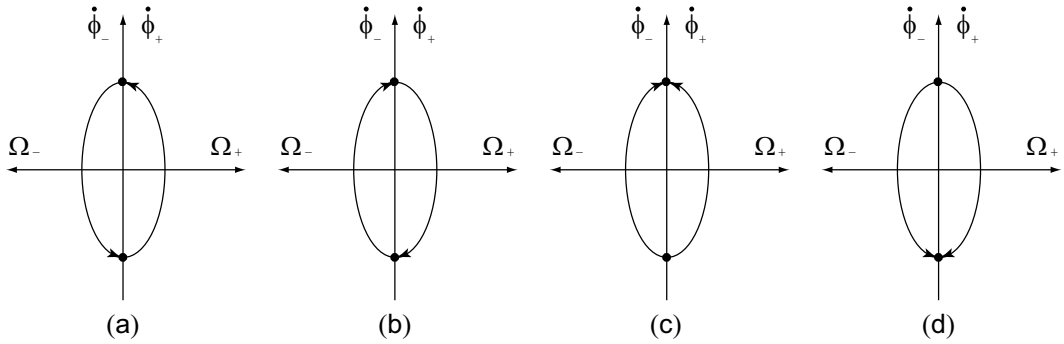

Figure B.2: Variation of torque vectors for various chirping direction of the symmetric left- and right- propagating light pulses. The sign or phase of $\Omega_\pm$ is immaterial. (a) Chirping upwards and then downwards. (b) Chirping downwards and then upwards. (a) Both chirping upwards. (a) Both chirping downwards.

their inclination angles.

Next we will calculate the average force of a sequence of symmetric pulses in the sense of Eq. (A.10). The chirping direction of the counter-propagating light pulses may have four different combinations, as shown in Figure B.2. Due to the average over the relative azimuthal angle between $\boldsymbol{\theta}_\pm$, the sign or phase of the Rabi frequency $\Omega_\pm$ doesn't affect the average force. All cases in Figure B.2 have the same average force on rest atoms since their $\boldsymbol{\theta}_\pm$ have the same amplitude and inclination angle. Furthermore, the symmetry of pulses indicates that $\boldsymbol{\theta}_\pm$ are in the equatorial plane on Bloch sphere and $|\boldsymbol{\theta}_+| = |\boldsymbol{\theta}_-|$. What remains is a mathematical exercise.

Define

$$R(\boldsymbol{\theta}_R) = R(\boldsymbol{\theta}_+) \cdot R(\boldsymbol{\theta}_-)$$
$$R(\boldsymbol{\theta}_L) = R(\boldsymbol{\theta}_-) \cdot R(\boldsymbol{\theta}_+).$$

Then $\vec{R}_k^R = R(\boldsymbol{\theta}_R)\vec{R}_{k-1}^R$ and $\vec{R}_k^L = R(\boldsymbol{\theta}_L)\vec{R}_{k-1}^L$. As discussed before, $\vec{R}_k^L$'s are distributed on a circle around the axis of $\boldsymbol{\theta}_L$ passing through the south pole and $\vec{R}_k^R$'s are distributed on a circle around the axis of $\boldsymbol{\theta}_R$ passing through the north pole. $(\overline{\vec{R}_k^R})_3 = -(\overline{\vec{R}_k^L})_3$ can be obtained from symmetry. The size of the circles not only depends on $\theta = |\boldsymbol{\theta}_+| = |\boldsymbol{\theta}_-|$, but also on the relative azimuthal angle between $\boldsymbol{\theta}_\pm$, denoted by 2α in Figure B.1. In fact, the inclination angle of $\boldsymbol{\theta}_R$ (β in Figure B.1) satisfies

$$\tan\beta = \tan\frac{\theta}{2}\sin\alpha. \tag{B.4}$$

Recalling the definition of the nonadiabatic transition probability in Eq. (2.7), we have

$$P_{nad} = \frac{1+\cos\theta}{2} = \cos^2\frac{\theta}{2}$$

for a single pulse. An interesting observation of Eq. (B.4) is that no matter how small P_{nad} is, so long as it is not zero, the circle formed by the Bloch vectors after each period can be as large as a meridian circle! The reason is that $P_{nad} \neq 0$ implies a nonzero $\cos\theta/2$ and thus a finite $\tan\theta/2$, and then from Eq. (B.4) $\beta = 0$ for $\alpha = 0$, which corresponds to a meridian circle. This echoes what we claimed near the end of Section 2.3. Although for the extreme

case of a meridian circle, $(\overline{\vec{R}_k^R})_3 = (\overline{\vec{R}_k^L})_3 = 0$, the net force is zero, we will show that the force averaged over α (and so kx) is large as long as P_{nad} is small. Indeed, from Eq. (B.3) we have

$$F(\alpha) = \frac{\hbar k}{T} 2(\overline{\vec{R}_k^R})_3 = \frac{2\hbar k}{T} \sin^2 \beta, \tag{B.5}$$

by averaging over α,

$$\overline{F} = \frac{2}{\pi} \int_0^{\frac{\pi}{2}} F(\alpha) d\alpha = \frac{2}{\pi} \frac{2\hbar k}{T} \int_0^{\frac{\pi}{2}} d\alpha \sin^2 \beta.$$

Using Eq. (B.4),

$$\overline{F} = \frac{2\hbar k}{T}(1 - \cos\frac{\theta}{2}) = \frac{2\hbar k}{T}(1 - \sqrt{P_{nad}}).$$

It has some similarity as the force formula of single pulse in Eq. (2.11).

B.2 Force on Moving Atoms

For an atom moving at velocity v to the right, the torque vectors of the left- and right- propagating light are blue- and red- shifted by kv respectively, as illustrated in Figure B.3. For arbitrary kv, the periodicity of the pulse train is broken down. However, for $kv = n\omega_m$, the doppler-shifted fields are still periodic. $\boldsymbol{\theta}_\pm$ in these cases are no longer in the equatorial plane, but for symmetric pulses $\boldsymbol{\theta}_\pm$ have the same magnitude and opposite inclination angle. Therefore $\boldsymbol{\theta}_R$ and $\boldsymbol{\theta}_L$ still have opposite inclination angle, and Eq. (B.5) still

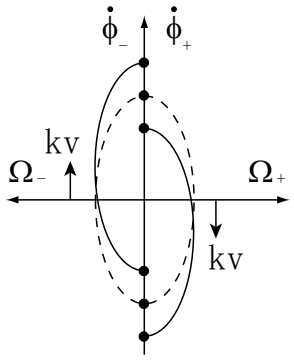

Figure B.3: Doppler shifted torque vectors for moving atoms.

holds. Assuming $\boldsymbol{\theta}_\pm$ have magnitude θ and inclination angle $\pm\varphi$, we have

$$\tan^2\beta = \frac{\sin^2\alpha}{\tan^2\varphi + \cot^2\frac{\theta}{2}\sec^2\varphi}.$$

Averaged over α,

$$\overline{F} = \frac{2\hbar k}{T}\left(1 - \sqrt{\cos^2\frac{\theta}{2} + \sin^2\frac{\theta}{2}\sin^2\varphi}\right).$$

On the other hand, the nonadiabatic transition probability of a pulse is

$$P_{nad} = \frac{1 + \cos\theta\cos^2\varphi + \sin^2\varphi}{2} = \cos^2\frac{\theta}{2} + \sin^2\frac{\theta}{2}\sin^2\varphi.$$

Surprisingly we achieve the same conclusion $\overline{F} = (2\hbar k/T)(1 - \sqrt{P_{nad}})$.

Bibliography

[1] D. Wineland and H. Dehmelt. Proposed $10^{14}\delta\nu/\nu$ laser fluorescence spectroscopy on tl^+ mono-ion oscillator. *Bull. Am. Phys. Soc.*, 20:637, 1975.

[2] T. Hänsch and A. Schawlow. Cooling of gases by laser radiation. *Opt. Commun.*, 13(1):68–71, 1975.

[3] D. Wineland and W. Itano. Laser cooling of atoms. *Phys. Rev. A*, 20(4):1521–1540, 1979.

[4] H. Metcalf and P. van der Straten. *Laser Cooling and Trapping*. Springer, New York, 1999.

[5] C.S. Adams and E. Riis. Laser cooling and trapping of neutral atoms. *Prog. Quantum Electron.*, 21:1, 1997.

[6] D. Suter. *The Physics of Laser-Atom Interactions*. Cambridge University Press, Cambridge, 1997.

[7] L. Allen and J.H. Eberly. *Optical Resonance and Two-Level Atoms*. Dover, New York, 1987.

[8] C. Cohen-Tannoudji, J. Dupont-Roc, and G. Grynberg. *Atom-Photon Interactions*. J. Wiley & Sons, New York, 1992.

[9] R. Feynman, F. Vernon, and R. Hellwarth. Geometrical representation of the schrödinger equation for solving maser problems. *J. Appl. Phys.*, 28(1):49–52, 1957.

[10] P.W. Milonni and J.H. Eberly. *Lasers*. Wiley, New York, 1988.

[11] W. Phillips and H. Metcalf. Laser deceleration of an atomic beam. *Phys. Rev. Lett.*, 48(9):596–599, 1982.

[12] P. Lett, R. Watts, C. Westbrook, W. Phillips, P. Gould, and H. Metcalf. Observation of atoms laser cooled below the doppler limit. *Phys. Rev. Lett.*, 61(2):169–172, 1988.

[13] P.J. Ungar, D.S. Weiss, S. Chu, and E. Riis. Optical molasses and multilevel atoms — theory. *J. Opt. Soc. Am. B*, 6(11):2058–2071, 1989.

[14] J. Dalibard and C. Cohen-Tannoudji. Laser cooling below the Doppler limit by polarization gradients - simple theoretcal models. *J.Opt.Soc.Am. B*, 6:2023–2045, 1989.

[15] S.Q. Shang, B. Sheehy, P. van der Straten, and H. Metcalf. Velocity-selective magnetic-resonance laser cooling. *Phys. Rev. Lett.*, 65(3):317–320, 1990.

[16] J. Dalibard and C. Cohen-Tannoudji. Dressed atom approach to atomic motion in laser light: The dipole force revisited. *J. Opt. Soc. Am. B*, 2(11):1707, 1985.

[17] C. Cohen-Tannoudji and W.D. Phillips. New mechanisms for laser cooling. *Phys. Today*, 43(10):October, 33–40, 1990.

[18] A.P. Kazantsev and I.V. Krasnov. Interference phenomena and the radiative force rectification effect. *Zh. Eksp. Teor. Fiz.*, 95(1):104–113, 1989.

[19] V.S. Voitsekhovich, M.V. Danileiko, A.M. Negriiko, V.I. Romanenko, and L.P. Yatsenko. Observation of a stimulated radiation pressure of amplitude-modulated light on atoms. *Pisma Zhur. Teor. Eksp. Fiz.*, 49(3):138–140, 1989. [JETP Lett. **49**, 161-164, (1989)].

[20] R. Grimm, Yu.B. Ovchinnikov, A.I. Sidorov, and V.S. Letokhov. Observation of a strong rectified dipole force in a bichromatic standing light-wave. *Phys. Rev. Lett.*, 65(12):1415–1418, 1990.

[21] V.S. Voitsekhovich, M.V. Danileiko, A.M. Negriiko, and et al. 'general disc. of bichro'. *Zh. Eksp. Teor. Fiz.*, 99(2):393–410, 1991. [Sov. Phys. JETP **72**, 219-227, (1992)].

[22] R. Gupta, C. Xie, S. Padua, H. Batelaan, and H. Metcalf. Bichromatic laser cooling in a 3-level system. *Phys. Rev. Lett.*, 71(19):3087–3090, 1993.

[23] J. Söding, R. Grimm, Yu.B. Ovchinnikov, P. Bouyer, and C. Salomon. Short-distance atomic-beam deceleration with a stimulated light force. *Phys. Rev. Lett.*, 78(8):1420–1423, 1997.

[24] M. Williams, F. Chi, M. Cashen, and H. Metcalf. Measurement of the bichromatic optical force on rb atoms. *Phys. Rev. A*, 60:R1763–R1766, 1999.

[25] M. Williams, F. Chi, M. Cashen, and H. Metcalf. Bichromatic force measurements using atomic beam deflections. *Phys. Rev. A*, 61:023408, 2000.

[26] M. Cashen and H. Metcalf. Bichromatic force on helium. *Phys. Rev. A*, 63:025406, 2001.

[27] M. Cashen and H. Metcalf. Optical forces on atoms in nonmonochromatic light. *J. Opt. Soc. Am. B*, 20:915, 2003.

[28] M. Partlow, X. Miao, J. Bochmann, M. Cashen, and H. Metcalf. Bichromatic slowing and collimation to make an intense helium beam. *Phys. Rev. Lett.*, 93:213004, 2004.

[29] V.S. Voitsekhovich, M.V. Danileiko, A.M. Negriiko, V.I. Romanenko, and L.P. Yatsenko. Light pressure on atoms in counterpropagating amplitude-modulated waves. *Zh. Tekh. Fiz.*, 58(6):1174–1176, 1988. [Sov. Phys. Tech. Phys. **33**, 690-691, (1988)].

[30] R. Grimm, J. Söding, and Yu.B. Ovchinnikov. Coherent beam splitter for atoms based on a bichromatic standing light-wave. *Opt. Lett.*, 19(9):658–660, 1994.

[31] R. Grimm, G. Wasik, J. Söding, and Yu.B. Ovchinnikov. Laser cooling and trapping with rectified optical dipole forces. In A. Aspect, W. Barletta, and R. Bonifacio, editors, *Proceedings of the Fermi School CXXXI*, page 481, Amsterdam, 1996. IOS Press.

[32] L. Yatsenko and H. Metcalf. A dressed atom description of the bichromatic force. *Phys. Rev. A*, 70:063402, 2004.

[33] A. Abragam. *Principles of Nuclear Magnetism.* Oxford University Press, Oxford, 2002.

[34] E. B. Treasy. Adiabatic inversion with light pulses. *Phys. Lett. A*, 27:421, 1968.

[35] M. M. T. Loy. Observation of population inversion by optical adiabatic rapid passage. *Phys. Rev. Lett.*, 32:814, 1974.

[36] I. Nebenzahl and A. Szoke. Deflection of atomic beams by resonance radiation using stimulated emission. *Appl. Phys. Lett.*, 25:327–329, 1974.

[37] T. Lu, X. Miao, and H. Metcalf. Bloch theorem on the bloch sphere. *Phys. Rev. A*, 71:061405, 2005.

[38] L. P. Yatsenko, S. Guérin, and H. R. Jauslin. Topology of adiabatic passage. *Phys. Rev. A*, 65:043407, 2002.

[39] E. Riis G.-L. Oppo, S. M. Barnett and M. Wilkinson. *Quantum Dynamics of Simple Systems*. Institute of Physics, 1996.

[40] A. Shapere and F. Wilczek. *Geometric Phases in Physics*. World Scientific, 1989.

[41] E.E. Nikitin. *Theory of Elementary Atomic and Molecular Processes in Gases*. Clarendon Press - Oxford, 1974.

[42] D. Sawicki and J. H. Eberly. Perfect following in the adiabatic limit. *Optics Express*, 4:217, 1999.

[43] J. P. Davis and P. Pechukas. Nonadiabatic transition induced by a time-dependent hamiltonian in the semiclassical/adiabatic limit: The two-state case. *J. Chem. Phys.*, 64:3129, 1976.

[44] B. M. Garraway K.-A. Suominen and S. Stenholm. The adiabatic limit of level crossing models. *Optics Communications*, 82:260, 1991.

[45] L. Landau. *Phys. Z. Sowjet.*, 2:46, 1932.

[46] J. R. Rubbmark, M. M. Kash, M. G. Littman, and D. Kleppner. Dynamical effects at avoided level crossings: A study of the landau-zener effect using rydberg atoms. *Phys. Rev. A*, 23:3107, 1981.

[47] Yu. N. Demkov and M. Kunike. *Vestn. Leningr. Univ. Fis. Khim.*, 16:39, 1969.

[48] K.-A. Suominen and B. M. Garraway. Population transfer in a level-crossing model with two time scales. *Phys. Rev. A*, 45:374, 1992.

[49] H.J. Metcalf and P. van der Straten. *Laser Cooling and Trapping*. Springer-Verlag, New York, 1999.

[50] S. Nowak, T. Pfau, and J. Mlynek. Nanolithography with metastable helium. *Appl. Phys. B*, 63:203, 1996.

[51] K. K. Berggren, A. Bard, J. L. Wilbur, J. D.Gillaspy, A. G. Helg, J. J. McClelland, S. L. Rolston, W. D. Phillips, M. Prentiss, and G. M. Whitesides. Microlithography by using neutral metastable atoms and self-assembled monolayers. *Science*, 269:1255, 1995.

[52] M. Cashen. *Optical Forces on Atoms in Polychromatic Light Fields*. PhD thesis, Stony Brook University, 2002.

[53] M. Partlow. *Bichromatic Collimation to Make an Intense Helium Beam*. PhD thesis, Stony Brook University, 2004.

[54] J. Kawanaka, M. Hagiuda, K. Shimizu, F. Shimizu, and H. Takuma. Generation of an intense low-velocity metastable-neon atomic-beam. *App. Phys. B*, 56(1):21–24, 1993.

[55] H. Mastwijk. *Cold Collisions of Metastable Helium Atoms*. PhD thesis, Utrecht University, 1997.

[56] H. Mastwijk, J. Thomsen, P. van der Straten, and A. Niehaus. Optical collisions of cold, metastable helium atoms. *Phys. Rev. Lett.*, 80(25):5516–5519, 1998.

[57] W. Lu, M.D. Hoogerland, D. Milic, K.G.H. Baldwin, and S.J. Buckman. A bright metastable atom source at 80 k. *Rev. Sci. Instrum.*, 72:2558–61, 2001.

[58] D. Meschede and H. Metcalf. Atomic nanofabrication: atomic deposition and lithography by laser and magnetic forces. *J. Phys. D: Appl. Phys.*, 36:R17, 2003.

[59] A. Dalgarno K. L. Bell and A. E. Kingston. Penning ionization by metastable helium atoms. *J. Phys. B*, 1:18, 1968.

[60] C.L. Bohler and B.I. Marton. Helium spectroscopy using an ingaas laser diode. *Opt. Lett.*, 19:1346–48, 1994.

[61] C. Avila. Spectral control of a 1083 nm diode laser. Master's thesis, Stony Brook University, 1998.

[62] C.E. Wieman and L. Hollberg. Using diode lasers for atomic physics. *Rev. Sci. Instrum.*, 62:1–20, 1991.

[63] M. Prevedelli, P. Cancio, G. Giusfredi, F.S. Pavone, and M. Inguscio. Frequency control of dbr diode lasers at 1.08 micrometer and precision spectroscopy of helium. *Opt. Comm.*, 125:231–236, 1996.

[64] W. Demtröder. *Laser Spectroscopy - Basic Concepts and Instrumentation - 3rd Edition.* Springer-Verlag, Berlin, 2003.

[65] A. Yariv. *Optical Electronics in Modern Communications.* Oxford University Press, New York, 1997.

[66] G.L. Li and P.K.L. Yu. Optical intensity modulators for digital and analog application. *J. Lightwave Tech.*, 21:2010, 2003.

[67] R.A. Boyd, J. L. Bliss, and K.G. Libbrecht. Teaching physics with 670-nm diode-lasers — experiments with fabry-perot cavities. *Amer. J. Phys.*, 64(9):1109–1116, 1996.

[68] G.P. Agrawal. *Fiber-Optic Communication Systems, 3rd Edition.* Wiley-Interscience, New York, 2002.

[69] S. Bordais, S. Grot, Y. Jaouën, P. Besnard, and M.L. Flohic. Double-clad 10-w yb^{3+} doped fiber master oscillator power fiber amplifier for he^{3+} optical pumping. *Applied Optics*, 43:2168, 2004.

[70] D.T. Walton, J. Nees, and G. Mourou. Broad-bandwidth pulse amplification to the $10 - \mu j$ level in an ytterbium-doped germanosilicate fiber. *Opt. Lett.*, 21:1061, 1996.

[71] R. Ulrich, S.C. Rashleigh, and W. Eickhoff. Bending-induced birefringence in single-mode fibers. *Opt. Lett.*, 5:273, 1980.

[72] G.B. Arfken and H. J. weber. *Mathematical Methods for Physicists.* Academic Press, Inc, London, 1995.

[73] A.R.P. Rau. Unitary integration of quantum liouville-bloch equations. *Phys. Rev. Lett.*, 81:4785, 1998.

[74] J. J. Sakurai. *Modern Quantum Mechanics.* Addison-Wesley, 1994.

[75] M. V. Berry. Histories of adiabatic quantum transition. *Proc. R. Soc. A*, 429:61, 1990.